CELLULAR FORCES AND MECHANICAL COUPLING USING MICROENGINEERED DEVICES

by

Craig R. Copeland

A dissertation submitted to The Johns Hopkins University in conformity with the requirements for the degree of Doctor of Philosophy.

Baltimore, Maryland

February, 2014

Abstract

The biological response of cells to mechanical forces is integral to both normal cell function and the progression of many diseases. Physical cues experienced by cells arise from internally generated contractile forces, as well as from external sources of force and strain in the local environment. We have used arrays of flexible micron-scale poly(dimethylsiloxane) (PDMS) cantilevers (posts) to probe the behavior of cell-generated contractile forces under varying chemical and mechanical conditions. The cells' contractile forces displace the tops of the underlying posts, which are individually tracked through microscopy and image analysis, yielding a dynamic, micron-scale map of the cells' mechanical activity. I have applied these techniques to study cell generated forces in two experimental systems. First, force generation by cardiac fibroblasts (CFs) in order to elucidate mechanical coupling between these cells and the myocytes responsible for the heart's pumping action, which may contribute to certain types of cardiac arrhythmias. These experiments were part of a collaborative effort which demonstrated that modulation of both CF contractile forces, and the cellular structures on which these forces can act when coupled to cardiac myocytes, had direct influence on the electrical conduction mechanisms that are critical for the proper functioning of cardiac muscle tissue.

The second experimental system studied the impact of force application through an applied global stretch on the traction force dynamics of arterial smooth muscle cells. These cells, resident within the inner walls of arteries, are constantly exposed to global stretching forces as a result of changes in blood pressure and flow. I developed an enhanced version of the micropost array that enabled the application of controlled global stretch to cells while the evolution of traction forces could be measured in real time. These measurements revealed a heterogeneous response to imposed strain, as a portion of the tested cells responded by increasing their force generation against the micropost substrate, while others underwent plastic deformation and exhibited relatively small changes in force generation. Upon reversal of stretch direction, all cells exhibited decreasing force generation that is characteristic of a viscoelastic response. Following stretch completion and left at rest, all cells demonstrated active recovery and re-establishment of contractile forces.

I have also demonstrated the combined use of a laminar flow technique, micropipette "spritzing", with both micropost arrays and microfabricated tissue gauges for application of local chemical stimulation to single cells or single tissues while observing contractile dynamics in real time.

Adviser: Daniel H. Reich

Acknowledgements

I would like to thank Dr. Daniel Reich for all of his guidance and understanding throughout the time we have worked together. My fellow lab members Alan Liu, Prasenjit Bose, and Yu Shi, have been a pleasure to get to know and to work with. My former colleagues Ruogang Zhao, Susan Thompson, Jim Felton, Corinne Kramer, and Stuart Kirschner, have all provided me with instrumental teachings and valuable advice and insights along the way. I would like to thank Dr. Christopher Chen, at Boston University, and Dr. Leslie Tung with the Department of Biomedical Engineering, for their interdisciplinary guidance and effort in providing me with opportunities for unique and exciting research. The Johns Hopkins University Institute for Nanobiotechnology provided me with excellent resources and opportunities to expand my professional and educational boundaries.

I would like to thank all of my family and friends for their support and encouragement over the years. Finally, I would like to thank my wife Shannon for her endless patience and understanding.

Contents

List of Figures

Chapter 1 Introduction

Biological systems, from ecological networks down to single cells, represent a critical frontier in our understanding of the universe. At the scale of a single cell, these systems, while vast in complexity, must operate on the basis of physical laws governing the interactions of single molecules. Studying these systems at mesoscopic (cellular/sub-cellular) scales provides insight into the emergence of biological function from these fundamental interactions. As tools to further our understanding, microengineered devices are advancing our ability to not only probe and measure the properties of living cells and tissues, but to selectively alter and control the microenvironment for targeted studies of specific behaviors, interactions, and adaptations.

1.1 Cellular Structure and Force Generation

1.1.1 Cellular Structure

The primary physical structure that establishes the mechanical properties of a biological cell is the cytoskeleton. The cytoskeleton is a filamentous network that supports the cell and defines the structure and shape. There are three main types of filaments that comprise the cytoskeleton. The largest, microtubules, are hollow cylinders ~23 nm in diameter. Microtubules play important roles in the intracellular transport of organelles, and are perhaps best known for their role in the formation of the mitotic spindle and chromosome separation during cell division. Intermediate filaments, ~10 nm in diameter, serve to anchor organelles, supply structural support for the nuclear lamina, a fibrous network inside the cell nucleus, and support cell shape. The third type of cytoskeletal filaments are microfilaments. Often referred to as actin filaments (f-actin), due to their being comprised of polymerized actin subunits known as globular actin, or g-actin, these filaments are ~6 nm in diameter and are highly dynamic. Actin filaments span the entire cell, providing structure and mechanical support (Fig 1.1). Actin filament dynamics are regulated by processes that serve to polymerize, or grow, what is known as the “barbed” end of fibers, and depolymerize subunits at the “pointed” end. The relative rates of these two processes play a primary role in driving morphological changes and cell motility, and are regulated by cell signaling mechanisms. The action of proteins such as the actin severing protein cofilin, which cleaves actin subunits from the pointed end, or profilin, which promotes polymerization at the barbed end, are regulated to facilitate physical cellular dynamics [1].

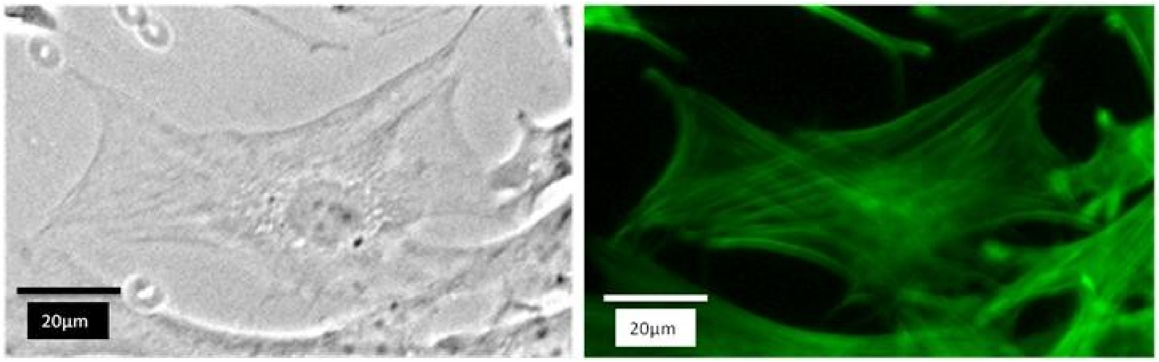

Figure 1.1: (A) Phase contrast image of a NIH 3T3 fibroblast cultured on a two dimensional substrate. (B) Fluorescence image of the same cell showing actin fibers labeled using Alexa-Fluor 488 Phalloidin.

1.1.2 Force Generation

Actin filaments are the primary medium through which cells are able to generate force. Actin polymerization at a cell's leading edge generates outwardly directed force that facilitates the formation of cellular protrusions known as pseudopodia, and coupled with actin depolymerzation at the trailing edge, enables a cell to undergo amoeboid movement, or “crawling” within its environment. More predominantly, the actin network enables a cell to generate inwardly directed contractile forces. This is achieved through the action of mysosin motors, which are specialized proteins that bind to and cross-link actin filaments. Adenosine tri-phosphate (ATP) hydrolysis produces the necessary energy for conformational changes in actin bound myosin that enable the myosin to move or “walk” along the filaments. Through this mechanism myosin motors generate a relative sliding motion between cross linked actin filaments (Fig 1.2). This system for generating force is commonly referred to as the “acto-myosin” system[1]. Regulation of the acto-myosin system in non-striated muscle tissue is predominantly controlled by the Rho family GTPase, RhoA. GTPases are protein complexes that function as molecular switches for controlling signaling processes. They are turned on and off through hydrolysis of guanosine triphosphate (GTP), a source of energy within cells that is similar to ATP. Through this switching mechanism, RhoA phosphorylates, or activates, the protein ROCK. ROCK then inhibits myosin light chain (MLC) phosphatase, which when uninhibited serves to decrease myosin activity, leading to increased myosin activity and increased contraction. [2].

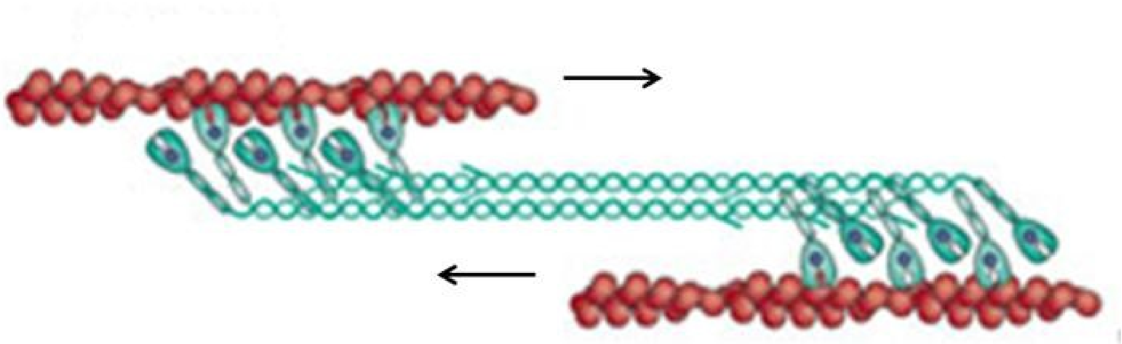

Figure 1.2: Schematic of myosin motor proteins (blue), crosslinking two acti fibers (red) for generation of relative sliding motion (arrows) [2].

The binding of myosin to actin, a necessity for generation of contractile force, is largely dependent on the concentration of intracellular calcium, particularly in skeletal and cardiac muscle cells. In the absence of calcium, myosin binding sites located on actin fibers are blocked and the myosin head is unable to bind to and cross link actin fibers. The protein complexes that block these binding sites, tropomyosin in particular, undergo conformational changes as a result of binding calcium. These changes expose the myosin binding site on the actin fibers allowing myosin to bind and cross link the fibers, ultimately facilitating the generation of contractile force [1]. In this way, regulation of intracellular calcium can regulate the contractile state of a cell. In cardiac muscle, for instance, the regulation of calcium through transmitted electrical signals is what triggers the contraction of cardiac muscle [3].

1.2 Cell Adhesion

A cell's acto-myosin system is bound, or anchored, to adhesion sites located near the cell's periphery. These adhesion sites are connected to proteins that span the width of the cell membrane, known as trans-membrane proteins, which are capable of binding to structures exterior to the cell. Different types of adhesive junctions exist to provide cellular attachment to either the extra cellular matrix, or to other cells. In addition, there are different types of cell-cell junctions that enable specialized interactions between cells.

1.2.1 Cell-Substrate Adhesion

The extracellular matrix, or ECM, is a complex structure that occupies the intercellular space, consisting in part of structural proteins (collagens, elastins) that provide mechanical support, and adhesive proteins (fibronectin, laminins) for cellular attachment (Fig 1.3)[1].

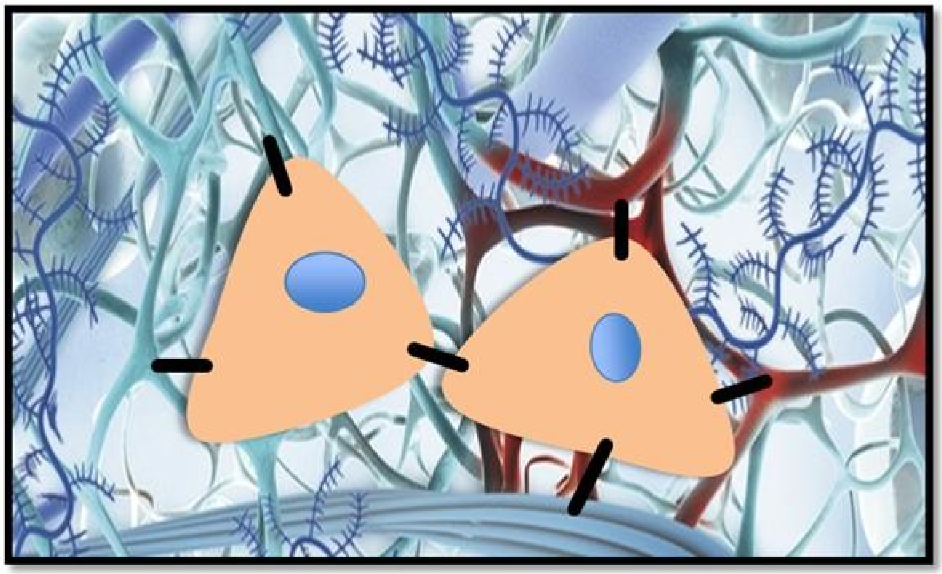

Figure 1.3: Schematic of two cells adhered to each other and the surrounding extra cellular matrix (ECM) within a tissue[4].

Trans-membrane proteins that serve to link the cytoskeleton with the surrounding ECM are known as integrins. The portion of integrins that is external to the cell varies in structure based on the type of ECM protein it is designed to bind with, and while the internal portion has specific binding sites for attachment to the cytoskeleton, this portion can also vary in structure based on the cell type in which it is located [1, 5]. Linkages between integrins and the cytoskeleton occur at adhesive junctions known as focal adhesions, or more dynamic focal complexes. Focal adhesions consist of a variety of adapter proteins (vinculin, α-actinin, talin) that are responsible for direct binding of integrins to the actin cytoskeleton, as well as signaling proteins (e.g. focal adhesion kinase) for dynamic regulation[6]. Figure 1.4 shows fluorescently labeled vinculin present within a pair of smooth muscle cells cultured on a two dimensional substrate, indicating the presence of focal adhesions.

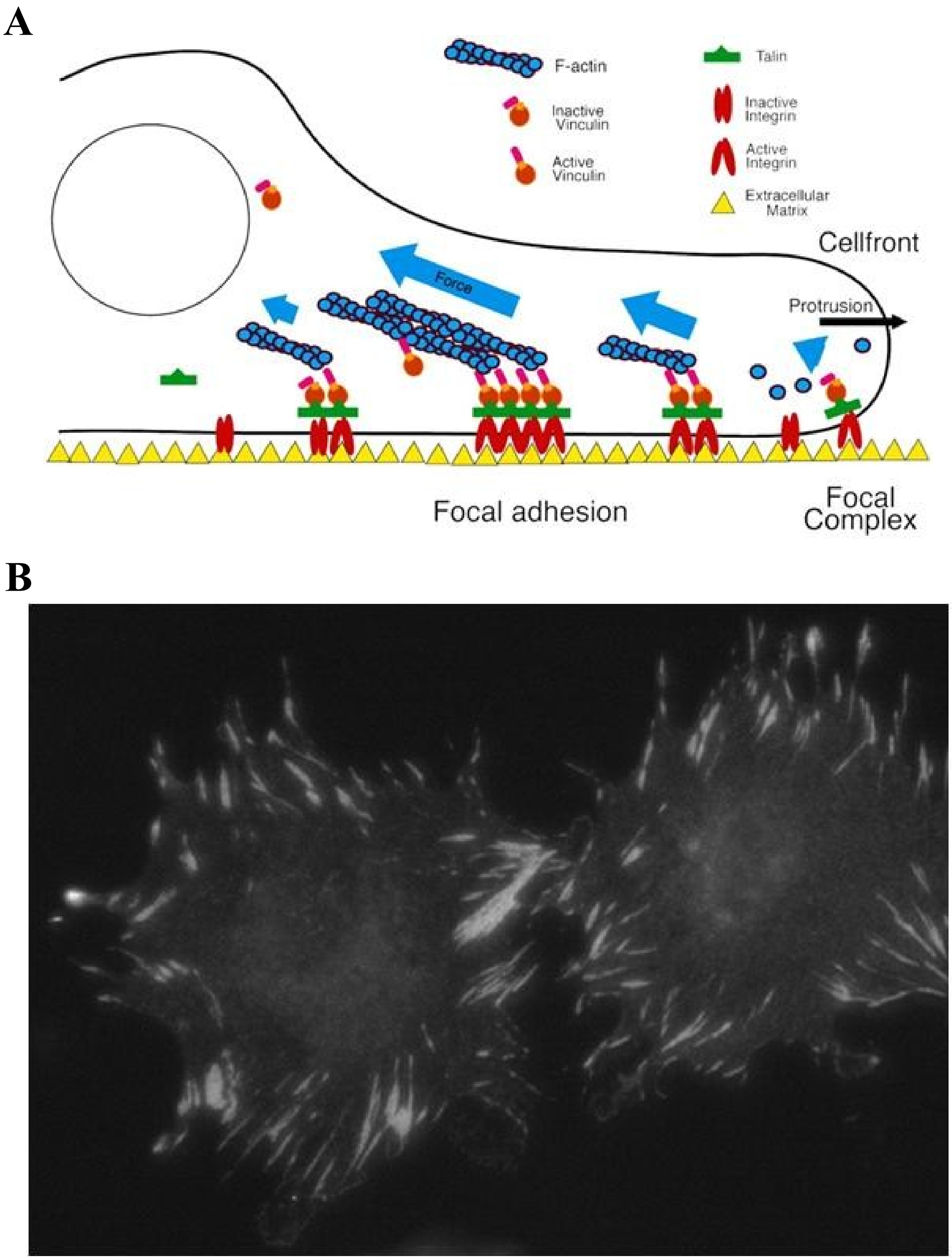

Figure 1.4: (A) Schematic of a cell with cytoskeleton adhered to ECM via focal adhesions [7]. (B) Fluorescence image of smooth muscle cells cultured on a two dimensional substrate. Fluorescently labeled vinculin (light patches) indicates the presence of focal adhesions connecting the cells with ECM located on the substrate surface.

1.2.2 Cell-Cell Adhesions

Similar to integrins and focal adhesions, adhesive junctions between neighboring cells rely on trans-membrane proteins called cadherins. The inner portion of cadherins link to the actin cytoskeleton using similar adapter proteins found in focal adhesions, whereas the outer portion binds to other cadherins presented on the membrane surface of other cells (Fig 1.5).

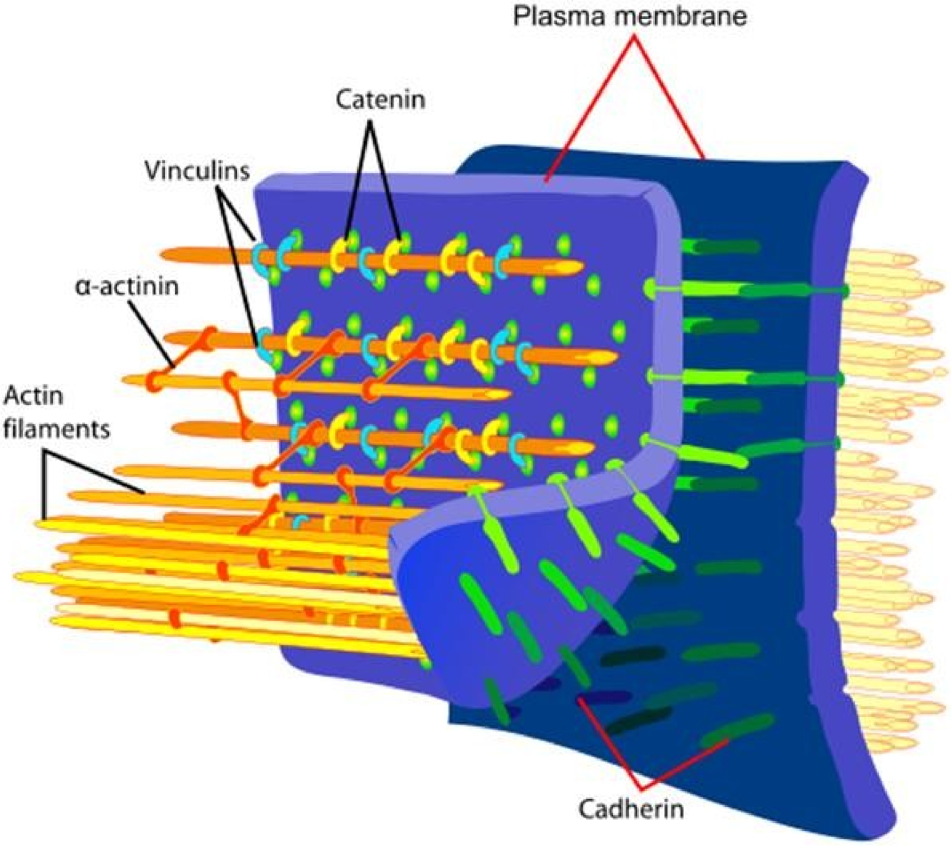

Figure 1.5: Schematic diagram of an adherens junction showing cadherin-mediated attachment between cytoskeletal actin filaments of two adjacent cells. (Image by Mariana Ruiz, Wikimedia commons).

Other types of cell-cell junctions include “tight junctions”, which form between adjacent cells and bring the membranes in close enough proximity to prevent fluid flow in the intercellular space [1]. The third type of cell-cell junctions are gap junctions, formed by trans-membrane proteins called connexins. Connexin monomers cluster together to form hollow cylinders that allow for the passage of small ions and molecules between the cytoplasms of the two cells (Figure 1.6) [1].

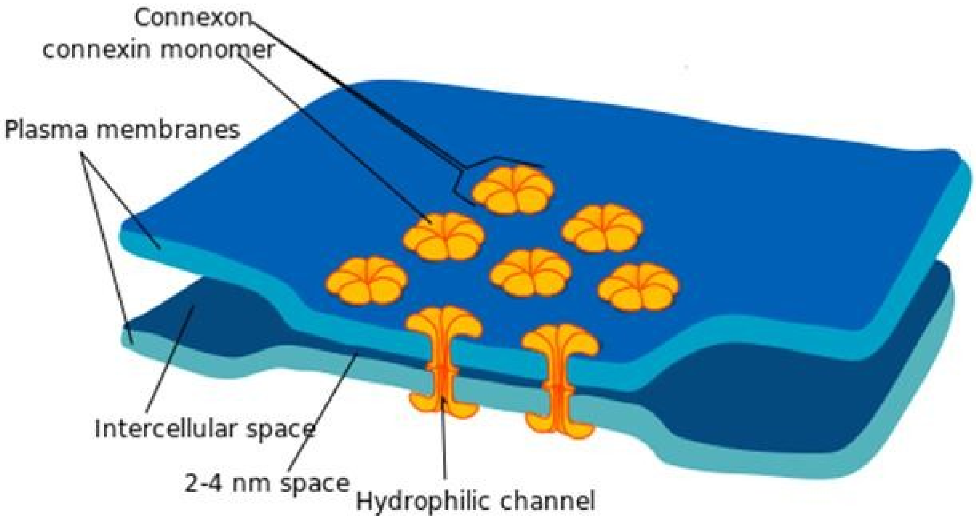

Figure 1.6: Schematic diagram of gap junctions between two plasma membranes. Connexin monomers form hollow, cylindrical channels allowing for the passage of small ions and molecules from cell to cell. (Picture by Mariana Ruiz, Wikimedia commons).

1.2.3 Mechanotransduction, Cell Behavior, and Pathology

Sites of cellular adhesion provide, through linkage to the acto-myosin system, the means for cells to apply force to their external environment. These same adhesion sites also serve as a means of transmitting forces imposed on the cell from its environment to the cytoskeleton. The process through which a cell transduces, or converts, a mechanical stimulus into a biochemical signal or, more generally, cellular action, is termed Mechanotransdution. The interplay between both force generation and force sensing with focal adhesion dynamics has been observed in studies that demonstrated that the application of mechanical stress was required for maturation of focal complexes into focal adhesions [8], and that regulation of RhoA facilitated focal adhesion assembly, as well as actin stress fiber formation . More recently, acto-myosin generated forces acting at adherens junctions have been measured in patterned endothelial cell pairs, and found to regulate adherens junction size [9].

Not only do mechanical forces influence the regulation of cellular adhesions, mechanical stimuli have been shown to affect a broad range of cellular processes and behaviors. Endothelial cells can be influenced to either proliferate, or undergo programmed cell death (apoptosis) depending on available spreading area [10]. Both the rate [11] and direction [12] of cell migration can be influenced by geometric properties of the ECM. As well, mechanical stresses are known to contribute to the progression of many diseases [13]. For example, the response of endothelial cells to fluid flow shear stress contributes to atherosclerosis progression [14] , and specific lines of melanoma cells are resistant to mechanical trauma and therefore more likely to survive and invade capillaries [15].

1.3 Model Systems and Experimental Overview

Despite advances in our understanding of the molecular basis for force generation and mechanotransduction in cells, the ways in which these molecular level phenomena are translated into whole-cell forces and dynamics are still not well understood. In order to identify potential targets for treatment of mechanically mediated diseases, it is critical that our understanding of the mechanotransduction process continues to advance. Targeted studies that focus on carefully chosen model systems are particularly useful in that they allow for investigation of biological function and response that is directly tied to their in vivo functionality.

I have studied cellular force generation in two model systems, the first of which consisted of neonatal rat ventricular fibroblasts (CFs) in order to study mechanical coupling between CFs and cardiac myocytes. The muscular tissue in the heart, known as the myocardium, is responsible for contraction and initiation of blood flow. Electrical signals initiated in the sinoatrial node propagate through the myocardium, facilitating the coordinated beating action of the tissue. The two main cell types [16] resident in the myocardium are cardiomyocytes, the functionally contractile cells responsible for beating; and cardiac fibroblasts (CFs), which are responsible for production and remodeling of the extra cellularmatrix (ECM), particularly during wound healing [17], and have more recently been implicated in processes such as cell signaling, heterocellular coupling, and mechanoelectric feedback [16]. Cardiac myocytes are coupled to one another via electrical gap junctions that allow for the passage of electrical signals from cell to cell. As ions flow across gap junctions, the cell membrane becomes electrically depolarized from its resting, negative voltage state. This depolarization triggers the cell to rapidly generate strong transient contractile forces, causing an effective “beat” as the entire cell body contracts and then returns to rest.

Following cardiac injury, such as infarction, cardiac fibroblasts migrate to the region of injury in order to replace necrotic tissue with new ECM (scar tissue), and to generate sustained contractile forces in order to minimize the scar area. To facilitate this functionality, cardiac fibroblasts differentiate into cardiac myofibroblasts (CMFs), a more contractile phenotype capable of generating high magnitude tonic contraction forces [18-20] . Due to their coexistence in cardiac muscle, understanding heterocellular coupling of cardiac myocytes and CFs is critical to our knowledge of heart physiology. Experiments in chapter 3 of this work directly measured the contractile force generation of cardiac fibroblasts (CFs) under a variety experimental conditions chosen to elucidate the role of mechanical coupling between cardiac fibroblasts and cardiac mycoytes on the physiology of cardiac tissue. CF contractile forces were measured using arrays force sensing microposts, originally developed by Tan et al., which enable direct measurement of contractile forces generated by a cell’s acto-mysoin system [21].

The second model system studied application of stretch to bovine pulmonary artery smooth muscle cells (BPASMCs). The middle layer of blood vessels, known as the tunica media, is comprised of smooth muscle cells and extra cellular matrix (Fig. 1.7).

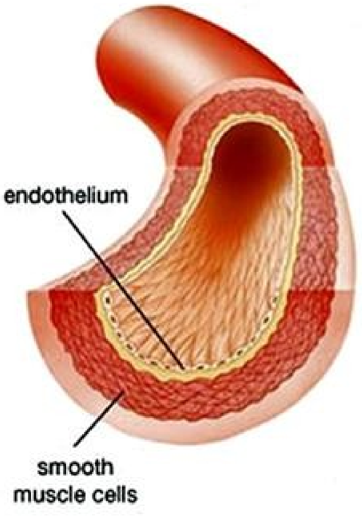

Figure 1.7: Schematic cross section of an artery, showing the location of smooth muscle cells in the arterial wall [22].

The tunica media is integral in the regulation of blood pressure and flow due to its role in controlling blood vessel diameter [23]. Because of this, the arterial SMCs and surrounding matrix are exposed to external global stretching forces caused by changes in blood pressure. In order to establish a more complete understanding of blood vessel physiology, it is therefore necessary to understand how the cells and tissue that form blood vessels respond and adapt in such a mechanically dynamic environment. To this end, I have developed an experimental procedure, described in chapter 4, using a custom cell culture device capable of applying stretch to a flexible membrane, upon which is micropost arrays were fabricated. These experiments enabled the measurement of cell generated traction force dynamics during application of global stretch to BPASMCs.

Chapter 5 demonstrates the combination of a local chemical stimulation technique using glass micropipettes with the aforementioned micropost device, as well as a device for measuring force generation in microtissue constructs[need first TUG paper ref].

1.4 Dissertation Outline

In Chapter 2, methods and experimental techniques for the fabrication, preparation, and analysis of force sensing devices are described. Included is a description of modifying these devices for use on a flexible substrate and of the custom designed culture chamber used for application of stretch. In Chapter 3, the results from studies of cardiac fibroblast force generation are presented, along with data showing the impacts of this force generation on the proper functioning of model cardiac tissues. Chapter 4 describes methods and results of application of global stretch stimulus to BPASMCs using modified force sensing devices. In Chapter 5, the use of an experimental technique combining microfabricated devices and micropipette assisted fluid flow for local chemical stimulation is demonstrated. In Chapter 6 a concluding discussion of all results is presented.

Chapter 2 Methods

2.1 Introduction

The specialized devices, techniques, and procedures utilized in the experiments throughout this work are described below. Cells were cultured and manipulated using standard bio-analytical techniques. Micropost arrays were fabricated via replica molding from a silicon master. A custom stretch chamber of my design was manufactured by the JHU machine shop. Flexible membranes were cast using culture plates as molds. Images of micropost arrays were acquired via microscopy and analyzed for quantification of cellular traction forces.

2.2 Cells

The cells used in the experiments shown in Chapters 4 and 5 were bovine pulmonary artery smooth muscle cells (BPASMCs). These cells were provided by the lab of Christopher Chen at the University of Pennsylvania. The cells used for the cardiac experiments in Chapter 3 were neonatal rat ventricular fibroblasts. These cells were isolated in the lab of Leslie Tung in the department of Biomedical Engineering at Johns Hopkins University.

2.2.1 Culture

All cells used were cultured in low glucose Dulbecco's Modified Eagle Medium (DMEM) containing 1% Penicillin-Streptomycin (antibiotic) and 10% Bovine Serum. BPASMCs were kept in culture at 37C and 10% CO_2, cardiac fibroblasts were kept at 37C and 5% CO_2. BPASMCs were passaged at a ratio of 1:4 when they reached 90%-100% confluence, and kept for use in experiments until they reached passage number 18. Cardiac cells were kept and used until pass 3, and were passed at a ratio of 1:10 upon reaching 90%-100% confluence.

2.1.2 Fluorescence Labeling

In order to better locate and visualize cells cultured on micropost arrays, cardiac fibroblasts were fluorescently labeled in a 5µM solution of CellTracker Green CMFDA (Invitrogen, Carlsbad, CA) for 45 minutes, followed by a 1 hour recovery period. BPASMCs were similarly labeled using a 2µM solution for 30 minutes followed by a 1 hour recovery period. In order to determine cell number in BPASMC pair experiments, cell nuclei were fluorescently labeled using Hoechst nuclear stain at a concentration of 1:1000 for 10 minutes (Figure 2.1)

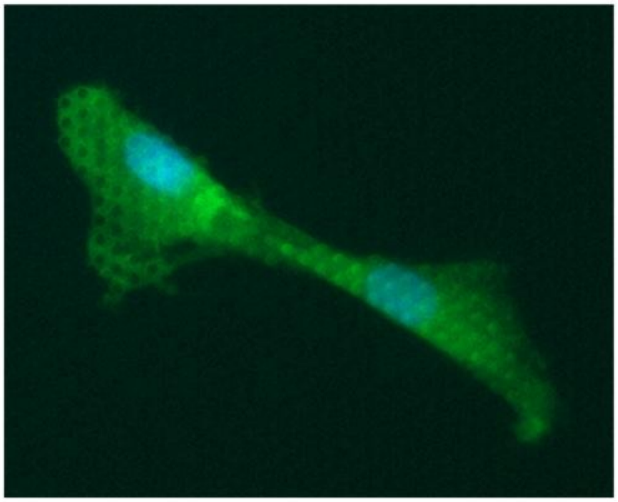

Figure 2.1: Fluorescence image of BPASM cell pair. Cell cytoplasm is visible in green, and the cell nuclei are in blue.

2.1.3 Virus Transfection

Up-regulation of myosin II activity was achieved by transfecting BPASMCs with RhoV14 adenovirus. Adenovirus containing RhoV14 was produced in the lab of Chris Chen. Virus treatment resulted in the production of mutant RhoA that was locked in its activated state. The abundance of activated Rho created up-regulation of myosin II activity [24]. Control cells were transfected with a GFP adenovirus, which caused treated cells to express green fluorescent protein (GFP), and therefore to be visible using fluorescence microscopy (Figure 2.2). BPASMCs were grown in 12-well culture plates, and the media was replaced with 0.5ml of media containing 2µl of Adeno-RhoV14 or 0.5 µl of Adeno-GFP and incubated for 20 hours. After the incubation period the cells were trypsinized and seeded onto mPAD substrates. The virally delivered Rho-V14 genetic sequence also contained sequencing for production of GFP, to be used as visual confirmation of successful transfection. In practice, the efficiency of GFP expression was not sufficient at providing visual confirmation of virus transfection. Therefore, cells were exposed to a large concentration of Adeno-RhoV14 in order to ensure sufficient exposure. Experiments using these cells had to be performed within 18-24 hours after virus incubation in order to observe virus effects before the occurrence of over-expression of RhoA, which would have resulted from the high levels of exposure used and inhibited the cells' ability to spread on the substrate beyond useable limits. Fluorescence expression for Adeno-GFP transfected cells worked as intended, and did not require exposure of control cells to overly large concentrations of virus. However, the same temporal protocol was still used for both Adeno-RhoV14 and Adeno-GFP cells.

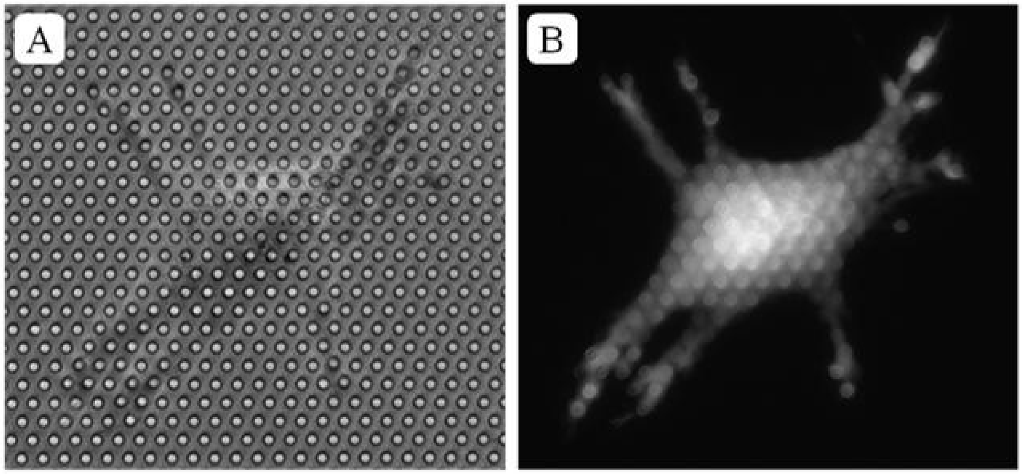

Figure 2.2: Phase contrast (A), and fluorescence (B) images of an adeno-GFP transfected BPASMC on an mPAD.

2.2 Device Fabrication

2.2.1 Micropost Array Detectors

Fabrication and preparation of micropost array detectors (mPADs) for experiments was adapted from published techniques [21, 25]. Micropost arrays masters created in silicon via deep reactive ion etching were obtained from the lab of Christopher Chen at the University of Pennsylvania. Micropost array negative molds were then cast from the silicon masters using Polydimethylsiloxane (PDMS) (Sylgard 184,Dow Corning) mixed at a ratio of 1:10 curing agent to base polymer. Positive geometry PDMS post arrays used for cell culture were then cast from the negative molds. In order to render the negative mold surface non-adhesive to further application of PDMS, the molds were treated with air plasma at 100W for 90s and then coated with a 20 µl of (Tridecauoro-1,1,2,2-Tetrahydrooctyl)-1-Trichlorosilane (United Chemical Technologies) via evaporation in a vacuum dessicator for 18 hours. This allowed for easy removal of the post array substrate from the mold. Post array substrates were built on a glass base using #2 thickness (0.19-0.23mm) cover glass. This thickness allowed for easy sample handling and was sufficiently thin for use with long working distance objectives. (For use with oil/water or otherwise short working distance objectives, #1 thickness (0.13-0.16mm) cover glass should be used.) The cover glass was UV-Ozone treated (Jelight UVO-Cleaner model #42) for 7 minutes at 28 ~ 32 mW/cm^2 @ 253.7 nm to render the surface adhesive to PDMS. A 50 µl drop of 1:10 PDMS was placed onto the negative mold surface and then inverted onto the treated glass surface. Substrates were then cured for 24 hours at 80C in air. In order to prevent collapse of the posts upon removal of the negative mold, the substrates containing the post arrays were submerged in 100% ethanol prior to removal of the negative mold. Once the post array was removed, negative molds could then be left to air dry and stored for use for up to one year.

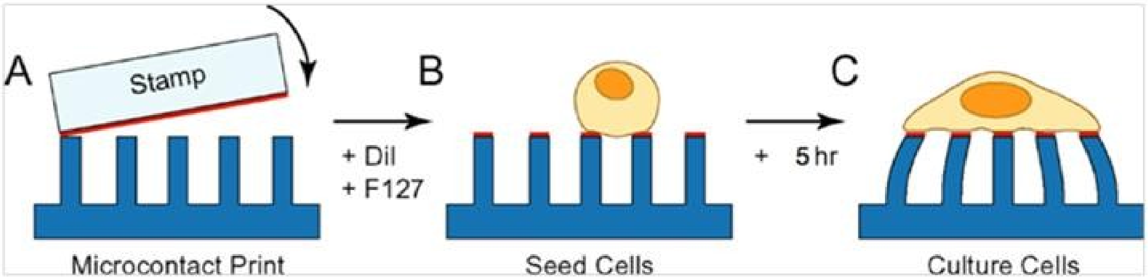

Figure 2.3: Schematic of micropost functionalization and cell seeding. (A) microcontact printing of ECM onto micropost tops, followed by adhesion inhibitor. (B) Cells in suspension seeded onto functionalized arrays. (C) Cells will attach and spread after a minimum of 5 hours. From [25].

PDMS post arrays required functionalization in order to be suitable for cell culture (Figure 2.3) [25]. To create a surface that promoted cellular adhesion, the extracellular matrix (ECM) protein fibronectin was stamped onto the post tops via micro-contact printing (Figure 2.3 A). The stamping technique was used to ensure that only the tops of the posts were coated and not the entire substrate. Before micro-contact printing could be performed, the post arrays had to be dried. If left to dry in air, surface tension from the evaporating ethanol would cause the posts to collapse. Therefore, the arrays were dried in a critical point dryer (Tousimis, Rockville MD) that promotes spontaneous evaporation. Briefly, the ethanol was replaced with liquid CO_2, which was then brought to its critical point and converted into a dense gas. Once the gas was released the posts were dry and ready for stamping.

For the stamping process, stamps made from 1:30 PDMS were coated with 100µl of 50ng/ml fibronectin solution in deionized (DI) water, and left for one hour. During this time, a layer of fibronectin adsorbed onto the stamp surface, which was then gently dried with compressed nitrogen. Post arrays were treated with UV-Ozone for 7 minutes, and the fibronectin coated stamps were gently placed onto the top of the array and left in contact for approximately 30 seconds. Following stamping, the post substrate was submerged in a 1:10 solution of phosphate-buffered saline (PBS) and Pluronic F-127 (BASF). Pluronic F-127 is a co-block polymer that adsorbed to the surface of the PDMS everywhere that did not already contain ECM. The result of these two treatments was a substrate that promoted cellular adhesion onto the post tops, while preventing attachment along the post sides or at the base of the array. Figure 2.4 shows a phase contrast image of a BPASMC adhered to an mPAD.

If fluorescently labeled posts were desired, the arrays could be submerged prior to cell seeding in a 1:10 solution of 50ng/ml Rhodamine B and DI water. Rhodamine B is a small (479 molar mass) hydrophobic fluorescent dye, which diffuses into the PDMS posts rendering them visible via fluorescence microscopy. Rhodamine B is preferable to other fluorescent molecules, such as the cell membrane stain DiI, which have been used previously [21, 25], as over time DiI will diffuse out of the posts and into the attached cell membranes, limiting post visibility. Although Rhodamine B will not diffuse into attached cells, this style of treatment resulted in staining of all parts of the PDMS array. Due to the finite depth of field associated with our long working distance objectives, the complete fluorescence coverage results in some level of background fluorescence from the bodies of highly deflected posts. In order to eliminate this background fluorescence, attempts were made to label only the post tops using fluorescently labeled gelatin, which is a fragment of collagen that possesses multiple binding sites for fibronectin [26]. However, upon using fluorescent gelatin, it was found that concentrations well above protocol were needed to produce even a weak signal from the post tops.

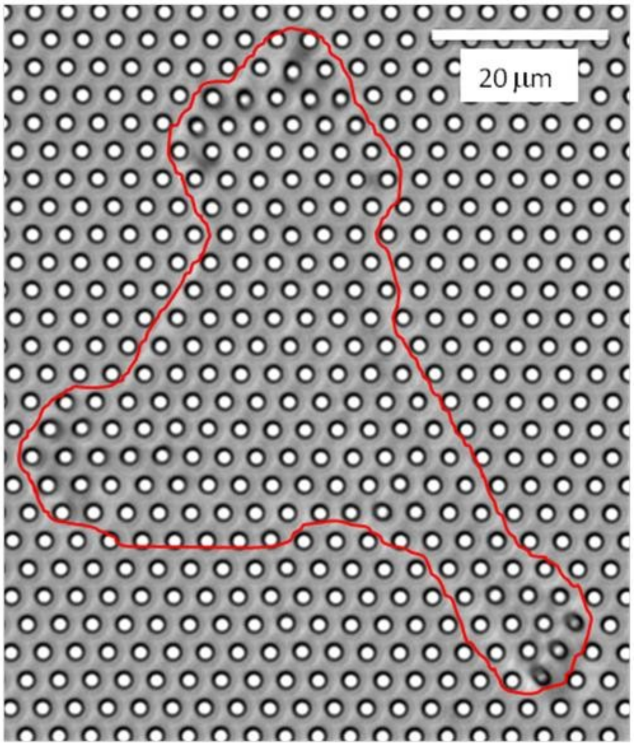

Figure 2.4: Phase contrast image of a BPASMC spread on the surface of a micropost array. The boundary of the cell can be seen as a white border, and is indicated in this image by a red trace.

2.2.2 Flexible mPADs

In order to apply strain to adhered cells while simultaneously measuring traction forces, PDMS post arrays were constructed on flexible PDMS membranes for application of stretch (Figure 2.5). PDMS was used to fabricate the membranes that served as the base for the arrays because uncured PDMS (that is not silane treated) will completely fuse with new PDMS upon curing. Therefore, post transfer from negative molds to PDMS membranes resulted in a single PDMS substrate with no risk of the posts delaminating from the membrane surface during stretch application. PDMS membranes were made using the wells of a standard 6-well cell culture plate as molds. These wells have a diameter of 3.5 cm, and application of 0.5 ml 1:20 PDMS resulted in a membrane with a central region approximately 300μm thick. A ratio of 1:20 was chosen in order to produce a more flexible substrate for application of vacuum induced deformation. Once the membranes were cured, flat nosed tweezers were used to detach the sides of the membranes from the walls of the 6-well plate, followed by gently peeling the membranes out of the wells. To assist in de-molding and prevent membrane tears, the wells were filled with enough ethanol to cover the membrane surface. Once removed, membranes were cut to size using a custom built die 13/16" (2.06 cm) in diameter. Membranes were trimmed in order to allow for loading into the critical point dryer used for substrate drying after post application.

Trimmed membranes were then placed into a flat sample container and micropost arrays were constructed on the top surface using 1:10 PDMS and negative molds, using the same procedure for posts constructed on a glass substrate. After curing, substrates were submerged in ethanol prior to removal of molds and critical point drying. With some modification, the same functionalization process described above was used for flexible mPADs constructed on membranes. With the entire substrate constructed from PDMS, the flexible mPADs were too buoyant to reliably remain submerged while treating and washing with water based solutions. This issue was resolved by using hollow PDMS cylinders placed on top of the membranes, around the post arrays. These cylinders stuck to and partially sealed with the membrane, allowing for solution to be placed inside the cylinder body, over the top of the post array. PDMS cylinders were fabricated by placing test tubes 1.5 cm in diameter vertically in a Petri dish, which was then filled with 1:10 PDMS and cured. After curing, a razor blade was used to cut cylinders from the bulk PDMS using the holes from the test tubes as the cylinder centers. While not critical, the cylinder walls were generally cut to be approximately 5 mm thick.

Notably, it was not possible to use fluorescent labeling of the microposts on the flexible substrates. The membranes used for stretching were in contact with sterile vacuum grease during cell seeding and experimentation (see Section 2.23 below). Due to the hydrophobic nature of Rhodamine B and other suitable molecules used for staining PDMS, diffusion out of the PDMS posts and into the grease occurred very rapidly, causing highly decreased post visibility. To avoid this, methods of data acquisition using white light imaging were developed and used.

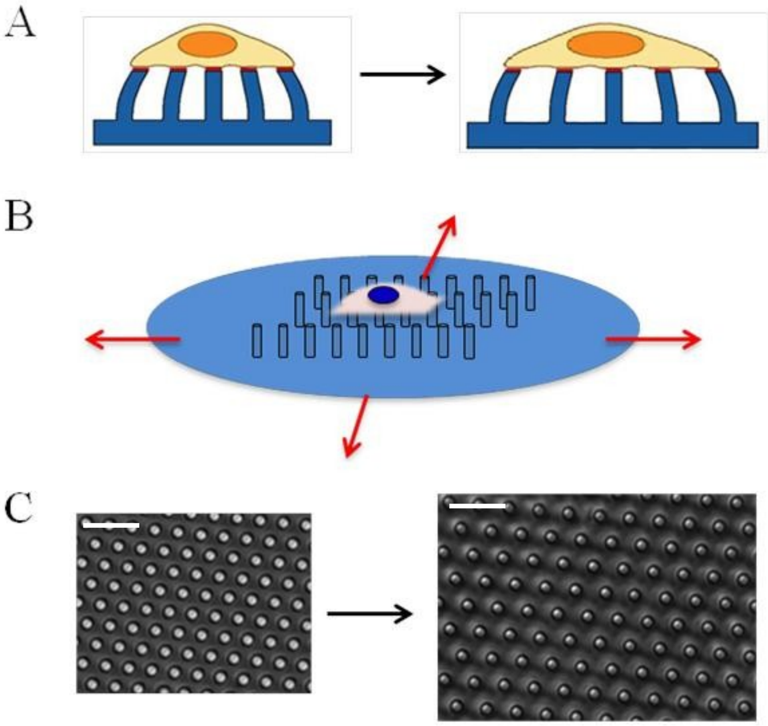

Figure 2.5: Two dimensional (A) and three dimensional (B) schematics of a cell adhered to a flexible mPAD. (C) Phase contrast images of a flexible mPAD before and after application of 40% biaxial stretch, scale bar is 10µm.

2.2.3 Stretch Culture Chamber

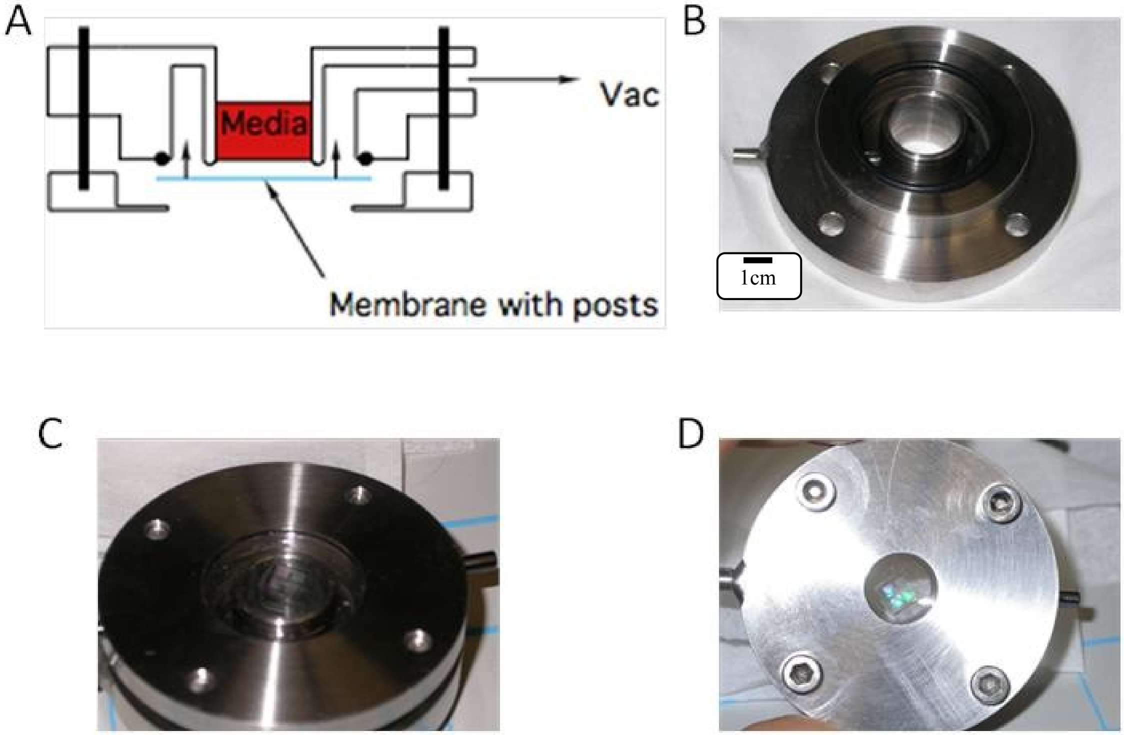

Figure 2.6: Flexible mPAD stretch culture device. (A) Schematic of device showing upper and lower pieces with membrane and media location. (B) Bottom view of the top piece of the chamber showing the vacuum chamber that surrounds the central well and an O-ring to seal the membrane edges. (C) Bottom view of the whole device with flexible mPAD. (D) Top view of device with flexible mPAD.

Application of stretch to cultured cells required a means to apply strain to a flexible culture substrate while maintaining suitable culture conditions and allowing for extraction of data. This was achieved through design of a custom-built culture chamber in which the flexible culture substrates described above were mounted and stretched while under constant observation. As seen in Figure 2.6, the device consisted of a central hole 0.5 inches in diameter surrounded by a cylindrical vacuum chamber 0.5 inches tall and 0.1675 inches wide. Once mounted, the PDMS membrane served as the base of a central "culture well" that was open for viewing on an inverted microscope. The stretch chamber was first fabricated from stainless steel, with later productions using polycarbonate, which was more cost efficient to manufacture.

Substrate stretch was achieved through application of vacuum pressure via a programmable syringe pump to the portion of the membrane surrounding the central culture well that was exposed to the vacuum chamber. In order to allow the membrane to slide across the base of the central cylinder during strain, a small amount of vacuum grease (Corning), autoclaved to ensure sterility, was applied to the bottom rim of the well. Grease application also served to seal the central chamber, allowing for containment of culture media. During cell seeding and prior to connecting the stretch chamber to a syringe pump, the stretch chamber had to be stored in such a way that the membrane was forced to remain in contact with the base of the inner cylinder. This was achieved using a modified Petri dish with a raised center region that contacted the membrane and supported the weight of the device. Once the stretch chamber was moved to the microscope stage and connected to a syringe pump, applying pressure equal to 0.2 psi below ambient conditions served to create the seal between the membrane and the chamber without imposing strain on the substrate. The device could then be moved out of the Petri dish and put in place for viewing on the microscope.

2.2.4 Patterned mPAD Functionalization

mPAD surfaces were selectively patterned to promote the adhesion of cultured cells in a pair configuration for cell-cell interaction studies (Figure 2.7 B). Controlled regions of fibronectin were applied to the mPAD surface using the aforementioned stamping technique in conjunction with patterned PDMS stamps (Figure 2.7 B). Patterned PDMS stamps were molded from SU-8 (Micro Chem, Newton MA) masters that were pattered using standard photolithography techniques. Briefly, a standard silicon wafer was spin coated with SU-8 10 at 2000 rpm for 30s, pre-baked @ 65C for 2 minutes followed by a soft-bake @ 95C for 5 minutes. The substrates were then exposed for 5s to obtain ~100-150 J/m^2 , and then post exposure baked for 1 minute @ 65C and 2 minutes @ 95C before being developed using MicroChem's SU-8 developer.

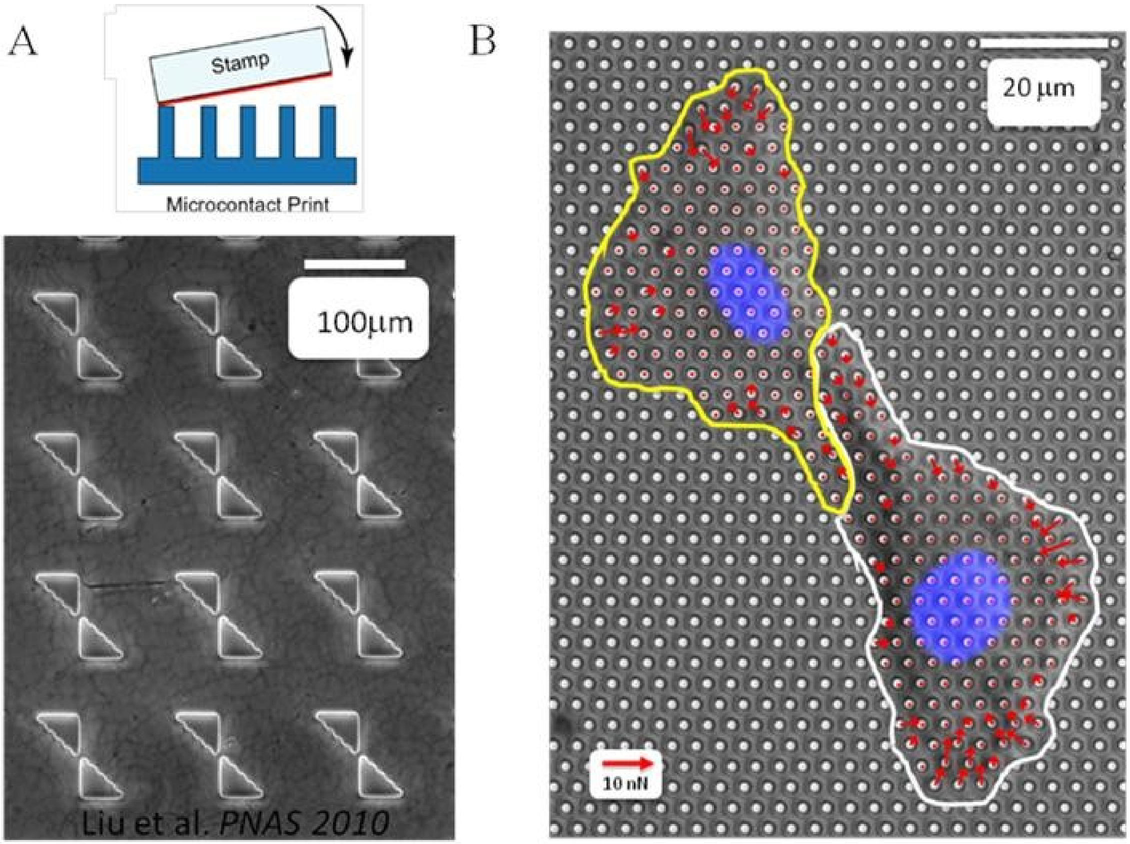

Liu et al. *PNAS 2010*

Figure 2.7: (A) Schematic of stamping technique used on mPADS (top), and a phase contrast image showing the surface of a bow-tie patterned PDMS stamp (bottom). (B) Phase contrast image of a BPASMC cell pair adhered to patterned micropost array. Associated force vector field is in red, fluorescently labeled cell nuclei are colored blue.

2.3 Experimental Techniques

2.3.1 Cell Culture on Microposts

Cells in suspension seeded onto functionalized micropost arrays will attach and spread across the micropost tops (Figure 2.4). For experiments requiring fully spread cells, substrates were incubated overnight (10-12 hours) following seeding. To obtain isolated cells surrounded by a sufficient number of empty posts as required for analysis (Section 2.3.2), 50 µl drops of suspended cells at an approximate concentration of 10,000 cells/ml were applied to a micropost substrate submerged in 3-4ml of media, and the density above the array was checked via microscopy prior to incubation. Experiments measuring cellular traction forces were conducted on a Nikon Eclipse TE-2000 microscope with epi-fluorescence attachment, and images were acquired using a Photometrics CoolSnap HQ CCD camera. Micropost substrates were placed into glass bottom culture dishes before transfer to the microscope stage. A small amount of vacuum grease (Corning), sterilized by autoclaving, was used to keep the micropost substrate secure and immobile in the culture dish during imaging. Experiments not involving external connections or stage mounted devices were performed using a custom built stage mounted chamber and live cell incubation system (LiveCell, Westminster MD). This system enclosed the microscope stage in order to regulate and maintain culture conditions of 37C and either 5% or 10% CO_2, depending on cell type. Single cells were located on the array using phase contrast microscopy and a 10x objective, followed by imaging of both the cell and the underlying post array at either 40x or 60x using either phase contrast (Figure 2.8 B), fluorescence (Figure 2.8 A), or bright field (Figure 2.8 C) microscopy.

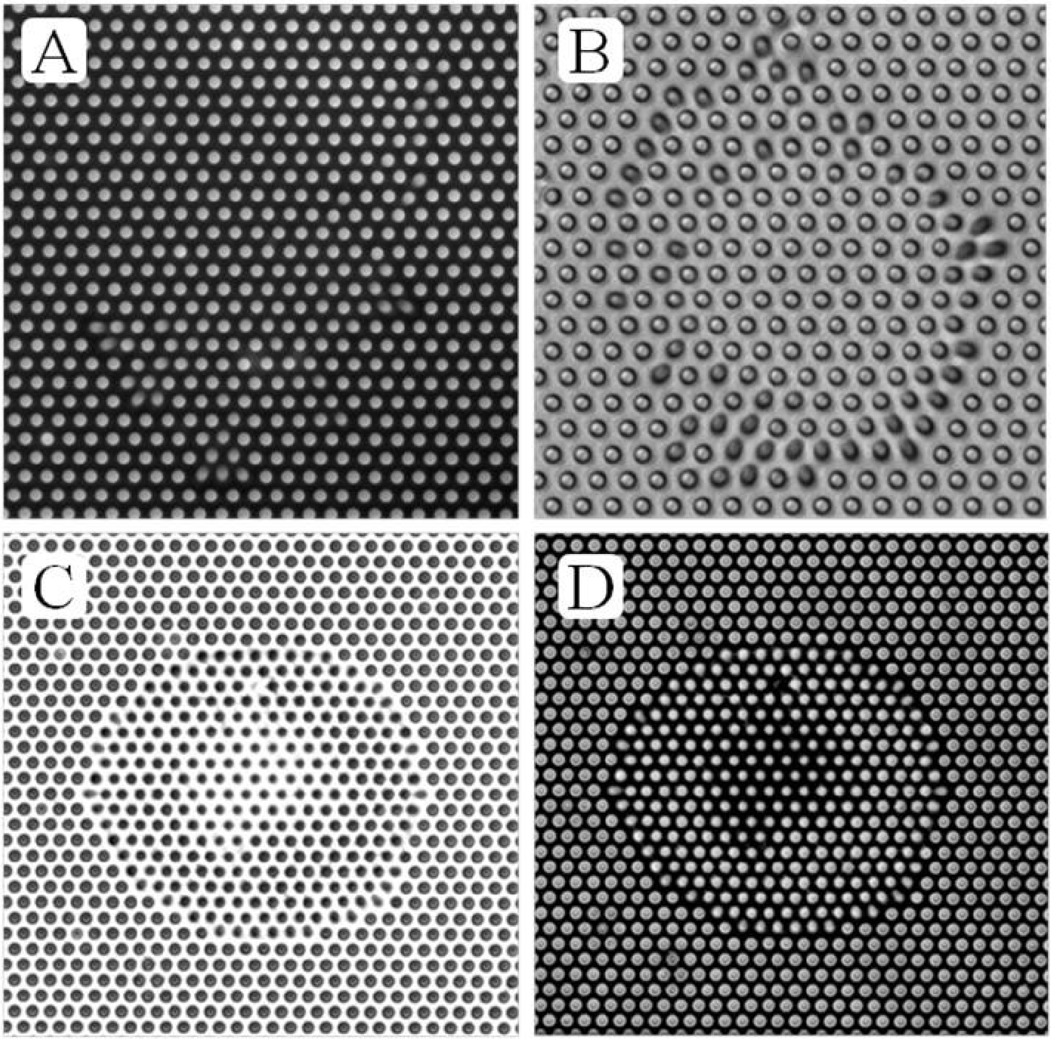

Figure 2.8: Fluorescence (A), phase contrast (B), and bright field (C) images of single cells adhered to mPADs. The bright field image was then inverted (D) to obtain light posts on a dark background.

The most robust method for imaging the post array was to use bright field microscopy, without any phase contrast, in conjunction with pre-processing prior to analysis. This was achieved on our microscope by using the “M” setting at the front focal plane of the microscope’s condenser. This particular setting is meant for use with DIC microscopy, and therefore does not contain a phase ring. Using this method, resulted in an image where individual microposts were dark on a light background (Figure 2.8 C). This method resulted in images with very low background and the least amount of distortion caused by thick regions of cell body, as well as removing the need for fluorescently labeled posts. Prior to analysis, these images required inversion of data values so that posts appeared light on a dark background (Figure 2.8 D). All post array images of any type undergo “rolling ball” background removal prior to analysis (Figure 2.9). This background subtraction algorithm uses a sliding paraboloid with a user-defined radius of curvature to remove unwanted background signal. This process can be thought of as a ball rolling on the underside of a pixel intensity plot, resulting in all pixels coming in contact with the ball’s surface having their intensity value set to 0. Therefore, the ball’s radius was defined such that the objects of interest, in this case, microposts, are smaller than the selected radius. This way, the ball does not “fall in” to the intensity peaks, and instead removes all background noise that exists in between individual microposts.

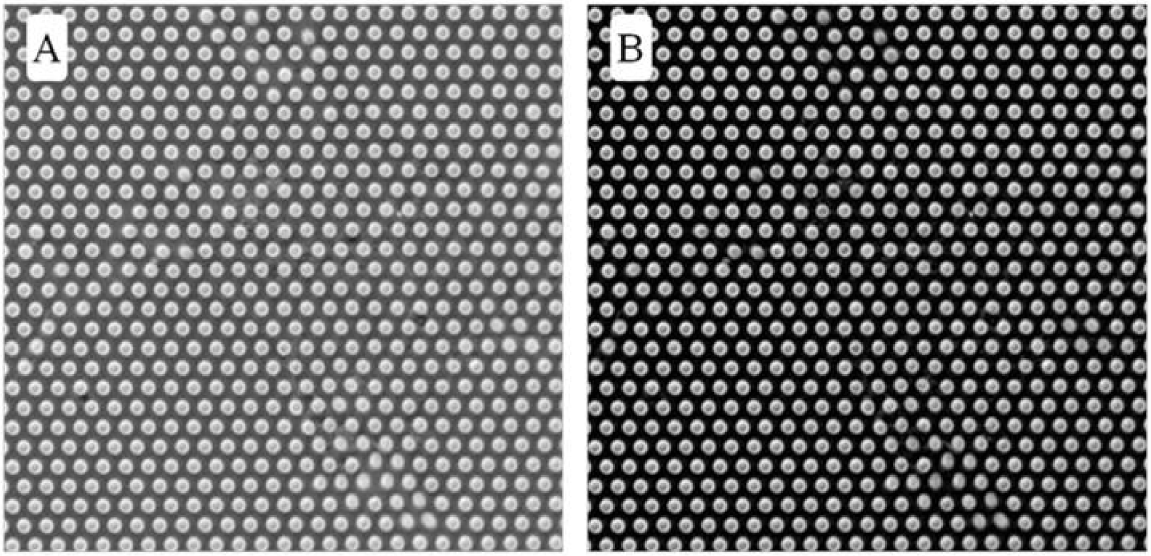

Figure 2.9: Inverted bright field images showing an mPAD before (A) and after (B) rolling ball background removal.

2.3.2 Micropost Image Analysis and Data Reduction

Micropost array images were analyzed and cellular traction forces calculated using custom software written in Igor Pro (Wavemetrics) (Figure 2.10). The analysis began with numerical indexing of all posts in a selected region of interest (ROI) that contained the posts to which a cell was adhered, as well as a large number of empty posts surrounding the cell.

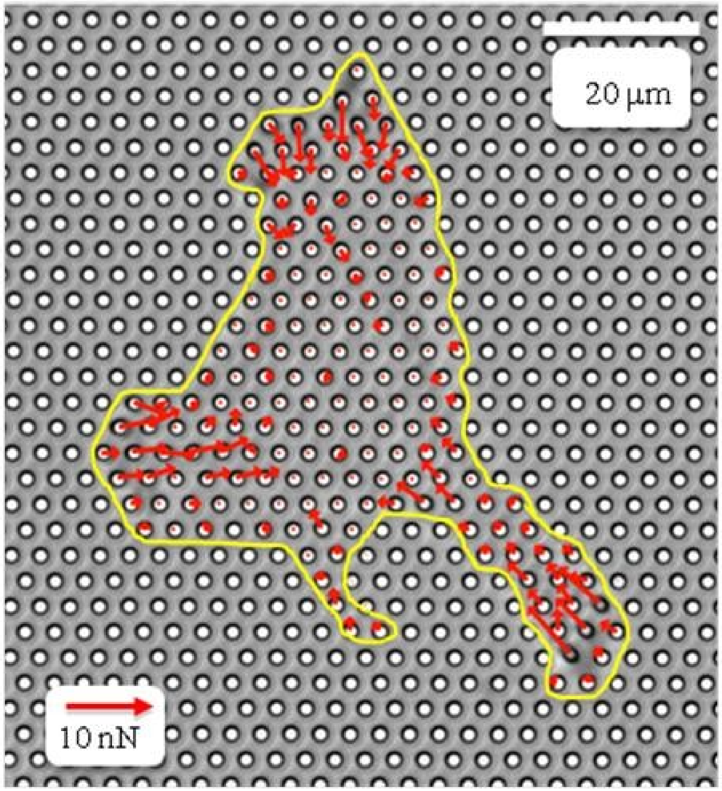

Figure 2.10: Phase contrast image of BPASMC adhered to a micropost array with calculated force vectors present for each post in contact with the cell.

Following ROI selection, the center location of each post was determined via two dimensional Gaussian fitting (Figure 2.11 B, C) [25]. Posts to which a cell was adhered were deflected by the cell's contractile forces (Figure 2.11 E). These deflections were measured relative to each cell post's un-deflected position. Un-deflected positions were interpolated from the intersections of best fit lines determined by the positions of all empty posts (Figure 2.11 F) surrounding, but not in contact with, the cell. Once all cell post deflections were measured, the force acting on each individual post was calculated and a vector map for the entire cell was then overlaid on the post array images (Figure 2.10). Forces are calculated by treating each post as a simple spring, F = -kx. Here k is the “spring constant” for small deflections as determined by bending of individual posts using calibrated glass micropipettes moved by a piezoelectric controller [21]. For all of the mPAD experiments in this work, the microposts used were 5.7μm tall, 1.8μm in diameter with a 4μm post-to-post spacing, and had a spring constant of 22nN/μm. For a whole cell scalar measure of cellular contractility, the measured post deflections were used to calculate the strain energy stored in each deflected post, which were then summed over all posts that the cell was adhered to, $E = \sum_i \frac{1}{2} k x_i^2$. These procedures were performed for each post array image, and the software had the capability of analyzing a series of images in order to observe traction force dynamics over time.

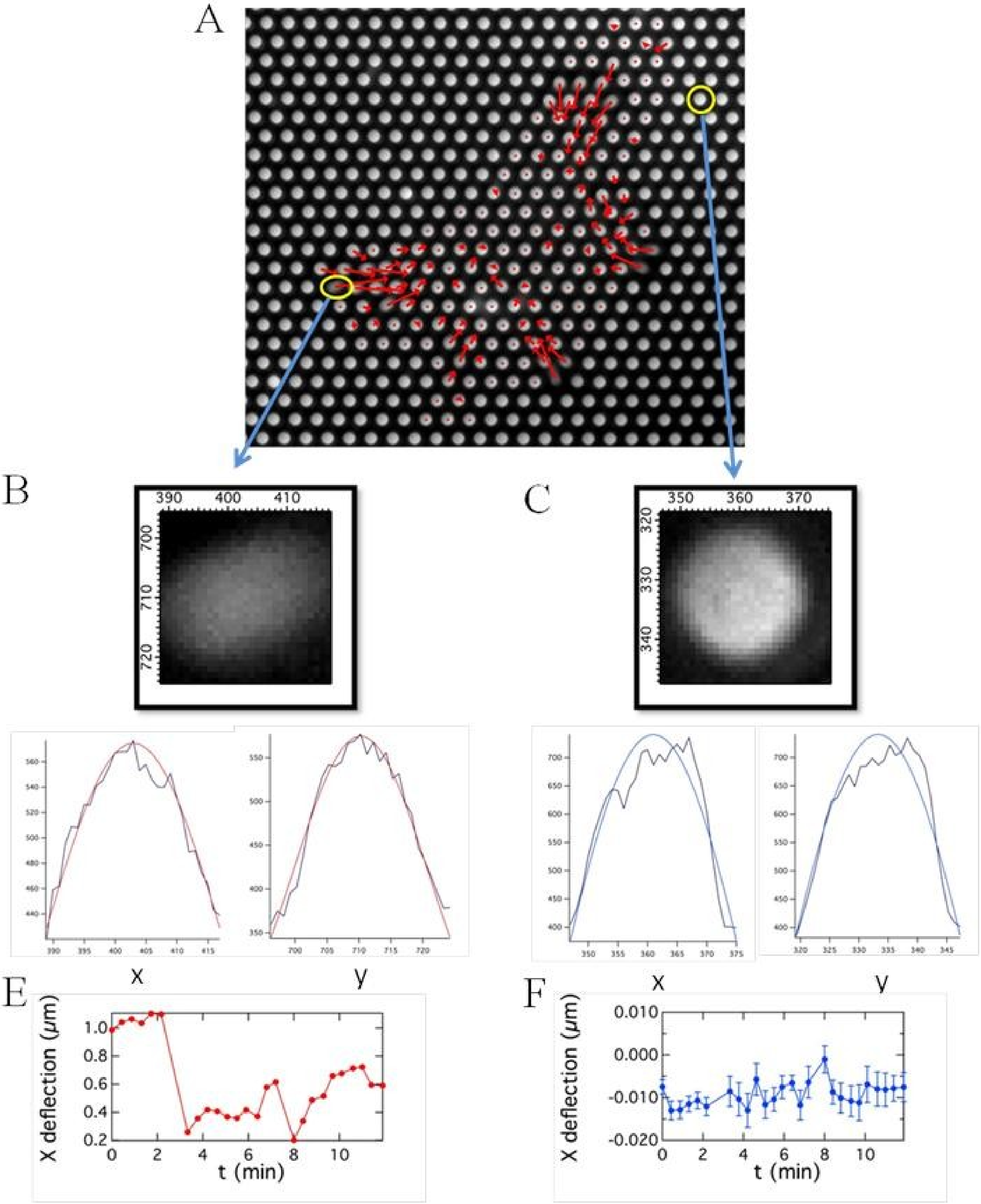

Figure 2.11: Analyzed fluorescence image showing force vector map of adherent cell (A). Below are magnified images of a cell-attached (B) and empty (C) micropost, and cuts in the x-direction and y-direction with the associated Gaussian fits. Time traces of each post's center location over the course of an experiment for the cell-attached (E) and empty (F) posts. Note the y-axis scaling on these plots, where (F) shows the noise level for the background post, and (E) shows true deflections due to application of force.

2.3.3 Measurement of Cell-Cell Force

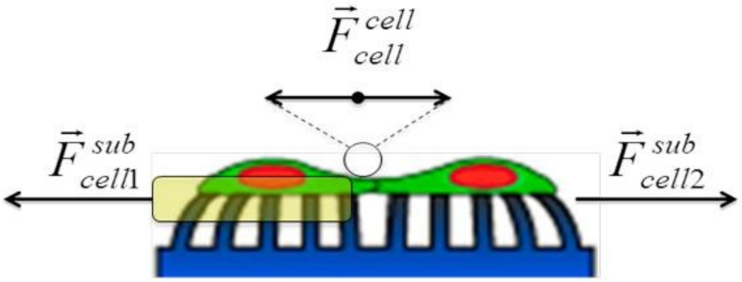

Figure 2.12: Schematic diagram of a cell pair adhered to an mPAD (ref Liu). Force vectors indicate cell-substrate forces for each cell, as well as the cell-cell force acting between the cells.

Cells remained stationary when adhered to the post arrays over short time scales, and therefore must have experienced a net force of zero across the cell body. For cells arranged in a pair configuration, determination of net cell-substrate force: $\vec{F}_{cell}^{sub} = \sum_i k\vec{\delta}$, which must by Newton's third law be equal and opposite to the net cell-cell force: $\vec{F}_{cell1}^{sub} = -\vec{F}_{cell1}^{cell2} = \vec{F}_{cell2}^{cell1} = -\vec{F}_{cell2}^{sub}$, cell-substrate forces measured via mPADs enabled calculation of cell-cell forces: $\vec{F}_{cell1}^{sub} = -\vec{F}_{cell2}^{cell1}$.

Chapter 3 Cardiac Fibroblast Contractility

3.1 Introduction

This chapter describes experiments using mPADs to measure the mechanical output of cardiac fibroblasts. The goal of these studies was to elucidate the role of fibroblast contractility in mechanical coupling of cardiac fibroblasts and cardiac myocytes. While completed as part of a cell-cell interaction study through collaboration with the lab of Leslie Tung in the Johns Hopkins University Department of Biomedical Engineering, taken alone, the following measurements provide a comprehensive characterization of the mechanical properties of neonatal rat ventricular fibroblasts (cardiac fibroblasts) using mPADs. These results are described in two publications [27, 28].

Experiments conducted in the lab of Leslie Tung used a cardiac tissue model consisting of a patterned cardiac myocyte monolayer supplemented with either cardiac fibroblasts (CFs) or cardiac myofibroblasts (CMFs) (Figure 3.1 A). The purpose of this tissue model was to simulate cardiac muscle tissue that naturally contains both myocytes and fibrobloasts/myofibroblasts. Myocyte beating was induced through application of an electrical signal, and a voltage sensitive dye was used to measure the velocity with which the applied electrical signal propagated through the model tissue. These experiments showed significant slowing of conduction velocity between control monolayers supplemented with CFs and tissues supplemented with CMFs (Figure 3.1 B), which simulate fibrotic tissue [27]. These changes were hypothesized to be a result of mechanical coupling between the myocytes and the CF's/CMF's, through which CMF contractile forces act on and open stretch activated ion channels located within the myocyte membrane. In order to investigate this hypothesis, conduction velocity in model tissues was measured under various experimental conditions that altered either CMF contractility, or aspects of the proposed coupling mechanisms between the CMFs and cardiac myocytes. The experiments described here measuring CMF force generation on mPADs provided a direct measurement and characterization of CMF mechanical output under experimental conditions that corresponded to those used in the conduction velocity experiments.

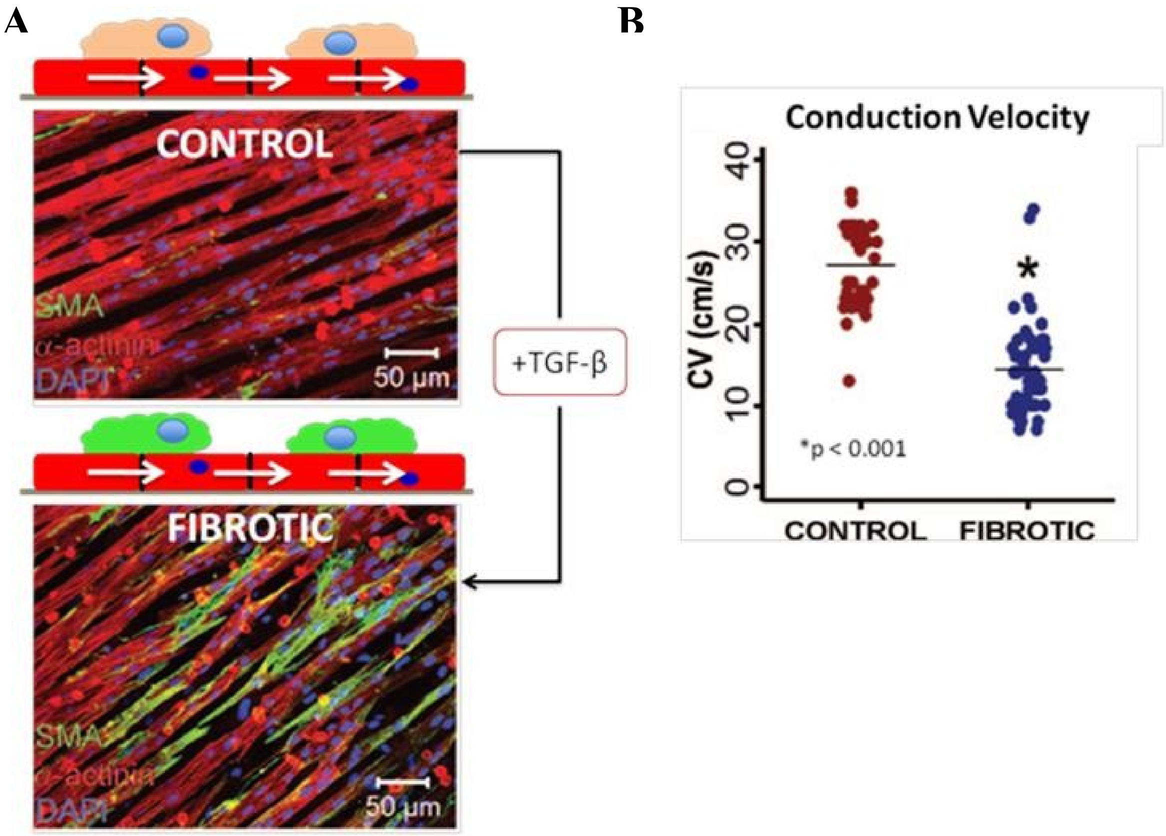

Figure 3.1: (A) Fluorescence images of control and fibrotic model cardiac tissues. α-actinin in red denotes cardiac myocytes, α-SMA in green denotes CMFs, and all cell nuclei are shown in blue. Nuclei not associated with a cell positive for α-actinin or α-SMA denotes a control CF. (B) Plot of conduction velocity shows significant slowing in tissues supplemented with CMFs (fibrotic) as compared with tissues supplemented with CFs (control). (From [27]) (Data courtesy of Susan Thompson)

3.2 Methods

3.2.1 Short Duration Treatments

The effects of various drug treatments on cellular contractility were observed by imaging cells in normal conditions, followed by incubation with drug containing media, and then imaging of the same cells following treatment. Because the micropost substrates were moved into an incubator for the treatment step, care was taken to allow for accurate identification of cells that were originally imaged. Depending on the length of treatment time, cells may have changed shape or migrated on the post substrate. Therefore, during the initial imaging procedure, cell locations, morphologies, and substrate orientation were carefully documented in order to ensure imaging of the same set of cells after treatment. Once imaging was completed, the images of each cell were then analyzed to determine changes in cellular contractility.

3.2.2 Long Duration Treatments

Cell treatments requiring incubation time greater than two hours greatly reduced the feasibility of tracking changes in contractility for specific individual cells. The translational and morphological changes that cells exhibited over multiple hour treatment times made re-location of specific cells following treatment impractical. In these cases, cells were treated prior to seeding on mPADs, and average total strain energy per cell was compared with that of a control group from the same culture that was not treated prior to seeding on mPADs.

3.2.3 Traction Force Dynamics During Cell Spreading

In order to observe traction force dynamics during cell attachment and spreading, cells were seeded onto mPADs and imaged without prior incubation. In contrast to the standard stamping procedure outlined previously (Section 2.2.1), which only deposited ECM onto the post tops, micropost arrays were immersed in 50ug/ml fibronectin solution for 1 hour, which resulted in a fully ECM-coated substrate. Because not all cells contacting the array would successfully spread, and given the need for real time measurement during the process, this method was chosen because it increased the probability of observing a cell that would successfully spread. To further increase this probability, cells showing early process development were chosen for imaging 10 minutes after seeding. Images were taken once every minute using a Nikon TE2000 microscope and a 60x objective. The thickness of a cell in the process of spreading caused a distorted view of the post tops when viewed using phase contrast imaging. For this experiment mPADs were stained using Rhodamine B, or bright field imaging with post-processing (Section 2.3.1). Cell spreading area was also tracked using phase contrast microscopy in order to provide a measure of spreading progress.

3.3 Results

3.3.1 TGF-β

In vivo, fibroblast differentiation into the more contractile myofibroblast phenotype is facilitated by the release of transforming growth factor beta (TGF-β) [20] . This transformation was facilitated in vitro through supplementation of culture media with 5ng/ml TGF-β for 48-72 hours prior to seeding on mPADs. Cardiac fibroblasts that have been treated with TGF-β will be referred to as CMFs throughout this work. In order to directly measure the effect of TGF-β treatment on fibroblast contractility in vitro, CMFs were cultured on mPADs, imaged, and their contractile forces measured. Whole cell strain energy ($E = \sum_i \frac{1}{2} k x_i^2$) was averaged for all cells of a TGF-β treated CMF population for comparison with the average strain energy of a population of control CF's from the same culture that were not exposed to TGF-β. Control CFs exhibited a wide range of strain energies imparted to the mPAD, a representative sample of which is shown in Figure 3.2. While the TGF-β treated population also showed a wide range of contractility (Figure 3.3), treatment resulted in a 50% increase in average CMF contractile energy imparted to the elastic micropost arrays (E=183 ±12fJ [n=100]) as compared with control CF's (E=120±8fJ [n=93])), $p = 10^{-5}$.

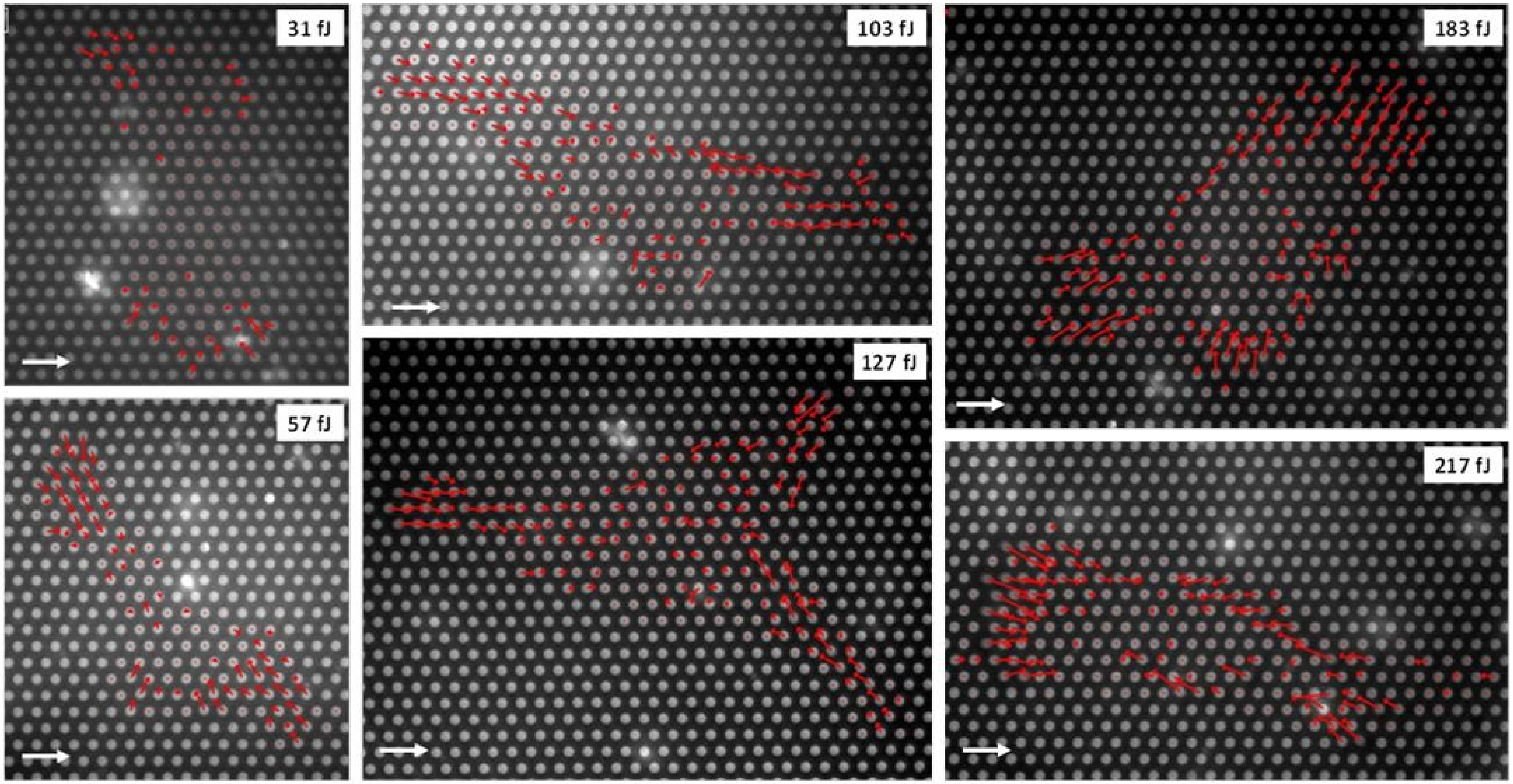

Figure 3.2: Force vector maps of cardiac fibroblasts overlaid onto fluorescence images of micropost arrays. Representative selection shows the wide range of contractility observed. Scale vector is 10nN.

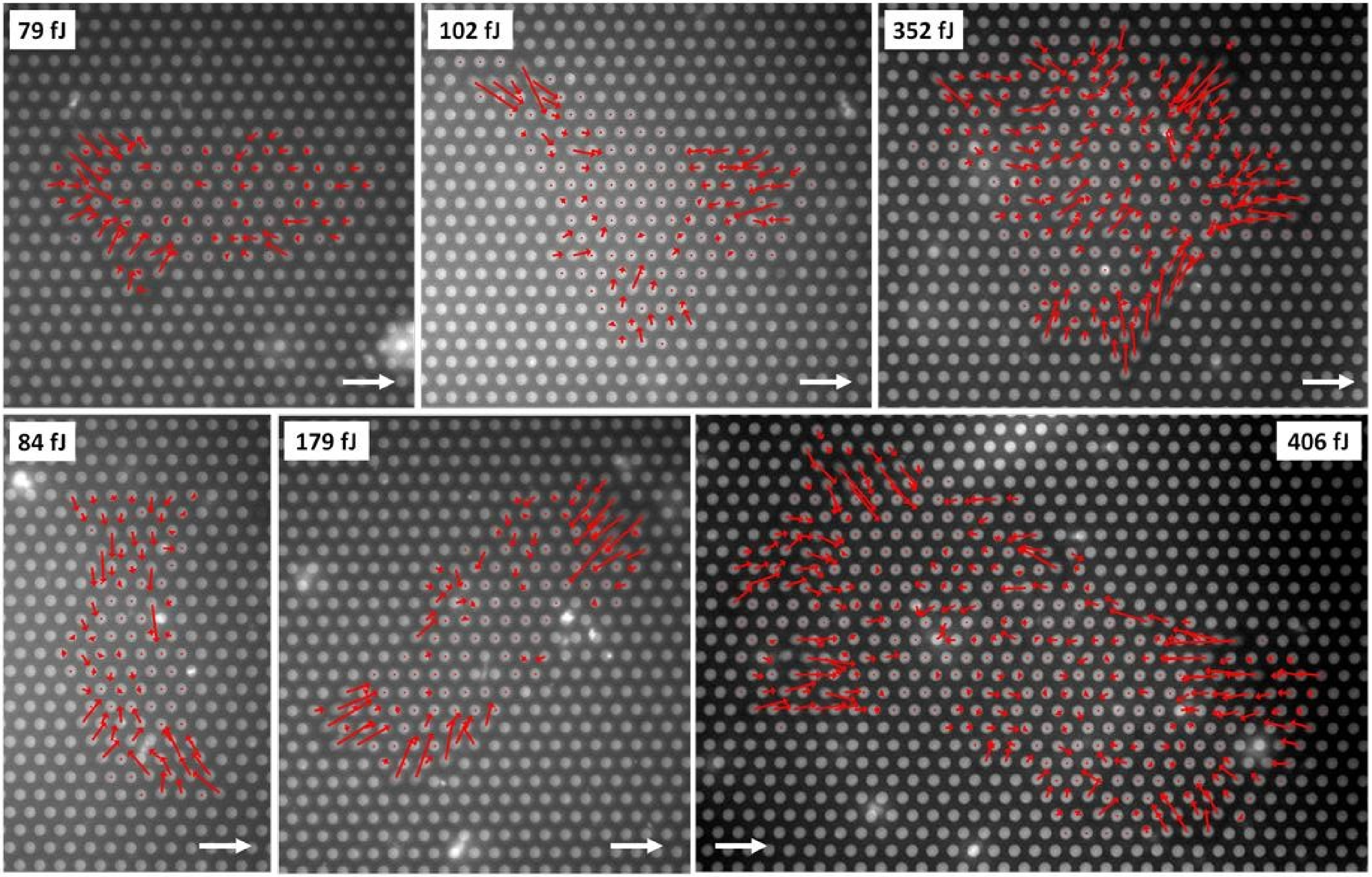

Figure 3.3: Force vector maps of TGF-β treated cardiac myofibroblasts overlaied onto fluorescence images of micropost array. Representative selection shows the wide range of contractility observed. Scale vector is 10nN.

The large range of contractile energies observed caused considerable overlap in the whole cell strain energy distributions between the two populations. A cumulative energy distribution serves to clearly convey the difference in contractile output between the cells in these two populations (Figure 3.4). This distribution shows the probability (y-axis) that a cell in a given population will have a whole cell contractile energy greater than or equal to a given energy value (x-axis). The vertical separation between the control and TGF-β traces shows a greater probability of finding more contractile cells in the TGF-β treated population.

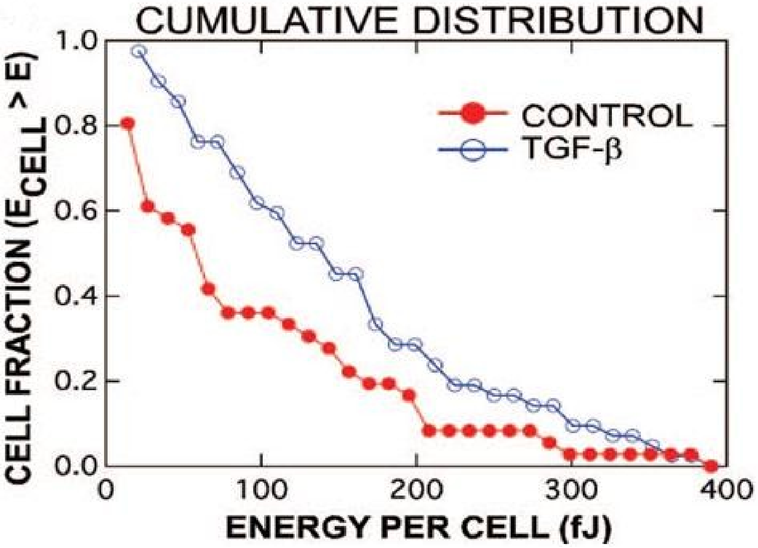

Figure 3.4: Cumulative distribution shows the probability (y-axis) that a cell in a given population will have a whole cell contractile energy greater than or equal to a selected value (x-axis). The vertical separation between the control and TGF-β traces shows increased contractility due to treatment. (From [27])

3.2.2 Blebbistatin

As mentioned previously, cells generate contractile forces primarily through the action of myosin motors within the actin cytoskeleton (Section 1.1.2). The drug blebbistatin inhibits myosin II activity by blocking the myosin head with a complex that has low affinity for actin [29], thus reducing a cell's ability to generate contractile forces.

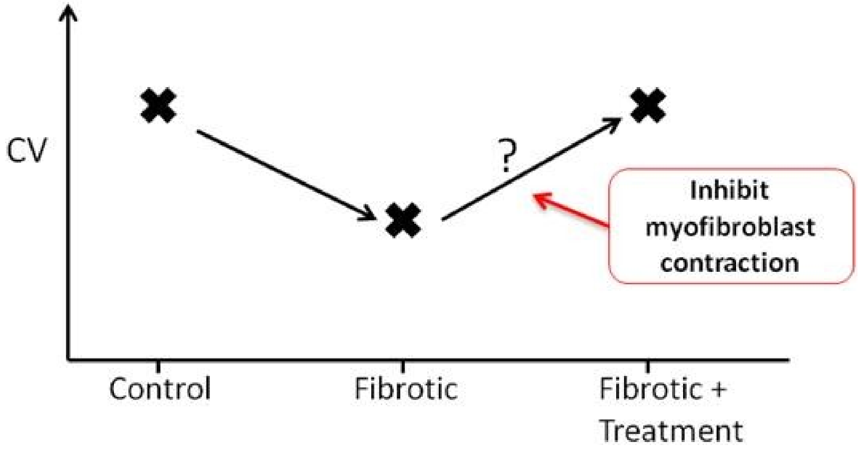

Figure 3.5: Graphical schematic of the hypothesized result of CMF contraction inhibition on fibrotic tissue conduction velocity (CV).

To elucidate the role of CF contractility within the mechanical coupling hypothesis, blebbistatin was added to culture media in order to reduce myofibroblast contractility. If the observed conduction slowing was a result of the action of myofibroblast contractile forces acting on the myocytes, blebbistatin treatment would serve to increase conduction velocity in fibrotic model tissues (Figure 3.5). Experiments conducted in the Tung lab using model tissues supplemented with blebbistatin-treated CMFs found a significant increase in conduction velocity as compared to tissues supplemented with untreated CMF's (Figure 3.6). Quantification of the effects of blebbistatin treatment on the contractility of CMFs was performed through direct measurement using mPADs.

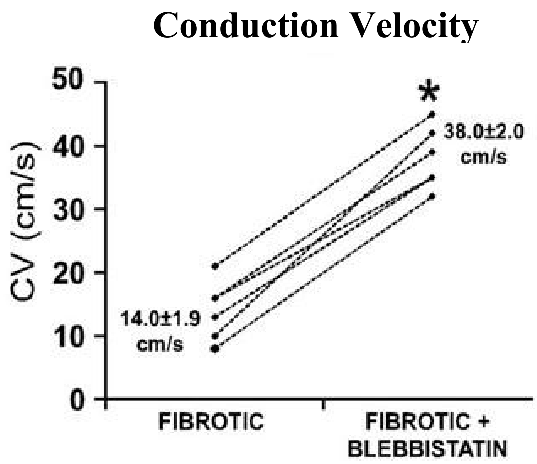

Figure 3.6: Comparison of conduction velocity on fibrotic model tissues containing CMFs before and after treatment (n=5). Dashed lines indicate individual model tissues, and connect measurements before and after Blebbistatin treatment. 30 minute treatment with Blebbistatin resulted in an increase in conduction velocity, a reversal of the effects of CMF supplementation. (From [27]) (Data courtesy of Susan Thompson)

CMFs cultured on mPADs were imaged before and after treatment with 100 μM Blebbistatin for 30 minutes. Representative data for four CMF cells are shown in Figures 3.7 and 3.8. The uniform reduction in cell-substrate contractile forces following Blebbistatin treatment can be clearly seen in each case.

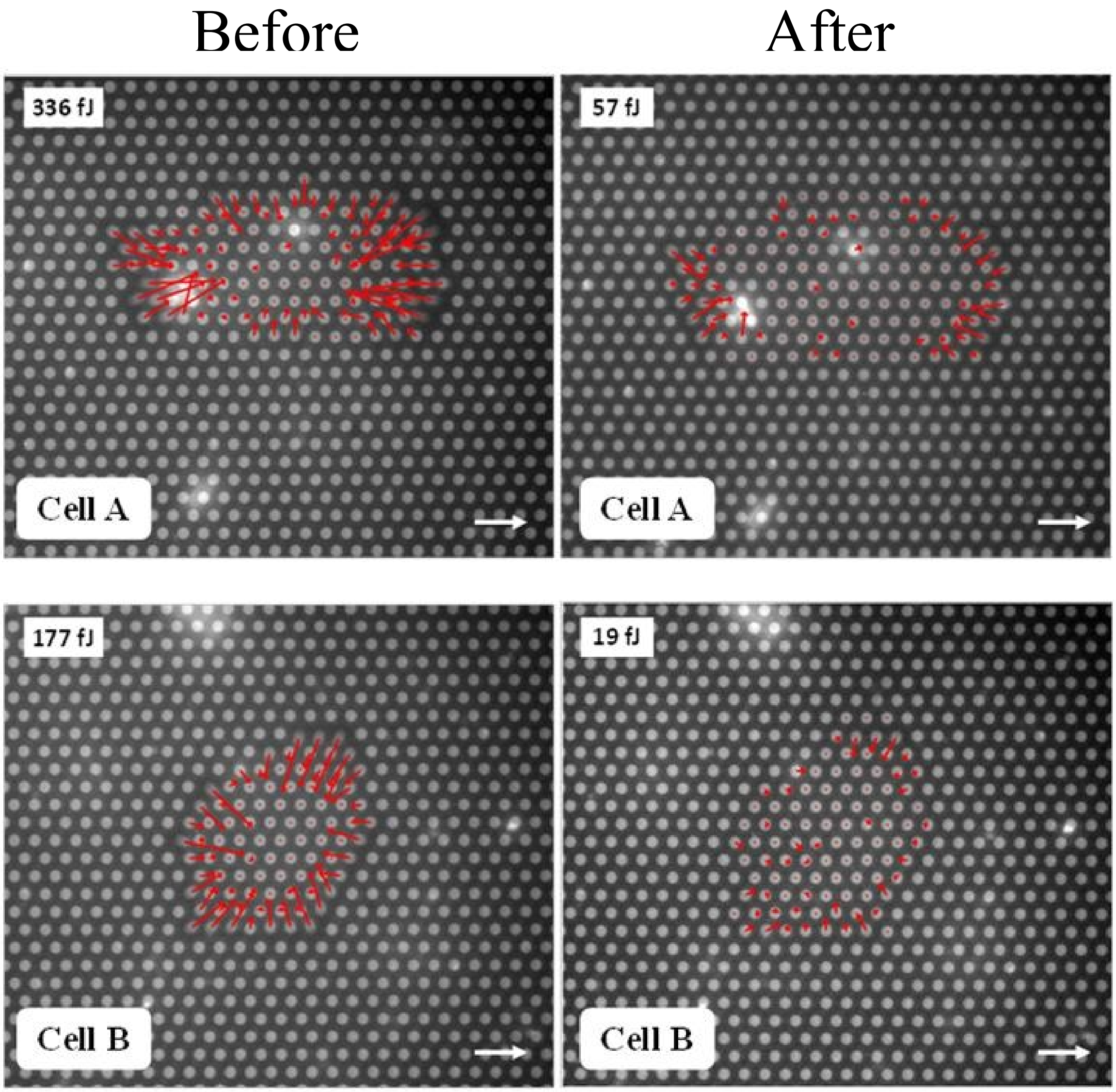

Figure 3.7: Force vector plots of two CMFs before and after Blebbistatin treatment showing reduction in contractile forces. Inset is whole cell strain energy. Scale vector is 10 nN.

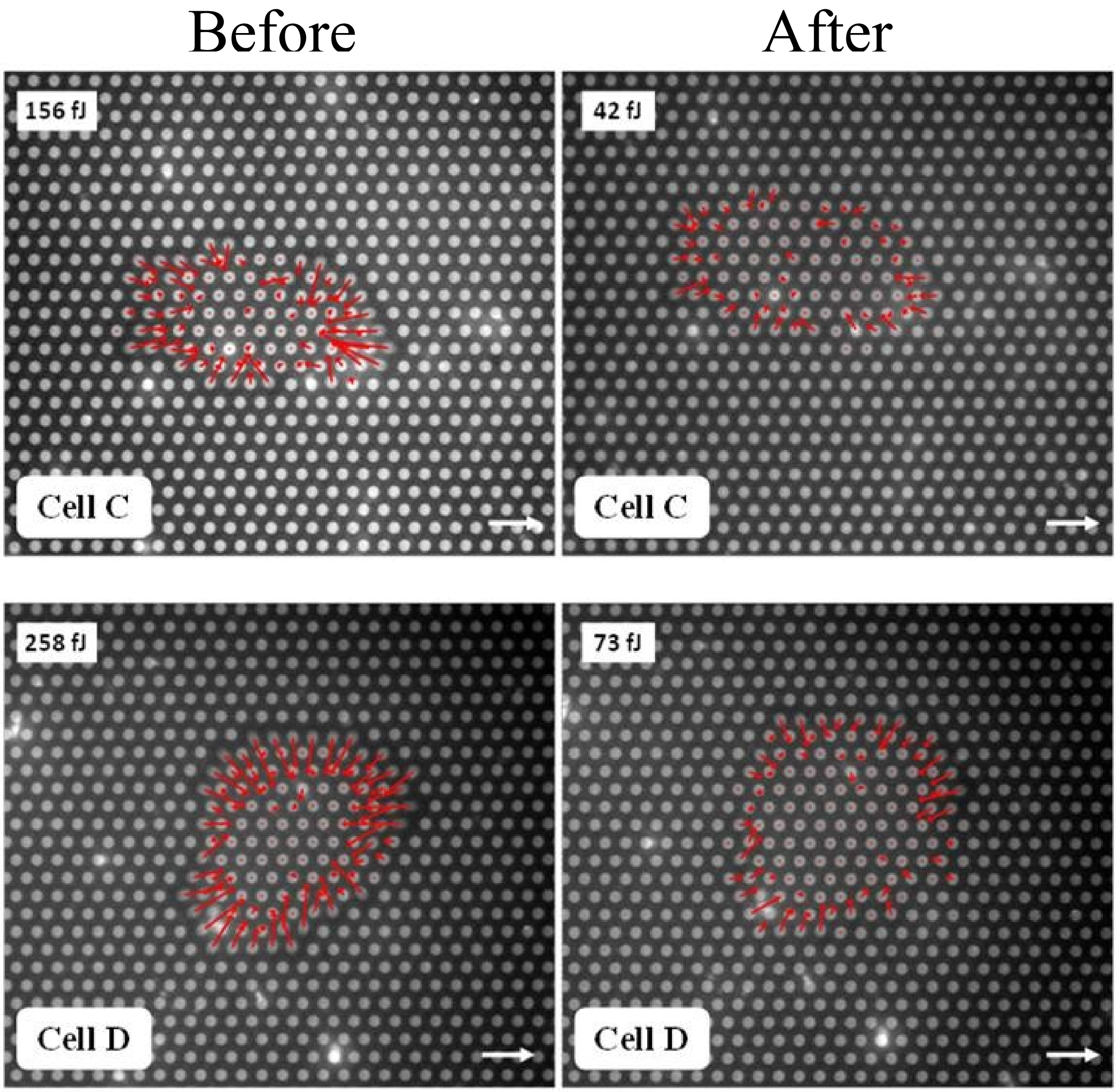

Figure 3.8: Force vector plots of two CMFs before and after Blebbistatin treatment showing reduction in contractile forces. Inset is whole cell strain energy. Scale vector is 10 nN.

The result of Blebbistatin treatment for all cells measured, quantified through the change in strain energy, is shown in Figure 3.9. Each cell showed a significant drop in strain energy. Overall, there was an average reduction in strain energy of 74.5%, from E = 278 ± 38fJ to E = 71 ± 14fJ (n=9) (Figure 3.9).

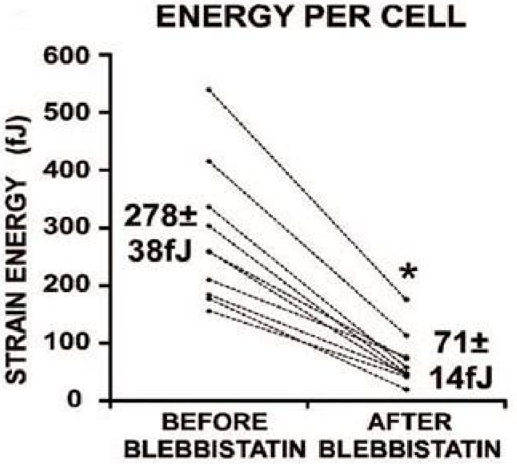

Figure 3.9: Change in total cell strain energy for CMFs (n = 9) using mPADs. Blebbistatin treatment results in a 74.5% reduction in contractile output. (From [27])

3.3.3 Mechanosensitive Channel Blockers (Gadolinium, Streptomycin)

Mechano-sensitive channels (MSCs) are transmembrane ion channels that open or are otherwise altered as a result of mechanical stimulus, allowing for passage of ions between the cytoplasm and the extracellular space. MSC function can be inhibited in the presence of certain MSC blockers, such as gadolinium and streptomycin, as used in this study. For example, gadolinium ions have been shown to block MSCs through mechanisms that limit the channel open time, reduce the current through open channels, and inhibit channel opening [30].

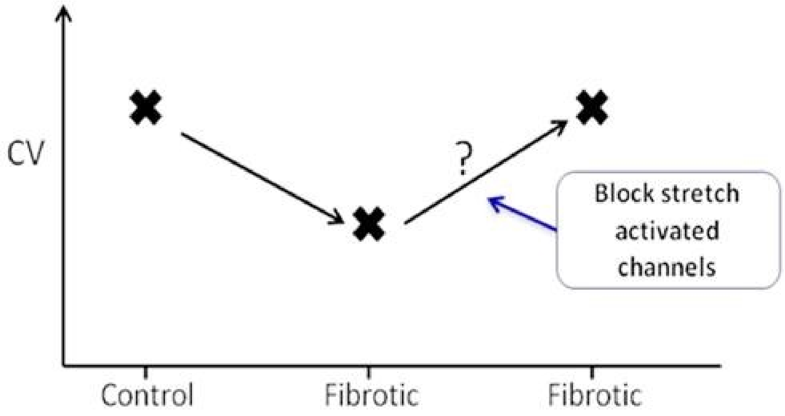

Figure 3.10:Graphical schematic of the hypothesized result of blocking mechano-sensitive channels in myocyte membranes on fibrotic tissue conduction velocity (CV).

These treatments served to determine the effect of inhibiting the *action* of CMF contractile forces acting on the cardiac myocytes, without interfering with CMF force generation (Figure 3.10). MSC blocker treatment on cardiac tissues resulted in an increase in conduction velocity, consistent with inhibition of MSC-mediated CV slowing through mechanical interactions (Figure 3.11).

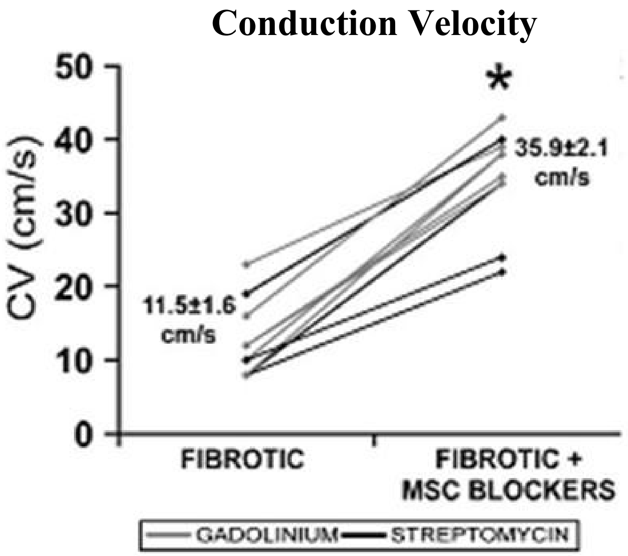

Figure 3.11: Changes in conduction velocity on fibrotic model tissues containing CMFs. Supplementation with gadolinium (n=5) and streptomycin (n=4) resulted in an increase in conduction velocity, a reversal of the effects of CMF supplementation. (From [27]) (Data courtesy of Susan Thompson)

In conjunction with conduction velocity experiments, mPAD experiments were used to measure MSC blocker effects on CMF contractility. Changes in total cell strain energy for 10 CMFs before and after treatment with 50µM gadolinium for 30 minutes resulted in no significant effect on CMF contractility. Four cells from this experiment are shown in Figures 3.12 and 3.13; none showed changes outside the normal range of fluctuations in contractile forces or strain energy over such an interval. Treatment with streptomycin under the same protocol yielded similar results, as illustrated for four representative cells in Figures 3.14 and 3.15. The results for the changes in strain energy for all cells measured in both conditions are shown in Figure. 3.16. For the gadolinium-treated group, we obtained average strain energies of E = 223 ± 30 fJ (before treatment) and E = 225 ± 31fJ (after treatment) [N=10]. For the streptomycin-treated group, we found E = 310 ± 41 fJ (before treatment), and E = 310 ± 38 fJ (after treatment) [N = 9]. Averaging the two groups together yielded E = 264 ± 26 fJ (before treatment), and E = 266 ± 26 fJ [N=19], as shown in Figure 3.16

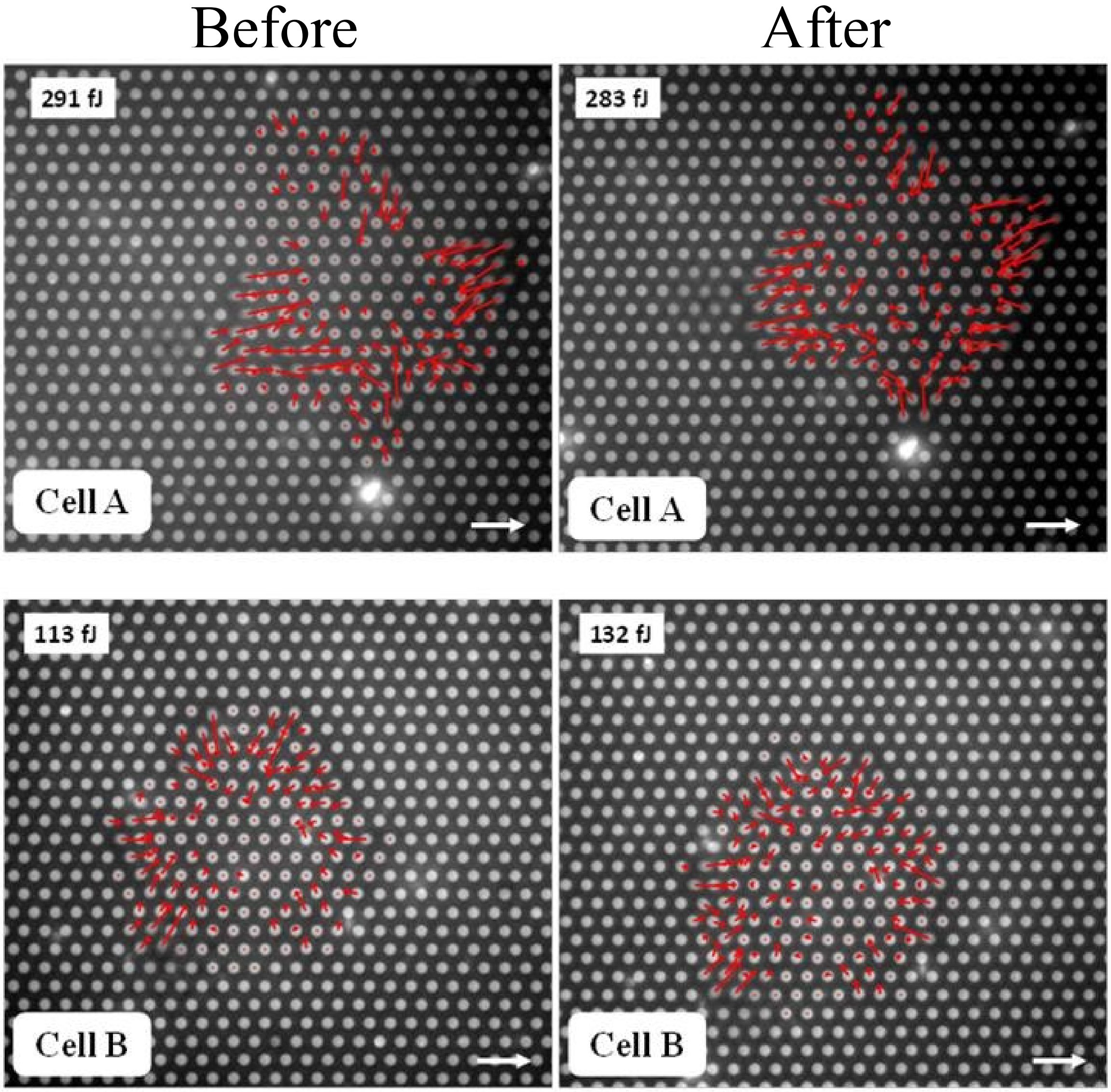

Figure 3.12: Force vector plots of CMFs before and after gadolinium treatment. No reduction in contractility was observed. Inset is whole cell strain energy. Scale vector is 10 nN.

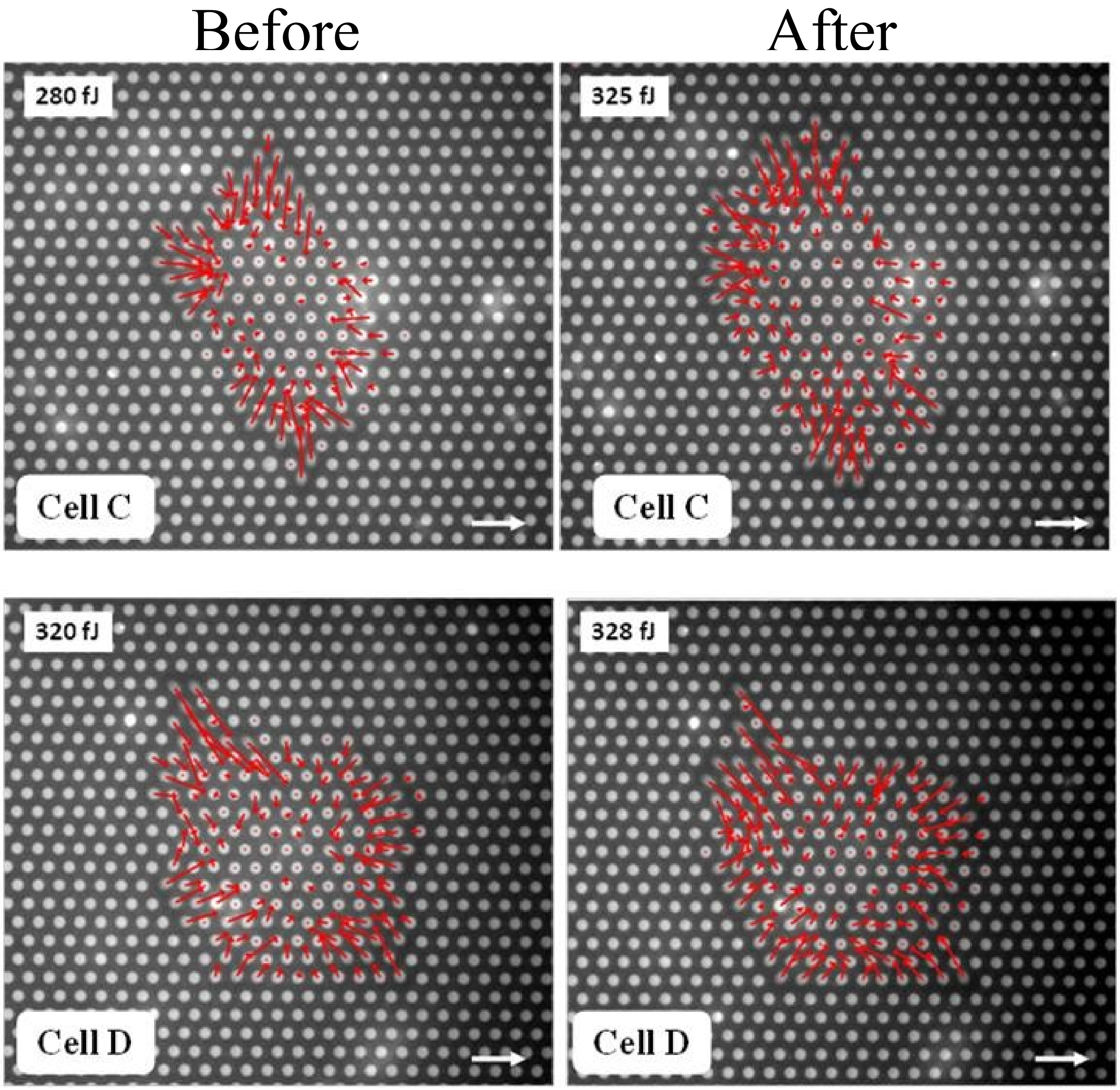

Figure 3.13: Force vector plots of CMFs before and after gadolinium treatment. No reduction in contractility was observed. Inset is whole cell strain energy. Scale vector is 10 nN.

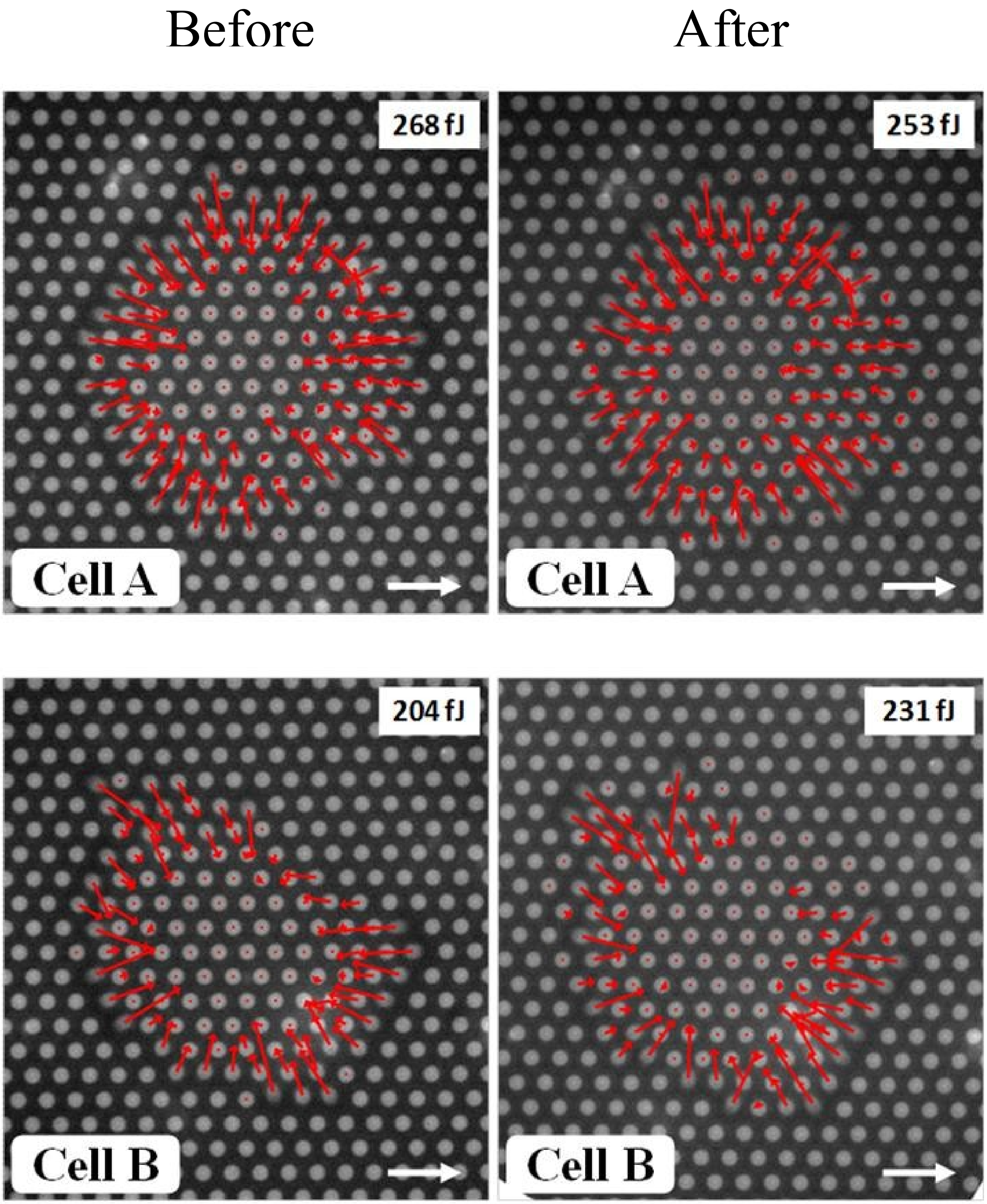

Figure 3.14: Force vector plots of CMFs before and after streptomycin treatment. No reduction in contractility was observed. Inset is whole cell strain energy. Scale vector is 10 nN.

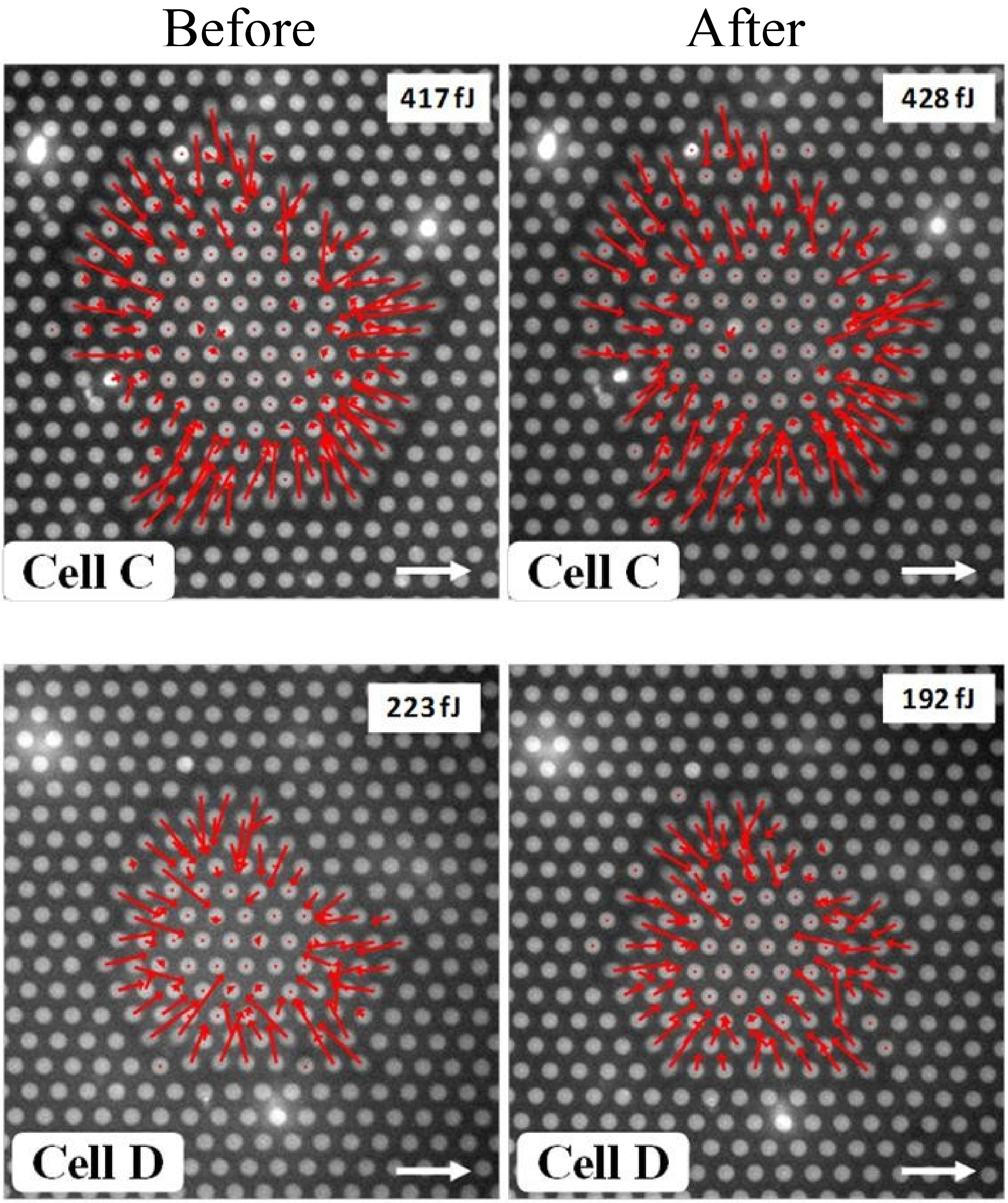

Figure 3.15: Force vector plots of CMFs before and after streptomycin treatment. No reduction in contractility was observed. Inset is whole cell strain energy. Scale vector is 10 nN.

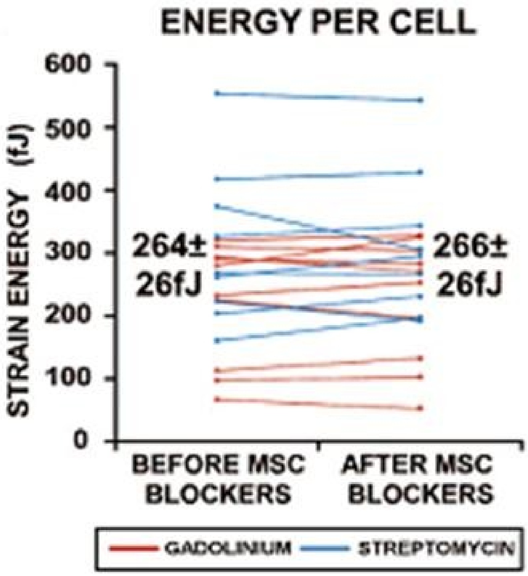

Figure 3.16: Comparison of CMF whole cell strain energy measured using mPADs. Treatment with gadolinium (red) or streptomycin (blue) had no significant affect on CMF contractility. (From [27])

3.3.4 Gap Junction Knockdowns

Gap junctions are specialized connections between adjacent cells that allow for the passage of various molecules and ions. The primary gap junction protein associated with electrical coupling in cardiac tissue is connexin 43 [31]. In order to clearly observe the contribution to conduction slowing from electrical cell-cell interactions between cardiac fibroblasts and cardiac myocytes, shRNA transduction was used to inhibit the cells' ability to produce connexin 43, a technique known as "silencing", in a population of CMFs prior to seeding on myocyte monolayers. The effects of shRNA transduction were controlled for by an identical treatment using scrambled shRNA, which had no effect on the cell's ability to express connexin 43. Experiments performed in the Tung lab showed that silencing connexin 43 expression did not suppress the conduction slowing observed in fibrotic tissues. These results suggest that electrical coupling is not the primary mechanism behind the conduction slowing we observed in model cardiac tissues [27].

The effect of connexin 43 silencing on CF contractility was measured using mPADs. As before, when measuring separate populations of CMFs, a large spread in cell strain energy was observed. Figures 3.17 and 3.18 show representative force vector maps spanning a wide range of energies for control and silenced CMFs, respectively. Figure 3.19 is a cumulative distribution of whole cell strain energies for each population. The trace overlap shows that the probability of finding a cell with any given value of strain energy is comparable for the two populations. Average strain energies for the two populations were not significantly different ($p = 0.5$):

$E = 251 \pm 25$ fJ (n=17)(connexin43 silenced), $E = 228 \pm 23$ fJ (n=20)(control).

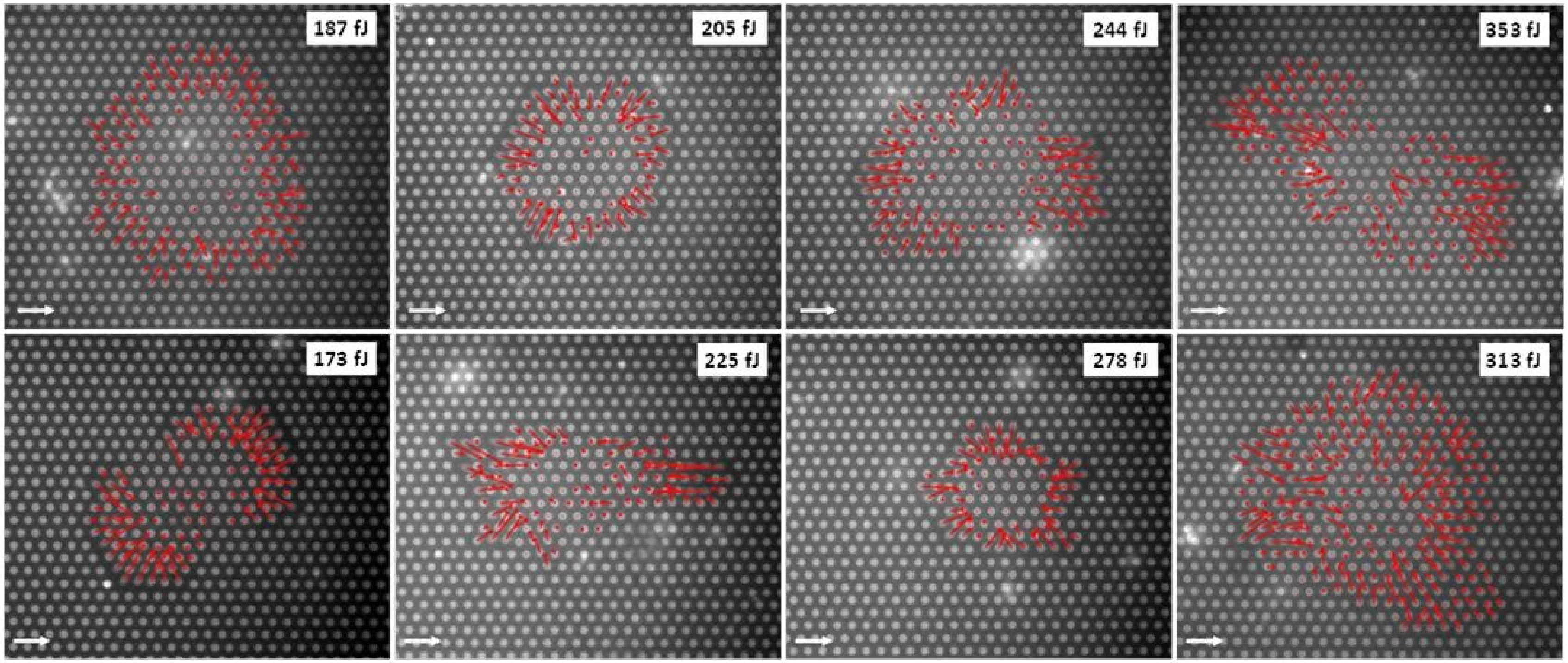

Figure 3.17: Top row: control cardiac myofibroblasts transfected with scrambled shRNA. Bottom row: Cardiac myofibroblasts transfected with shRNA to silence expression of connexin43. Multiple images show representative examples of the range of contractility observed. No significant difference in contractility was observed as a result of connein43 silencing. Control vector is 10 nN.

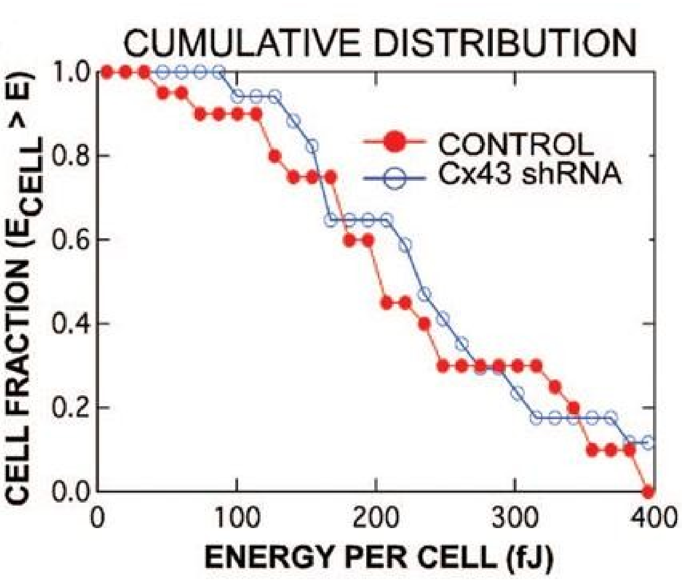

Figure 3.18: Cumulative distribution shows the probability (y-axis) that a cell in a given population will have a whole cell contractile energy greater than or equal to a selected value (x-axis). The lack of vertical separation between the control and connexin 43 shRNA traces shows no affect on contractility due to treatment. (From [27])

3.3.5 Adherens Junction Knockdowns

Mechanical linkages known as adherens junctions (Section 1.2.2) serve to mechanically link the cytoskeletons of adjacent cells. These junctions include transmembrane cadherin proteins, the external portion of which serves as binding points between cells. The internally exposed regions of cadherins are bound by other proteins (catenin, vinculin) to actin fibers that make up the cytoskeleton. Binding to actin allows adherens junctions to serve as points of force transfer between coupled cells [32, 33]. To investigate mechanical coupling via adherens junctions between cardiac myofibroblasts and myocytes, populations of CMF's were silenced for specific types of cadherins known to abundant in heart tissue [25, 34-36] in order to disrupt mechanical coupling.

Subsequent measurements of model tissue conduction velocity were combined with measurements of CMF contractility on mPADs to further characterize CMF myocyte mechanical coupling, and to determine the affects of cadherin silencing on CMF force generation. Figures 3.19 and 3.20 show force vector maps of representative cells from both control (top row) and silenced (bottom row) populations for OB-cadherin and N-cadherin knockdowns, respectively, illustrating the spread observed in the contractility of both cell populations. Silencing of both OB-cadherin and N-cadherin had no significant effect on CMF contractility compared to control cells (Figure 3.21). However, while silencing of OB-cadherin had no significant effect on model tissue conduction velocity (Figure 3.22), silencing of N-cadherin served to restore conduction velocity to normal levels (Figure 3.22).

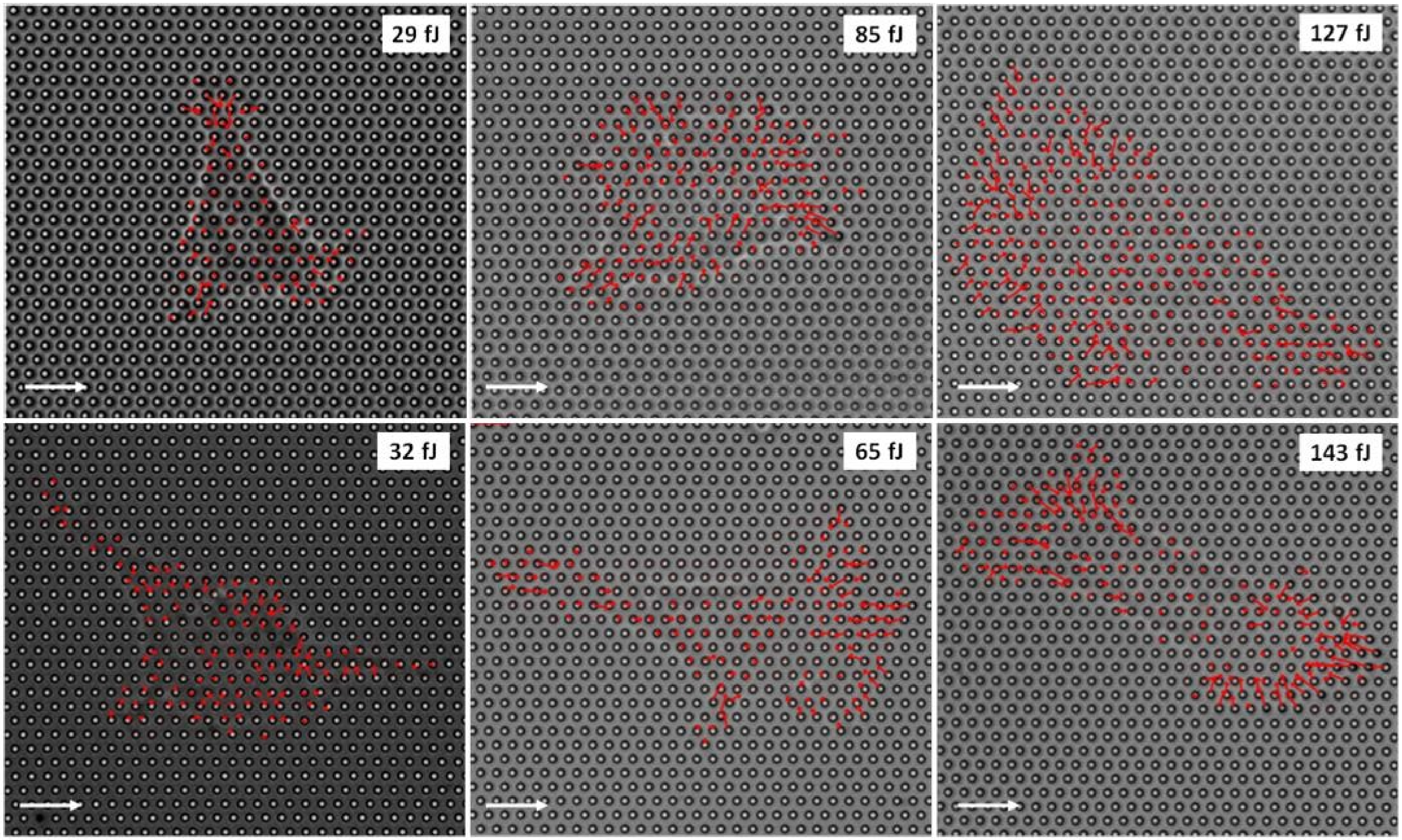

Figure 3.19: Top row: Control cardiac myofibroblasts transfected with scrambled shRNA. Bottom row: Cardiac myofibroblasts transfected with shRNA to silence expression of OB-Cadherin. Multiple images show representative examples of the range of contractility observed. No significant difference in contractility was observed as a result of OB-Cadherin silencing. Control vector is 10 10 nN.

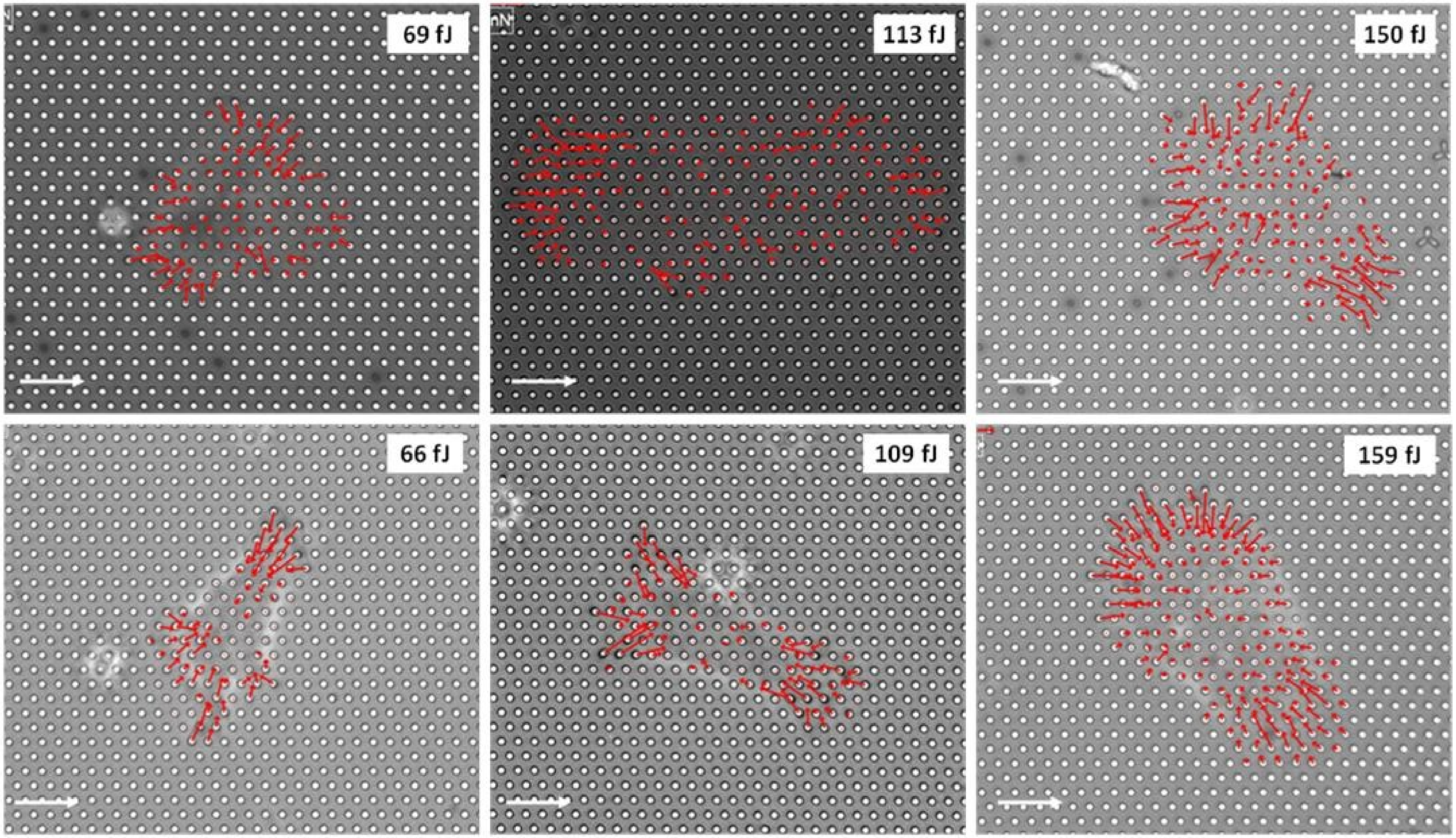

Figure 3.20: Top row: Control cardiac myofibroblasts transfected with scrambled shRNA. Bottom row: Cardiac myofibroblasts transfected with shRNA to silence expression of N-Cadherin. Multiple images show representative examples of the range of contractility observed as a result of N-Cadherin silencing. Control vector is 10 nN.

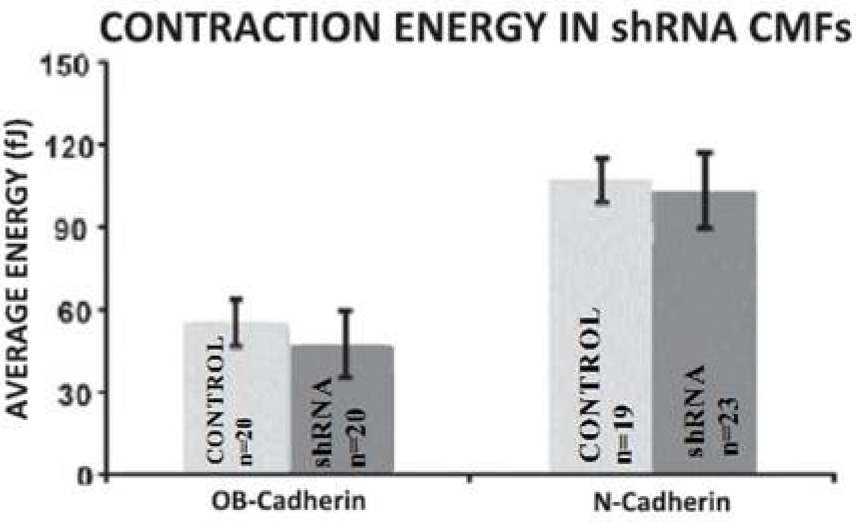

Figure 3.21: Experiments using mPADs show no affect on CMF contractility due to silencing of either OB-Cadherin or N-Cadherin. (From [28])

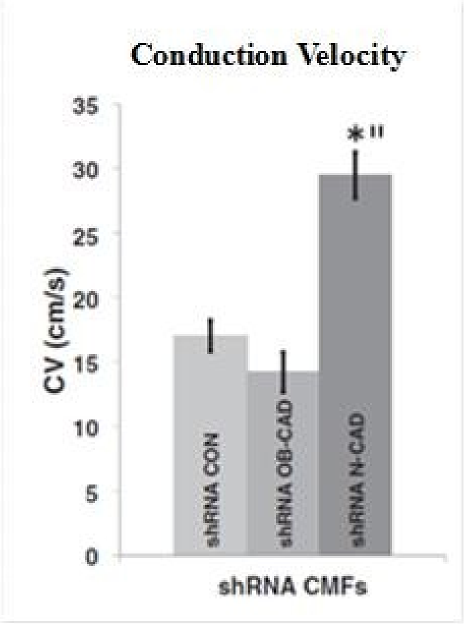

Figure 3.22: Conduction velocity experiments found no affect on conduction slowing due to OB-Cadherin silencing, but significant restoration of conduction velocity due to N-Cadherin silencing. (From [28]) (Data courtesy of Susan Thompson.)

3.3.5 Modulation of RhoA activity

RhoA is a small GTPase protein known to regulate acto-myosin force generation (Section 1.1.2) through activation of ROCK, which in turn phosphorylates, or activates, myosin light chain (MLC) and MLC phosphatase, both of which contribute to contractility [2]. Micropost arrays were used to measure the contractile output of CMFs treated by viral intervention to express dominant negative (N19) and constitutively active (V14) forms of RhoA. The same cell populations were used for supplementation on model cardiac tissues to determine the effects of altered CMF contraction on conduction velocity. Figure 3.23 shows representative force vector maps for N19-expressing (top row) and V14-expressing (bottom row) CMFs. Measurements using mPADs found a significant difference in contraction between the two treatments: $E = 126 \pm 20$ fJ, ($n = 15$)(N19) and $E = 247 \pm 28$ fJ, ($n = 15$)(V14) (Figure 3.24). While supplementation of V14-expressing CMFs onto model cardiac tissues resulted in conduction slowing levels similar to CMFs expressing GFP and wild type RhoA (Figure 3.25 B), reduced conduction slowing was observed for tissues supplemented with N19-expressing CMFs (Figure 3.25 A).

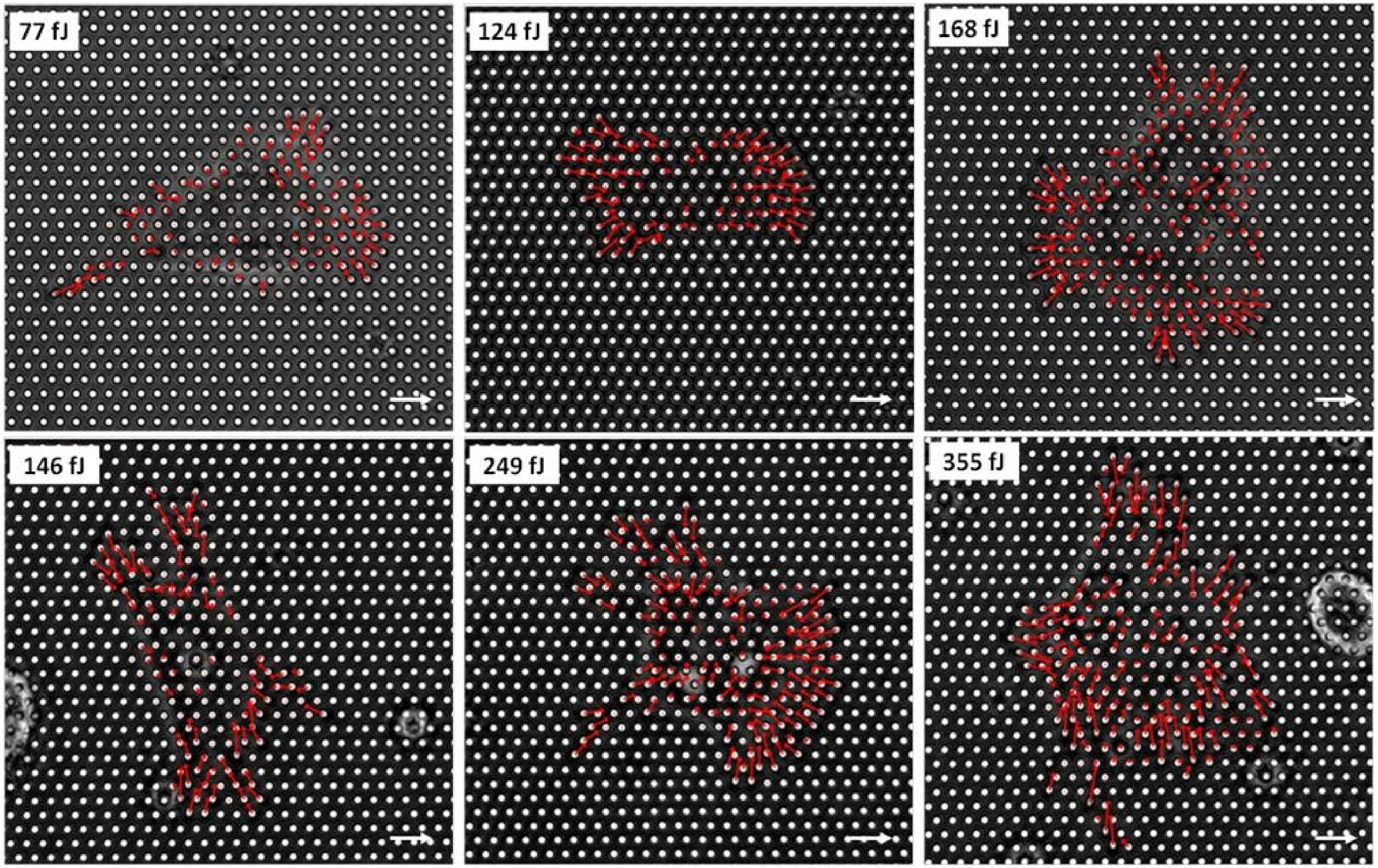

Figure 3.23: Top row: Cardiac myofibroblasts genetically modified to express dominant negative RhoA. Bottom Row: Cardiac myofibroblasts genetically modified to express constitutively active RhoA. RhoA modulation is reflected by changes in cellular contractility. Representative images show the range in observed contractility. Scale vector is 10 nN.

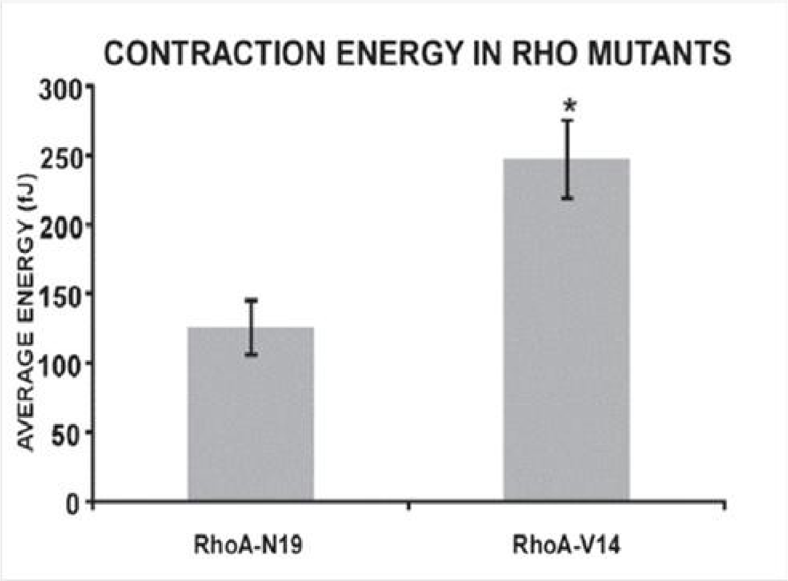

Figure 3.24: Experiments on mPADs found a significant increase in CMF force generation as a result of Rho-V14 expression, and a significant decrease due to expression of Rho-N19. (From [28])

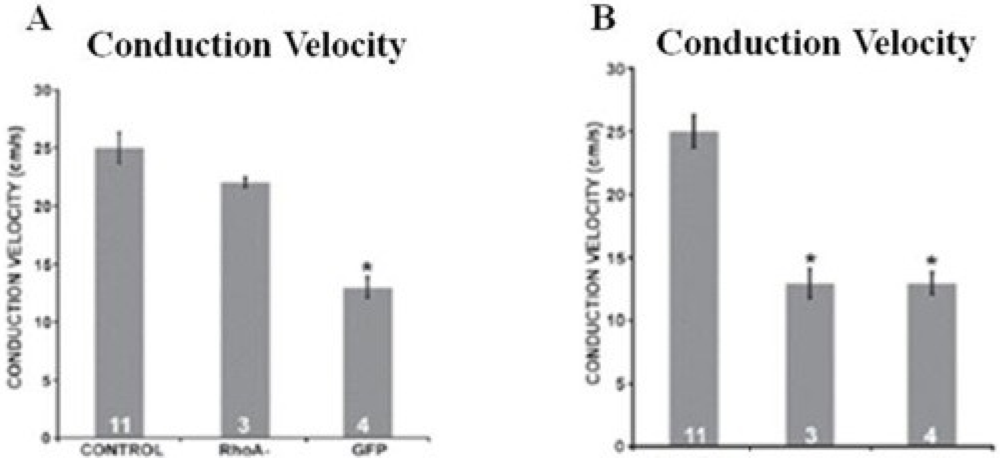

Figure 3.25: Results of conduction velocity experiments show significantly restored CV due to expression of dominant negative Rho-N19 (A). Rho-V14 expressing CMFs do not further reduce CV compared to control CMFs (B). (From [28]) (Data courtesy of Susan Thompson.)

3.3.5 Y-27632

Y-27632 is a drug that selectively inhibits p160ROCK, a protein known to regulate focal adhesion and stress fiber assembly, as well as force generation, through phosphorylation of myosin light chain (MLC). Micropost arrays were used to measure the affect of Y-27632 treatment on cardiac myofibroblast contractility. Single CMFs adhered to mPADs were imaged before and after treatment with 50μM Y-27632 (Sigma) for 30 minutes (Figures 3.26, 3.27).

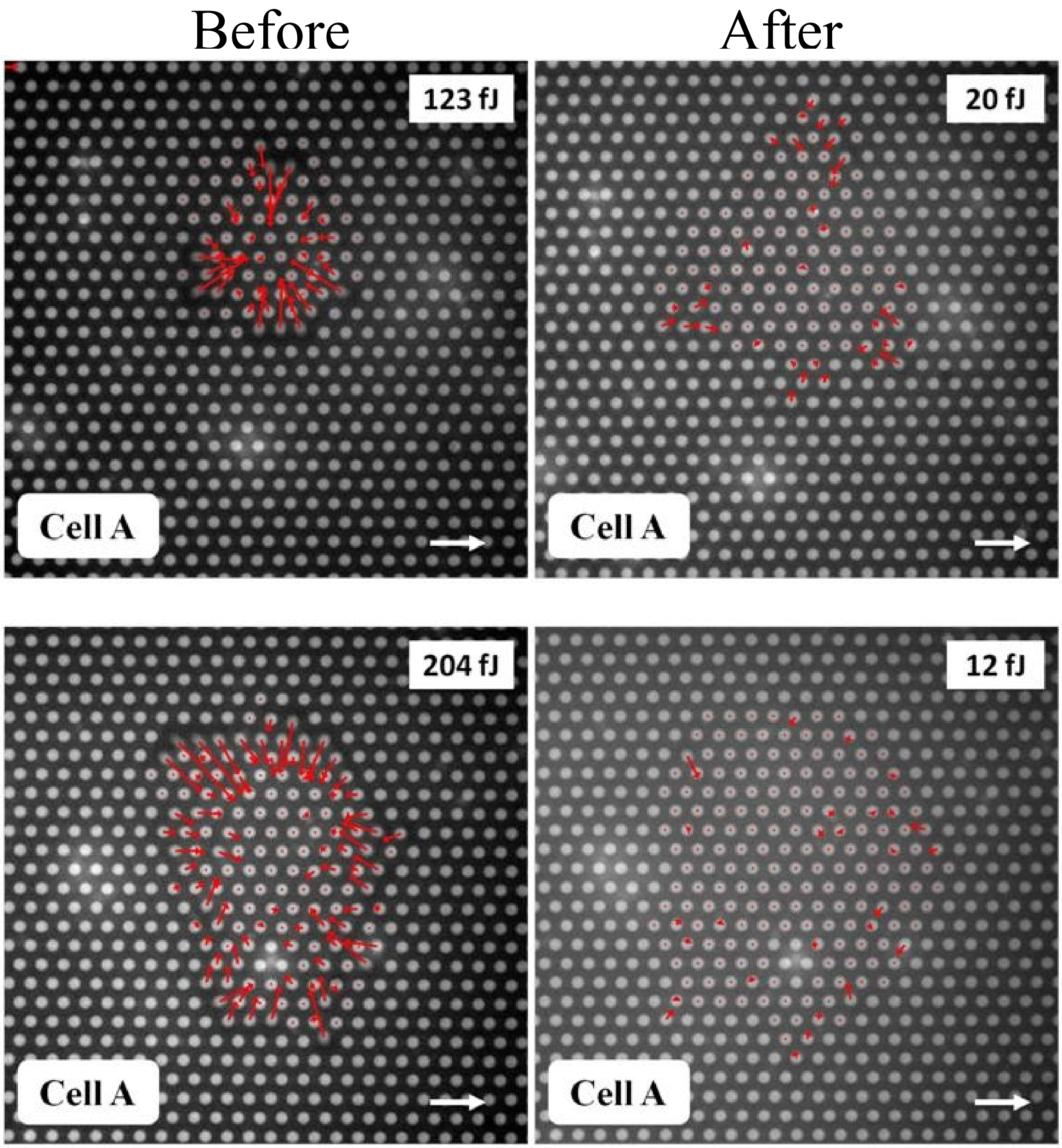

Figure 3.26: Force vector plots of CMFs before and after Y-27632 treatment. Inset is whole cell strain energy. Scale vector is 10 nN.

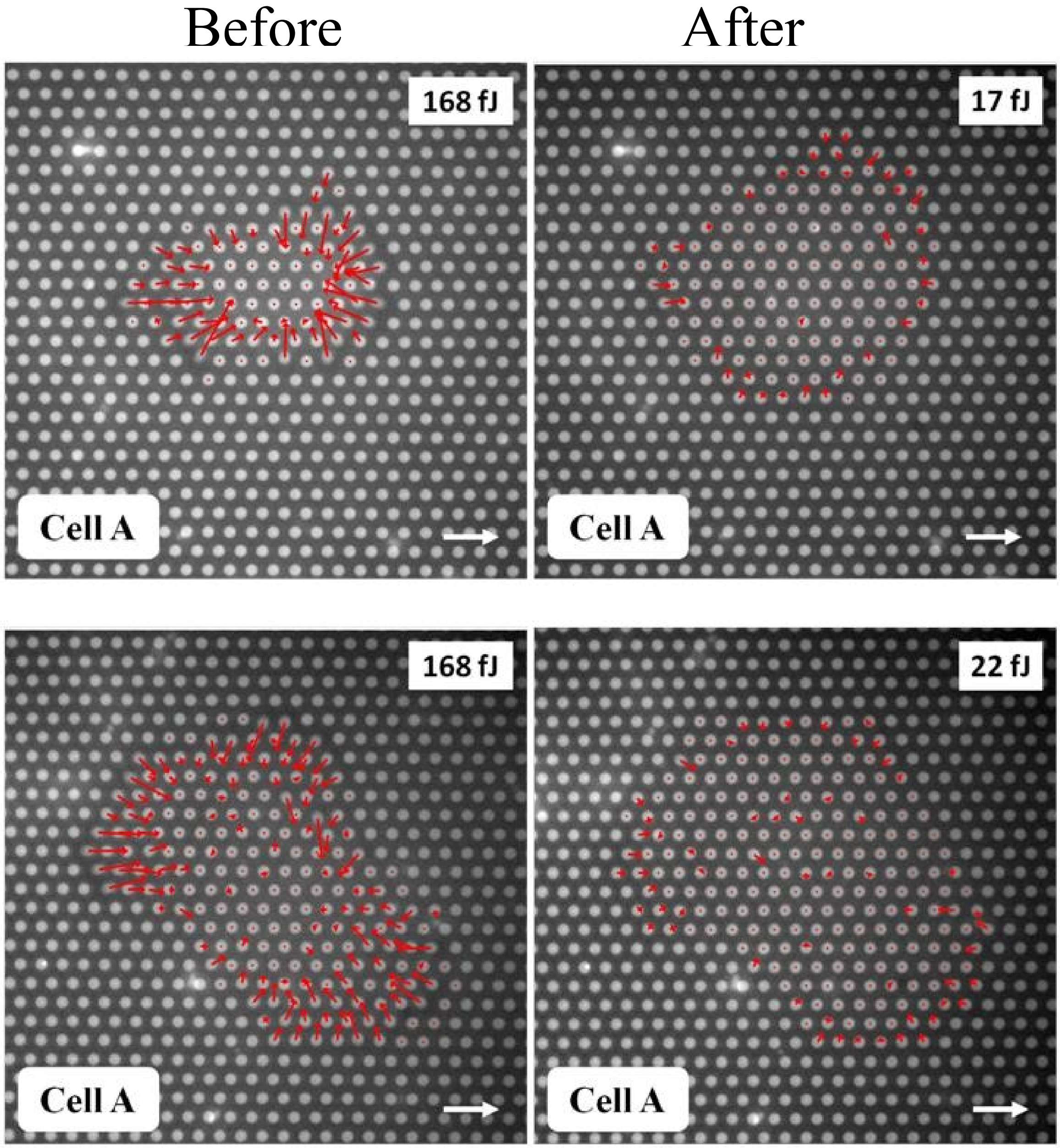

Figure 3.27: Force vector plots of CMFs before and after Y-27632 treatment. Inset is whole cell strain energy. Scale vector is 10 nN.

Treatment resulted in a dramatic decrease in average total cell strain energy: E = 226 ± 30 fJ (before), E = 15 ± 3 fJ (after), n=9 (Figure 3.28).

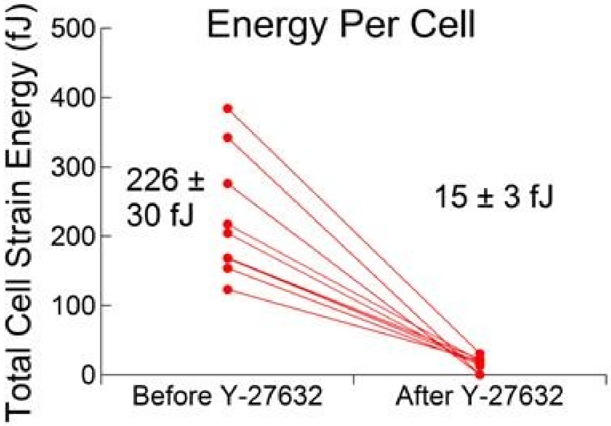

Figure 3.28: Change in total cell strain energy for n = 9 CMFs as a result of treatment with Y-27632.

3.3.6 Cardiac Myofibroblast Force Generation During Cell Spreading

Observation of CMFs immediately following seeding onto micropost arrays allowed for measurement of contractile force dynamics during the spreading process. These measurements investigated the role of CMF contractility in conduction velocity slowing of model tissues that was observed within 30 minutes of supplementation with CMFs. For 12 cells observed, the onset of visible micropost deflection occurred after an average of 32 minutes following seeding onto mPADs. Cells generally showed low magnitude forces when actively increasing their area (Figure 3.29 A-D), followed by rapid initiation of force generation when approaching maximum area (Figure 3.29 E). Forces continued to increase after stabilization of cell area (Figure 3.29 F-H). Figures

3.30 and 3.31 show force vector maps for two different CMFs at elected time points beginning 10-15 minutes after CMF seeding on an mPADs, as well as the evolution of total cell strain energy and cell area over time. Experiments on model cardiac tissues were also performed immediately following CMF supplementation and the effects on conduction velocity were measured, finding that the onset of conduction slowing could occur as early as 20 minutes, consistent with the time course of CMF force generation observed on mPADs. Taken together, these results further demonstrate the effects of CMF force generation on model cardiac tissue function.

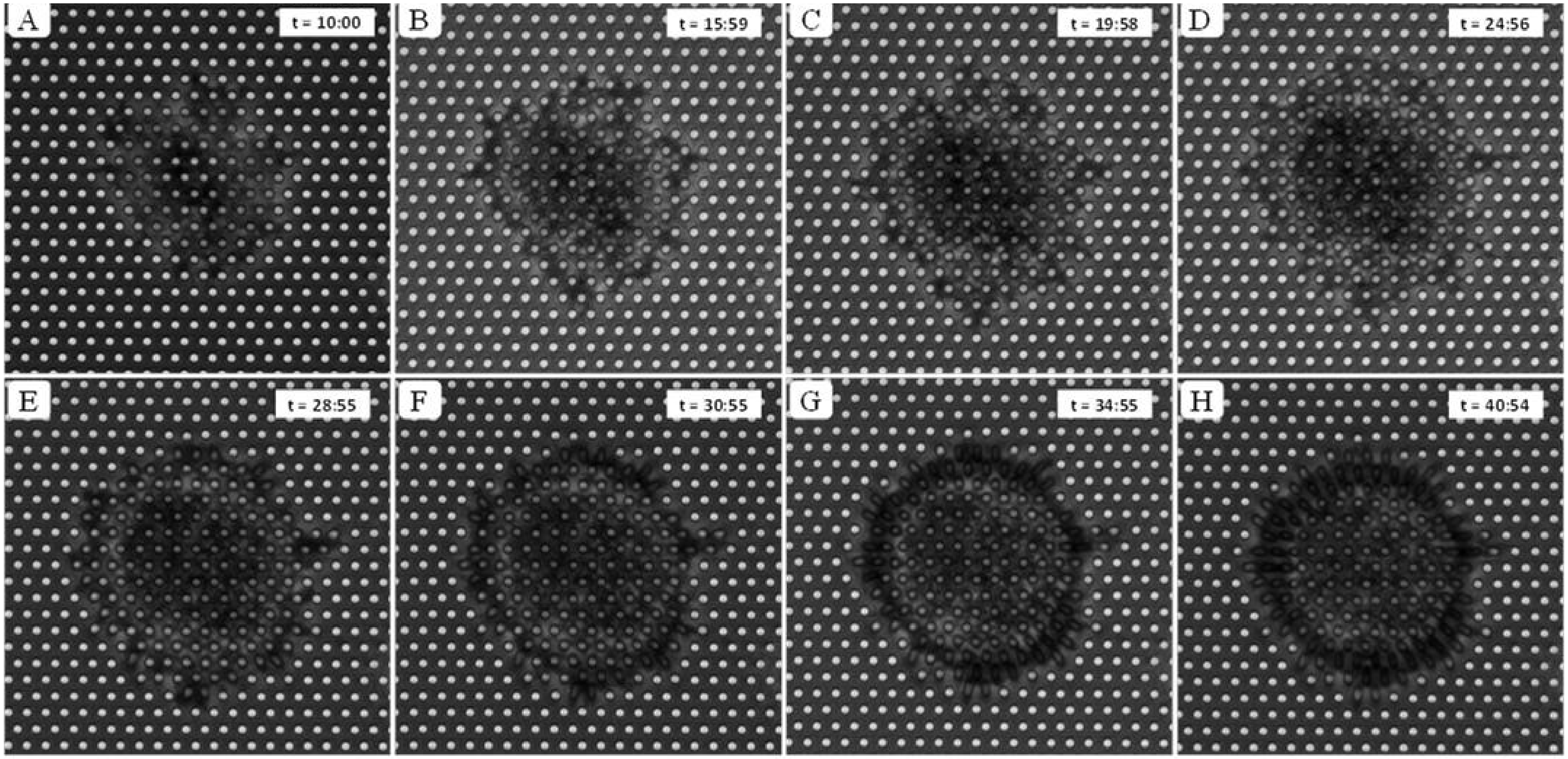

Figure 3.29: Phase contrast images of a cardiac myofibroblast adhering and spreading on a micropost array. Microposts become visibly deflected at 28 minutes as cellular traction forces are established. Phase contrast imaging allows for qualitative observation but may be unsuitable for quantitative force field analysis.

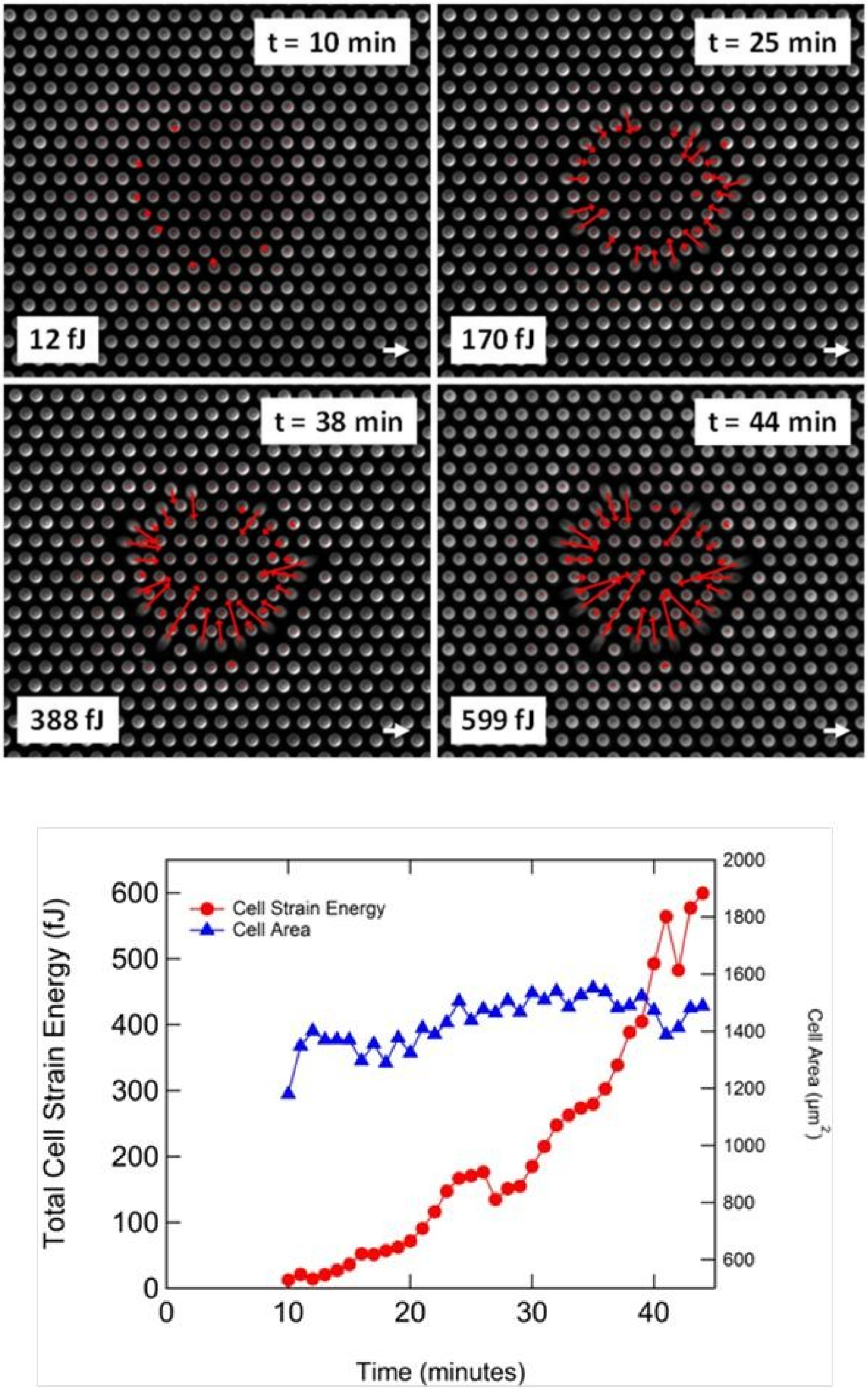

Figure 3.30: Top: Force vector maps of a CMF shortly after seeding on an mPAD. Insets show time since seeding and whole cell strain energy. Scale vector is 10 nN. Bottom: Plot of cell area and total strain energy versus time. (From [28])

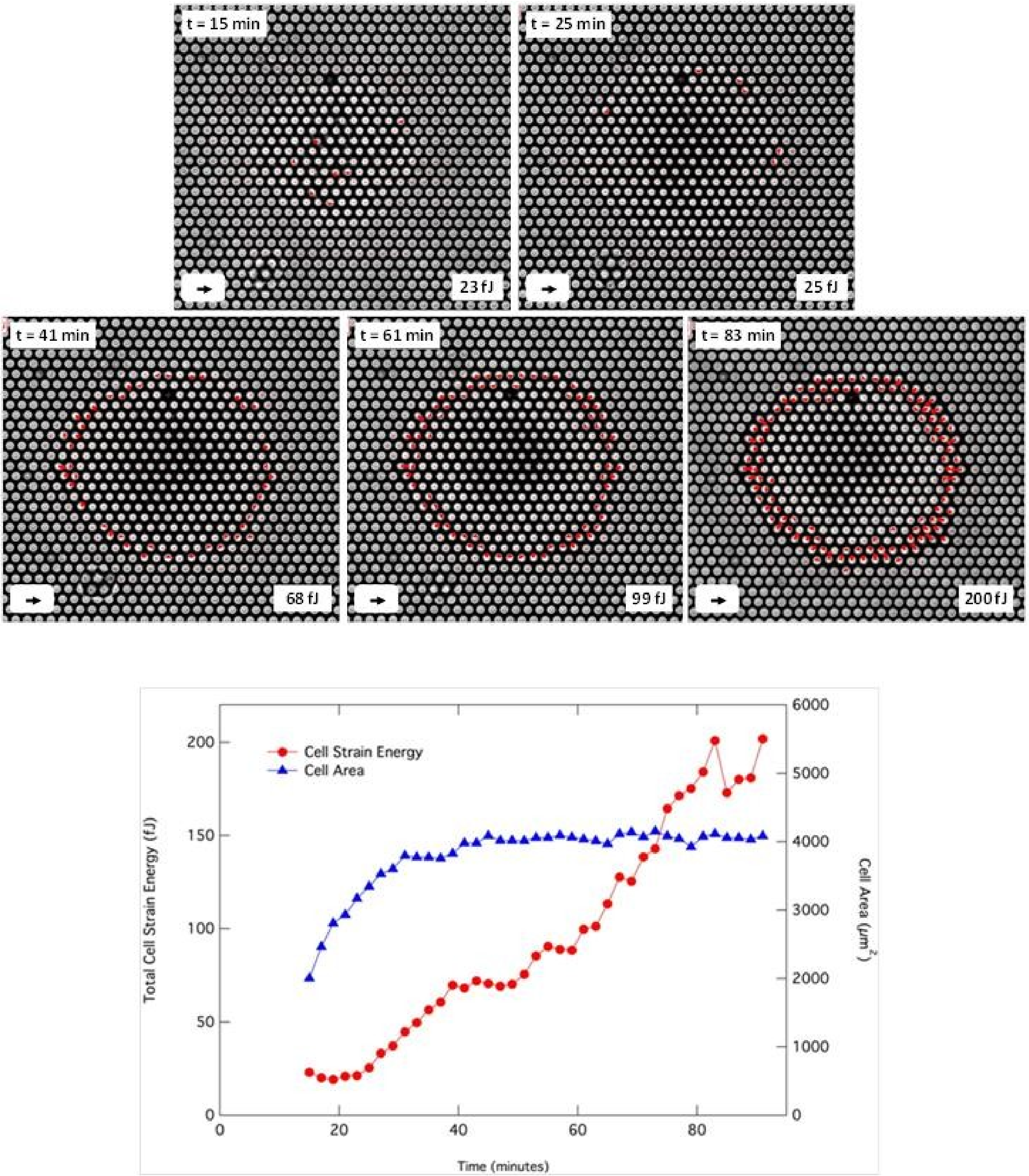

Figure 3.31: Top: Force vector maps of a CMF shortly after seeding on an mPAD. Insets show time since seeding and whole cell strain energy. Scale vector is 10 nN. Bottom: Plot of cell area and strain energy vs. time.

3.6 Discussion

This work has provided, for the first time, characterization of neonatal rat ventricular fibroblast contractility using mPADs. Basal contractile capabilities, as determined by the total bending energy imparted to a flexible micropost substrate by a single CF, were measured for a large number of cells from multiple cultures. These measurements provided a direct quantitative measure of CF contractile output. Changes in fibroblast contractility were measured in response to a multitude of treatments chosen to elucidate the nature and effects of mechanical heterocellular coupling between CFs and neonatal rat ventricular myocytes (NRVMs). Experiments measuring the velocity of electrical signal propagation, or conduction velocity (CV), in model cardiac tissues consisting of patterned monolayers of cardiac myocytes revealed significant CV slowing when the monolayers were supplemented with CFs. CV slowing was exacerbated when the monolayers were supplemented with CMFs, a more contractile CF phenotype brought on by treatment with transforming growth factor beta (TGF-β). These changes were hypothesized to be a result of mechanical coupling between the myocytes and the CFs/CMFs, through which CF/CMF contractile forces act on and open stretch activated ion channels located within the myocyte membrane. CF and CMF contraction were measured using mPADs, showing CMFs to be capable of generating significantly increased contractile forces compared to CFs. These results were consistent with previous studies by Lijnen *et al.* that utilized gel contraction assays [37]. Further experiments were performed in order to modulate CMF contraction and observe the resulting affect on CV in CMF supplemented myocyte monolayers. CMF treatment with the acto-myosin inhibitor blebbistatin was found to significantly decrease CMF contractility. Treatment of CMFs with blebbistatin prior to seeding on myocytes monolayers was shown to reverse the conduction slowing effects previously observed as a result of CMF supplementation, highlighting the importance of CMF contractility in the observed CV slowing resulting from interactions between these two cell types. Further regulation of CMF contractility was achieved through genetic modification to modulate RhoA activity via expression of either constitutively active Rho-V14, which resulted in increased CMF contractile force generation, or expression of dominant negative Rho-N19, which resulted in a significant decrease in CMF contractile force generation. When the genetically modified CMFs were used for supplementation onto myocyte monolayers, monolayers containing the less contractile Rho-N19 expressing CMFs were found to have improved CV as compared to those with unmodified CMFs, and the more contractile Rho-V14 expressing CMFs did not further reduce CV as compared to monolayers supplemented with unmodified CMFs. These results demonstrated that CV slowing in model cardiac tissues as a result of the action of CMF contractile force generation is likely saturated by the levels of force generated by unmodified CMFs, and is not bolstered by further increases in CMF contractility. However, CV could be significantly reduced by reducing CMF contractility. Furthermore, it was observed that the onset of CV slowing in CMF supplemented myocyte monolayers could occur as early as 30 minutes following CMF supplementation, and measurement of CMF contractile force dynamics during cell spreading found that the onset of significant traction, on average, also occurred at ~30 minutes. Contractile forces continued to increase after stabilization of cell area, similar to observations made by Thaler et al using mouse embryonic fibroblasts [38]. The above experiments demonstrate the significance of CMF contractility in driving CV slowing in model cardiac tissue.

To investigate mechanisms through which CMF force generation could be affecting myocyte function, chemical and genetic treatments that did not interfere with CMF contractility were performed. Treatment with the mechanosensistive channel (MSC) blockers gadolinium and streptomycin had no significant affect on CMF contractility, yet CV was significantly restored in CMF supplemented myocyte monolayers treated with either gadolinium or streptomycin. These results make clear that a significant element of the coupling responsible for CV slowing is the activation of MSCs resident in the myocyte membranes. The role of cell-cell adhesions was directly explored using genetic “silencing” techniques used to inhibit the cells’ ability to express junctional proteins associated with both electrical and mechanical cell-cell coupling. Inhibiting expression of the gap junction protein connexin 43 in CMFs had no significant effect on either CV in monolayer experiments, or CMF contractility, demonstrating that electrical coupling via connexin 43 is not responsible for the observed effects. In contrast, while inhibited expression of two cadherin proteins associated with mechanical cell-cell coupling (N-cadherin, OB-cadherin) was found to have no significant affect on CMF force generation, silencing of N-cadherin served to alleviate the CV slowing effects in CMF supplemented monolayers. These results define mechanical coupling via N-cadherin as an important element contributing to CMF-myocyte coupling.

Taken together, the results of CV experiments performed in the Tung lab using CMF supplemented model cardiac tissues, combined with the direct measurements of CMF contractile forces using mPADs described here, have identified a potential mechanism by which injury-induced transformation of CFs into highly contractile CMFs may contribute to arrhythmogenic behavior in cardiac tissue.

Chapter 4 Cellular Traction Force Response to Global Stretch

4.1 Introduction

The following experiments utilized a modified version of the micropost array detector (mPAD) that allowed for real time measurement of cell generated traction forces in response to global stretch stimulation. Cellular response to short duration 5s stretches was quantified through changes in whole cell strain energy imparted to the mPAD substrate following transient stretch. Longer stretches ~ 4 minutes in duration were applied and the cellular response was measured *during* the application of stretch.

The arterial smooth muscle cells and surrounding extra cellular matrix that comprise the inner walls of blood vessels are routinely exposed to external global stretching forces caused by changes in blood pressure. In order to establish a more complete understanding of blood vessel physiology, it is therefore necessary to understand how the cells and tissue that form blood vessels respond and adapt in such a mechanically dynamic environment. To this end, I have developed an experimental procedure using the mPAD device described previously, which enabled the measurement of cell generated traction force dynamics during an applied stretch.

4.2 Experimental Techniques

4.2.2 Transient 5s Stretch

Biaxial strains in the range up to 20% were applied with the custom-built vacuum-controlled stretching device described in Section 2.2.3. Prior to application of stretch, single cells were imaged using a 40x or a 60x microscope objective in order to establish their baseline contractile forces. Following baseline imaging, cells were observed using a 10x objective to ensure an accurate visual account of cell morphology and location in order to re-locate the cell following transient stretch. Stretch was applied by manual syringe pump operation to bring the system to the vacuum pressure corresponding to the desired level of stretch. Once maximum vacuum was reached, the stretch direction was reversed, bringing the system back to 0 psi. For stretches of 7%-10% strain, a maximum vacuum of -3.0 psi was used, and for stretches of 15-20% strain, a maximum vacuum of -4.0 psi was used. Manual syringe pump operation resulted in transient stretches of approximately 5s duration. Once stretch was completed, the cell of interest was re-located using the 10x objective. Cell positions did not change substantially following stretch. Once the substrate reached static equilibrium, observation using a 40x or a 60x objective resumed. Following stretch, cells were imaged for 5 minutes, with a minimum of 15 minutes in between stretches applied to the same substrate. The time period between stretches was chosen in order to allow all cells adhered to the substrate to reach a new quasi-static equilibrium state prior to being exposed to continued stretch application, consistent with recovery periods observed in human airway smooth muscle cells [39], and human bladder smooth muscle cells [40].

4.2.3 Observation During Stretch Application

In order to observe dynamics of cellular traction forces during an applied stretch, images were taken while the substrate strain was actively changing, as opposed to before and after stretch application. In this mode, observation using a 40x or a 60x objective, as needed to measure the microposts' deflections with sufficient accuracy, required constant input from the user. As the cells being observed were in general not in the center of the substrate, they translated in the x-y plane as the substrate stretched, requiring monitoring and adjustment of the stage position at all times in order to keep the cell of interest within view of the camera. Along with changes in x-y position, imposition of substrate strain also caused changes in z positioning as the tension on the substrate membrane increased, requiring constant focus adjustment during the experiment. These requirements were met by using two output ports on the microscope simultaneously; one port directing light to the camera for imaging, and another port directing light to the microscope eyepiece for real time observation. While observing the sample through the eyepiece, the user could use one hand to maintain stage position while using the other hand to maintain focus on the cell. Manageable strain rates in the range $4.4\text{x}10^{-4}$ s^{-1} to $17\text{x}10^{-4}$ s^{-1} for these experiments were achieved using a 60 ml syringe with the syringe pump set at 420 μl/min and the syringe diameter setting equal to 14.43 mm. These strain rates resulted in transient stretches of approximately 4 minute duration.

4.2.4 Analysis

The inherent difficulties associated with micron scale imaging of a substrate in constant motion made the analysis for these experiments more challenging than the analysis performed on static substrates. Data sets for time lapse evolution of cellular traction forces typically consist of a stack of many images that can be analyzed sequentially with minimal initial input from the user. This was not possible for experiments where observation took place during an applied stretch. First, the subset of posts surrounding and including the cell must be present in every image in order to maintain a consistent region of interest where every post is uniquely identified and tracked. Due to the large amount of lateral movement during applied stretch, on the order of 100's of microns, as well as increasing strain causing fewer posts to be visible in later images, it was impossible to ensure that the same subset of posts would be present in every image. Because of this, each image had to be analyzed separately using a unique ROI, greatly increasing the required user input. Second, substrate movement in the z-direction caused many of the acquired images to be out of focus. In order to obtain analyzable data from these experiments, images that were properly focused had to be selected from the stack. Care was taken to select a sufficient number and temporal spacing of images in order to have data that adequately displayed the cell's response throughout the stretch. Once images were selected, each one underwent pre-processing as described previously in section 2.3.1, followed by individual analysis. Data from each individual analysis was then compiled from all analyzed images of a given cell, creating a complete picture of cellular traction force dynamics during applied stretch.

4.3 Results

4.3.1 Transient 5s Stretch

As described previously (Section 2.3.2), for a whole-cell scalar measure of traction forces and cellular contractility, the strain energy stored in each micropost as a result of forces imparted by the cell was summed for every post to which the cell was adhered: $E = \sum_i \frac{1}{2} k x_i^2$. Following application of transient stretch, BPASMCs exhibit a dramatic decrease in traction forces (Figure 4.1 A, C). Measures of whole cell strain energy imparted to the mPAD substrate revealed an average decrease of 49.77% (n=13) following application of a 7-10% magnitude stretch lasting approximately 5 seconds. Following stretch, cellular traction forces begin to recover in magnitude over the course of minutes (Figure 4.1 A, D). New quasi-equilibrium whole cell strain energy values were generally near levels observed prior to stretch application (Figure 4.1 A), with some cells reaching new equilibrium states below (Figure 4.2 A) or above (Figure 4.2 B) their pre-stretch values.

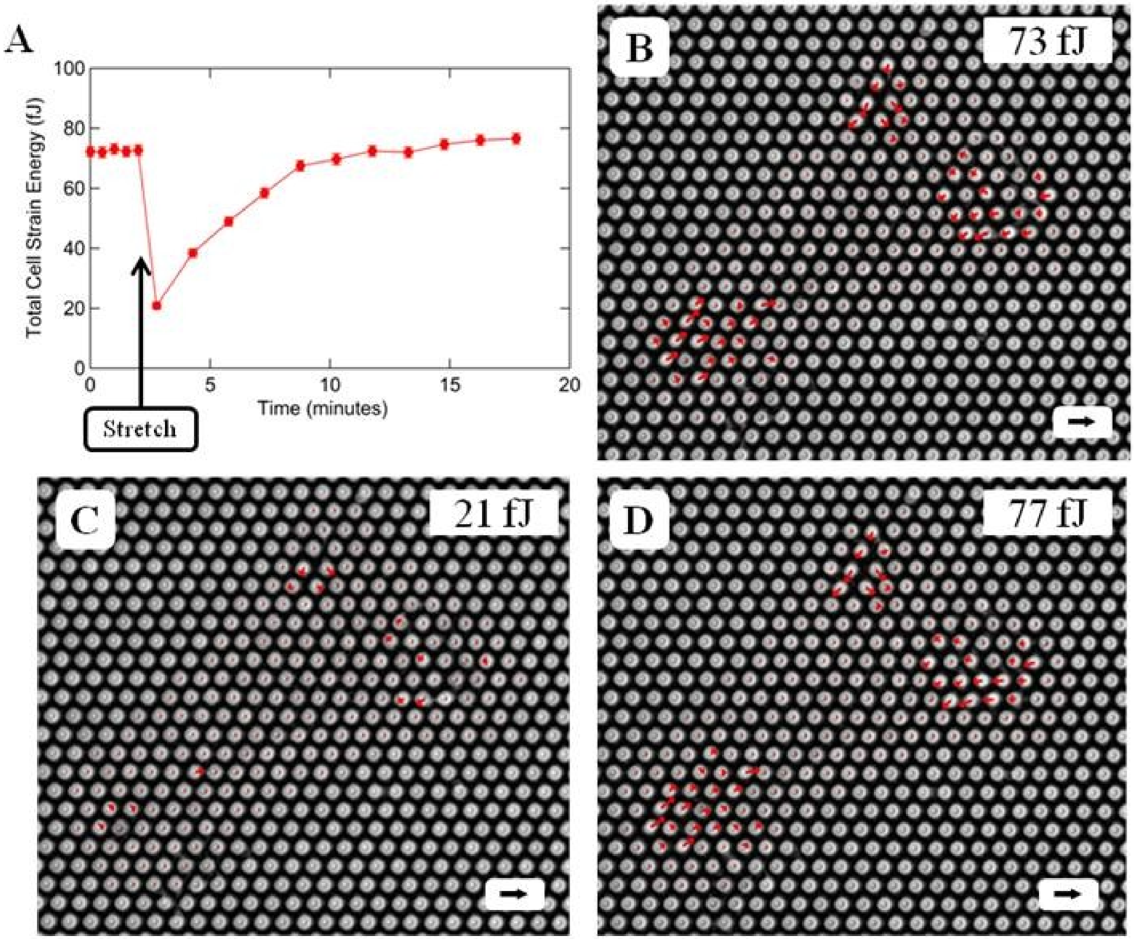

Figure 4.1: (A) Whole cell strain energy vs. time for a BPASMC exposed to a transient 8% stretch of 5s duration. Vector maps of cellular traction forces prior to stretch application. (B), immediately following stretch (C), and 14 minutes after stimulation. Scale vector is 10 nN.

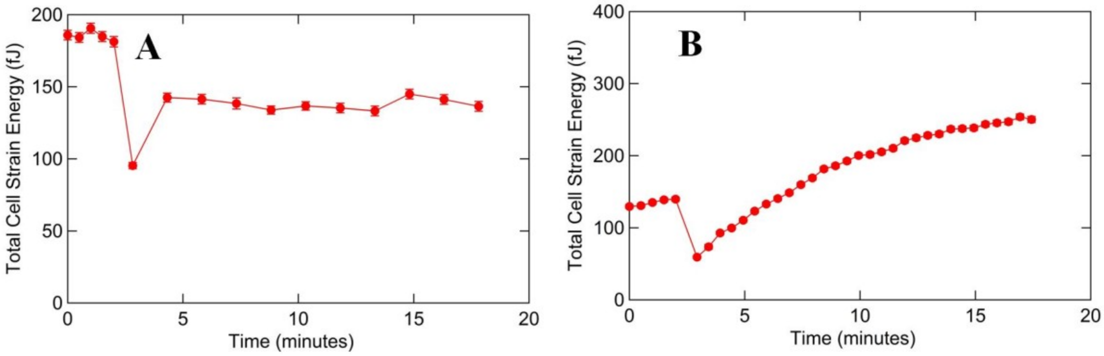

Figure 4.2: Whole cell strain energy vs. time for a BPASMC exposed to a transient 8% stretch of 5s duration. Variation in quasi-static equilibrium following recovery after stretch included cells that recovered to energy values less than (A), and greater than (B) baseline energy values.

4.3.2 Observation During Stretch

Using the aforementioned acquisition methods, traction force dynamics for BPASMCs were observed *during* application of a much slower transient stretch. These measurements provided a direct real time measurement of cellular behavior as substrate strain was actively changing. Figure 4.3A shows a schematic representation of substrate strain versus time for these experiments. Force vector maps corresponding to the red dots on the schematic show the contractile response of a BPASMC exposed to this stretch protocol. At maximum strain (Figure 4.3 C), traction force magnitudes are dramatically increased relative to pre-stretch (Figure 4.3 B). Traction forces decrease significantly upon reversal of substrate strain direction (Figure 4.3 D), and continue to decrease until stretch cessation (Figure 4.3 E). Worth noting, cell strain was indistinguishable from substrate strain, indicating that the cells were generally less stiff than the microposts and did not significantly resist stretching.

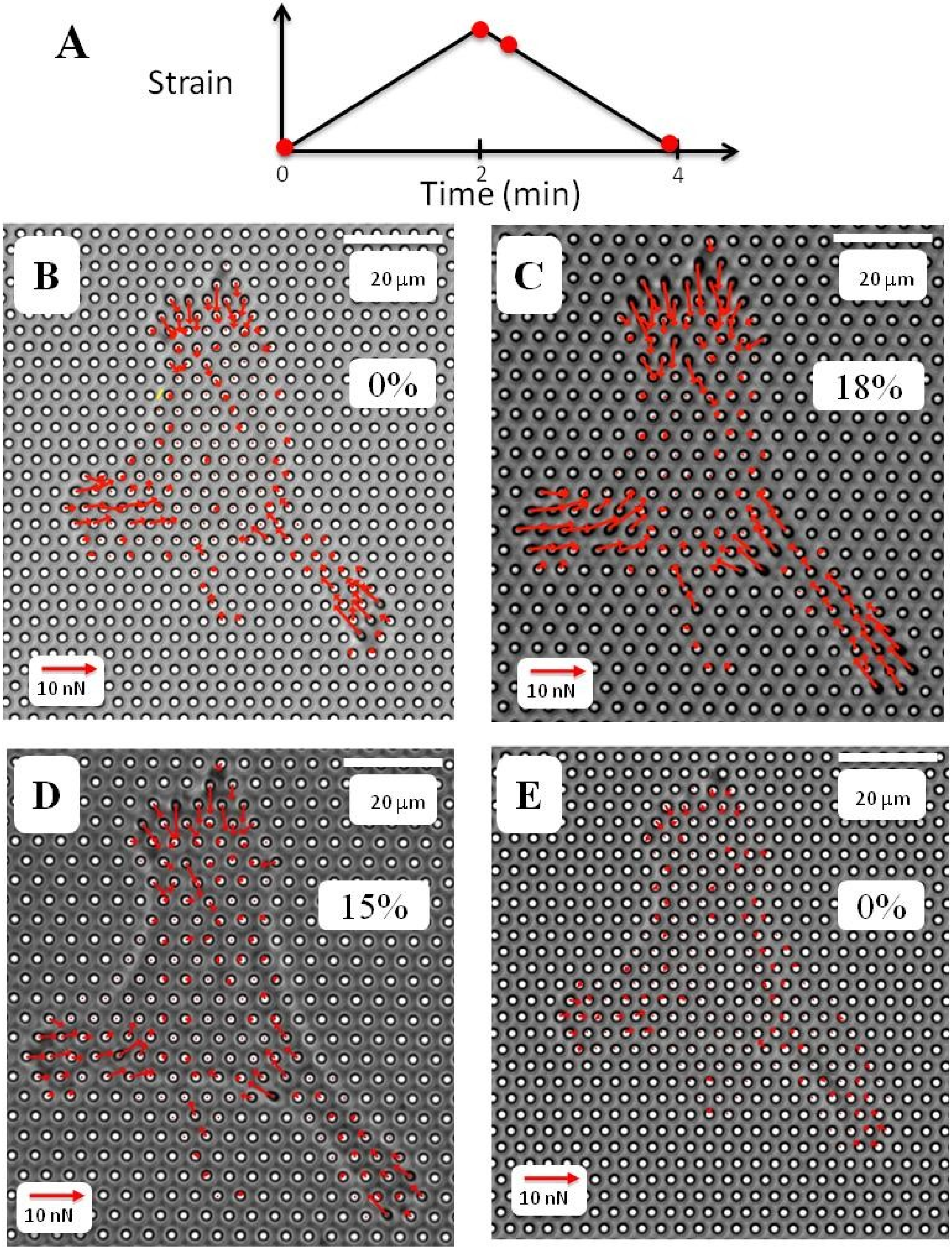

Figure 4.3: Schematic time course of applied strain for observation of traction force dynamic during stretch (A). Representative force vector maps show traction forces prior to stretch onset (B), at maximum strain (C), shortly after reversal of strain direction (D), and after stretch completion (E).

Whole cell strain energy was measured in response to applied stretch for multiple cells over a range of maximum strain values (Figures 4.4, 4.5). Cellular traction force response during increasing substrate strain varied considerably across the observed population. The initial response, from 0-2% substrate strain, of all cells (N = 25) was an increase in strain energy imparted to the mPAD. Energy increases ranged from 5% - 40%. At strain values greater than 2%, cell to cell traction force dynamics varied greatly. While the increasing strain energy response persisted for a fraction of the cells tested (Figure 4.4 A, B; Figure 4.5 A, D), many cells exhibited a "plastic limit", after which contraction energy would remain constant, decrease, or a time and strain varying combination of both (Figure 4.4 C,D,E,F; 4.5 B, C, E, F) . However, despite the varying responses to increasing strain, at the onset of decreasing substrate strain, cell tractions promptly decreased in all cases, falling below the values observed during increasing strain. Cell traction energies continued to decrease until stretch cessation, resulting in a final energy below pre-stretch levels, consistent with measurements performed immediately following the previous short duration stretches (Figures 4.1, 4.2).

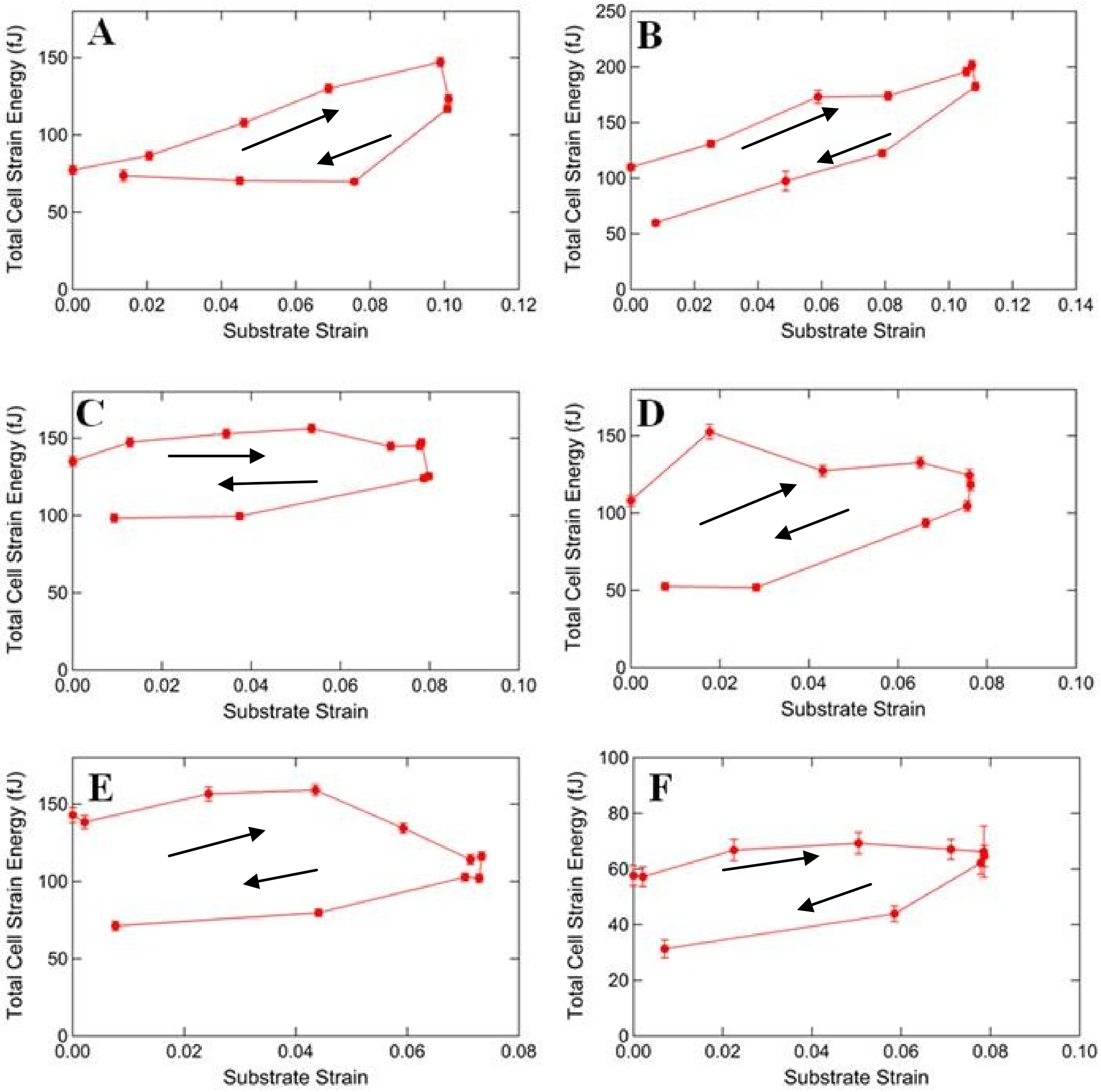

Figure 4.4: Total cell strain energy versus substrate strain for a representative sample of BPASMCs. Maximum strain values for these cells were 7% - 11%. Strain protocol was as depicted in Figure 4.3 A.

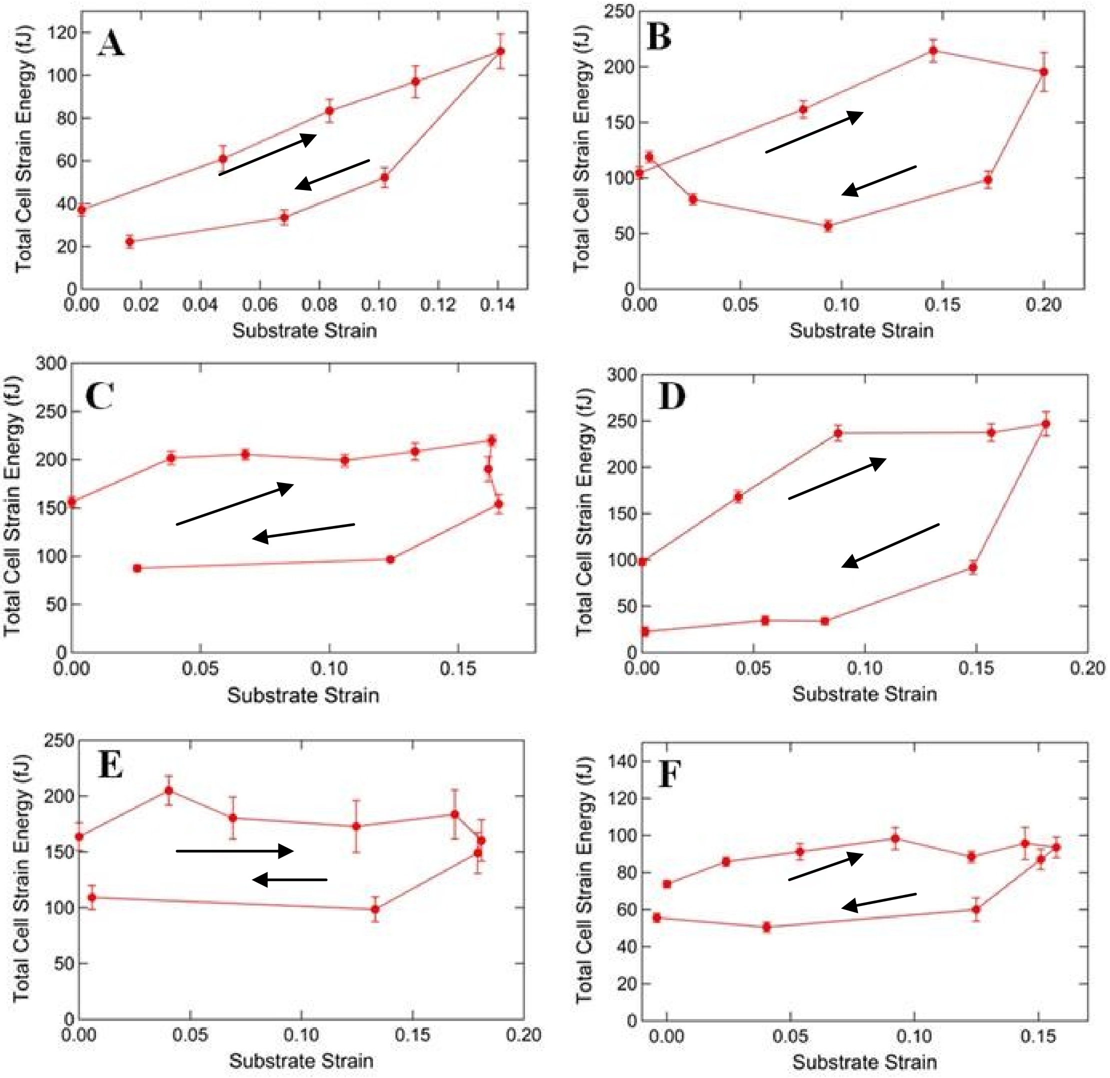

Figure 4.5: Total cell strain energy versus substrate strain for a representative sample of BPASMCs. Maximum strain values for these cells were 14% - 20%.

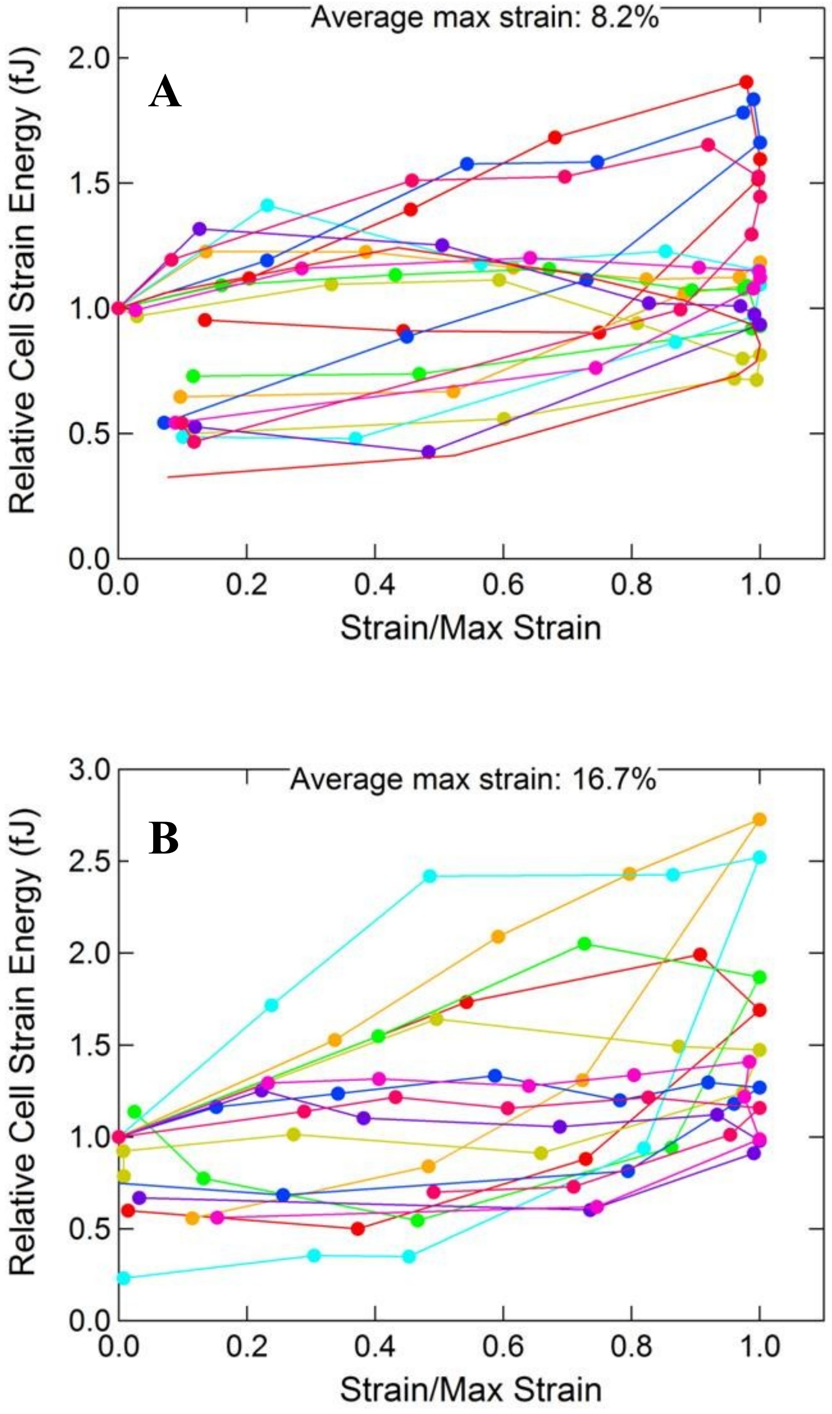

Figure 4.6: Relative strain energy vs. normalized substrate strain for multiple single SMCs shown in two groups with average strain values of 8.2% (A) and 16.7% (B). All cells exhibit hysteresis, with considerable variability in traction force response during increasing substrate strain.

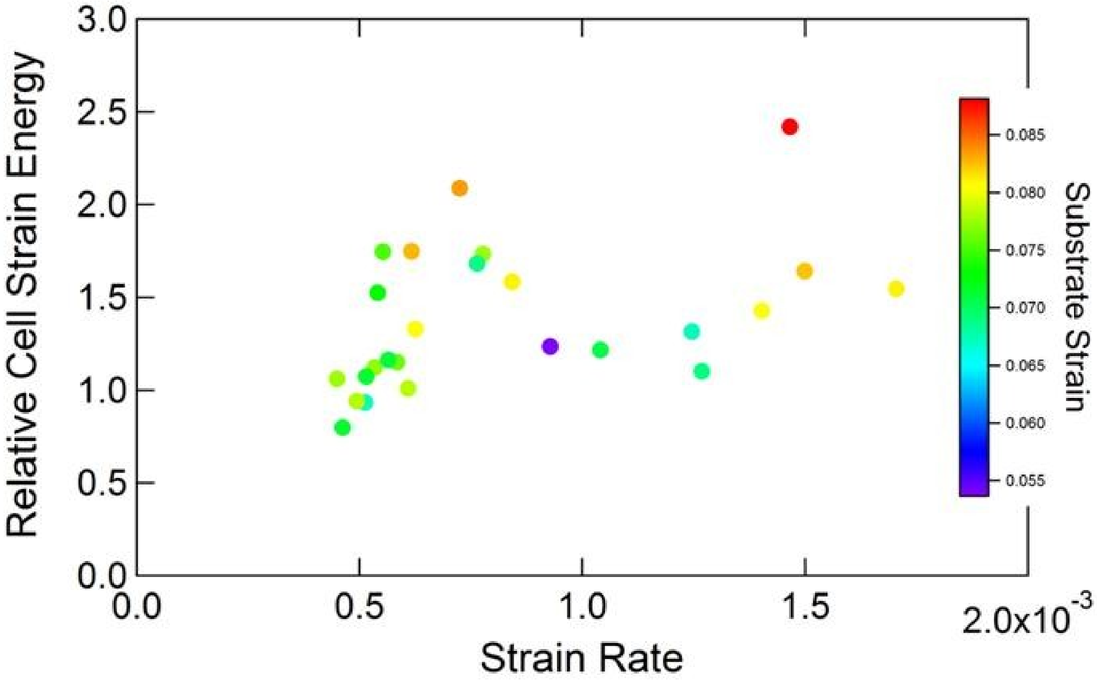

Figure 4.7: Relative cell strain energy vs. strain rate for all cells tested. Energy values correspond to substrate stains of 7.5% ± 1% I order to include cells from all strain ranges tested.

Figure 4.7 shows the relative change in cell strain energy @ 7.5% ± 1% strain vs. strain rate for 25 cells. While a weak positive correlation exists between the relative change in cell strange energy and strain rate, plots of relative cell strain energy versus (scaled) substrate strain (Figure 4.6 A, B) reveal a heterogeneous response to increasing strain across our tested cell population. 13 out of 25 cells exhibited energy changes during increasing substrate strain that did not exceed 50% of baseline, and the remaining 12 out of 25 cells exhibited a reinforcing response, with energy increases exceeding 50% prior to strain reversal. Worth noting, 4 of the 12 reinforcing cells did show energy decreases during increasing substrate strain, but only after an initial increase of greater than 50% of baseline.

Consistent with the response to short duration stretches described in the last section, left at rest, cell traction forces slowly recovered over the course minutes, and again showed significant variability in quasi-equilibrium strain energy values following recovery. This can be seen in Figures 4.8, 4.10, and 4.12 that show total cell strain energy vs. time (A) and total cell strain energy vs. strain (B) that include the recovery period following stretch cessation.

A more detailed analysis of cellular traction force dynamics is shown below for three representative cells that span the range of observed responses. Data for each cell is shown using a pair of figures. In Figures 4.8, 4.10, and 4.12, total cell strain energy and substrate strain vs. time are shown in panel A, and cell strain energy vs. substrate strain is shown in panel B. Force vector maps pertaining to data points indicated on the plots in A and B show the change in cellular traction forces during the course of stretch application (Figure 4.8 C-G; Figures 4.10 and 4.12, C-F). The second figure for each cell (Figures 4.9, 4.11, and 4.13) contains information about the evolution of the spatial distribution of cell strain energy imparted to the mPAD. Panel A in each of these figures contains traces of strain energy vs. time for each individual post to which the cell is adhered (cell posts). The right column of panels is heat maps that allow for easy visualization of strain energy distribution across the cell. The heat maps correspond to the same data points indicated by arrows on the plots of the previous figures, and are numerically labeled for the specific data point that they represent. The remaining panels (Figure 4.9 B-E; Figures 4.11 and 4.13 B-D), are plots of strain energy in a given frame vs. strain energy in an earlier frame for each cell post, where the axis labels again correspond to the previously indicated data points also labeling the heat maps. These plots indicate how the energy stored in each cell post evolves from one point to the next in response to the applied stretch. Individual posts that gain energy will lie above the y = x line (blue trace), while those that lose energy will be below the y=x line.

This analysis revealed that the measured whole-cell responses, which varied significantly from cell to cell, were generally uniform across all high energy cell posts (Figures 4.9 A, 4.11 A, and 4.13 A), and that the changes were restricted to regions of strong force generation (Figures 4.9, 4.11, and 4.13, heat maps). The remaining plots in Figures 4.9, 4.11, and 4.13 further demonstrate the uniformity of the changes in total cell strain energy that occurred between the selected time points, as the positions of nearly all posts moved synchronously relative to the y = x trace.

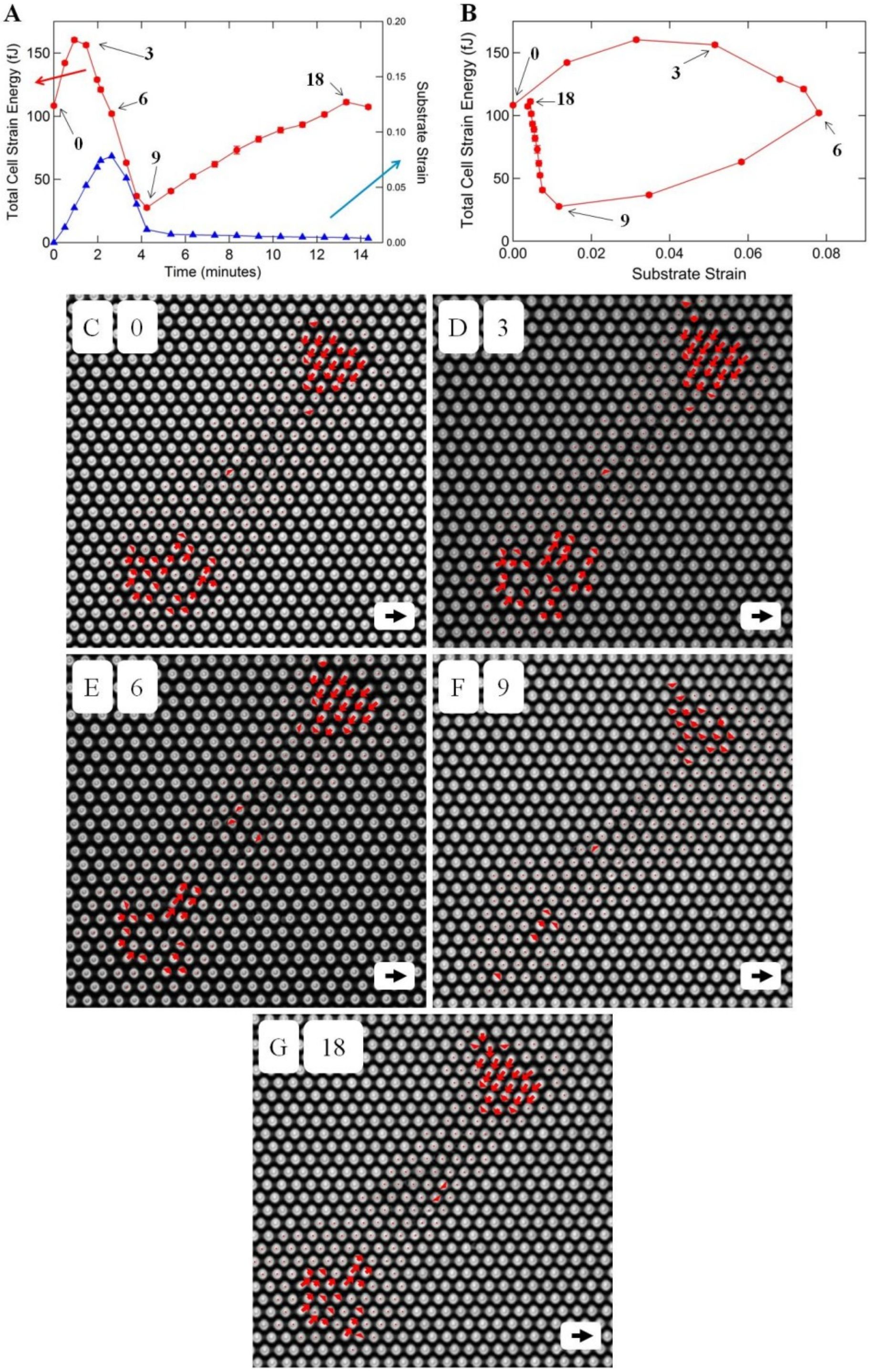

Figure 4.8: (A) Plots of cell strain energy (red, left axis) and substrate strain (blue, right axis) vs. time. (B) Cell strain energy vs. substrate strain. (C-G) Force vector maps for selected time points (numeric label) during stretch application. Points of interest indicated on plots by black arrows. Scale vector is 10 nN.

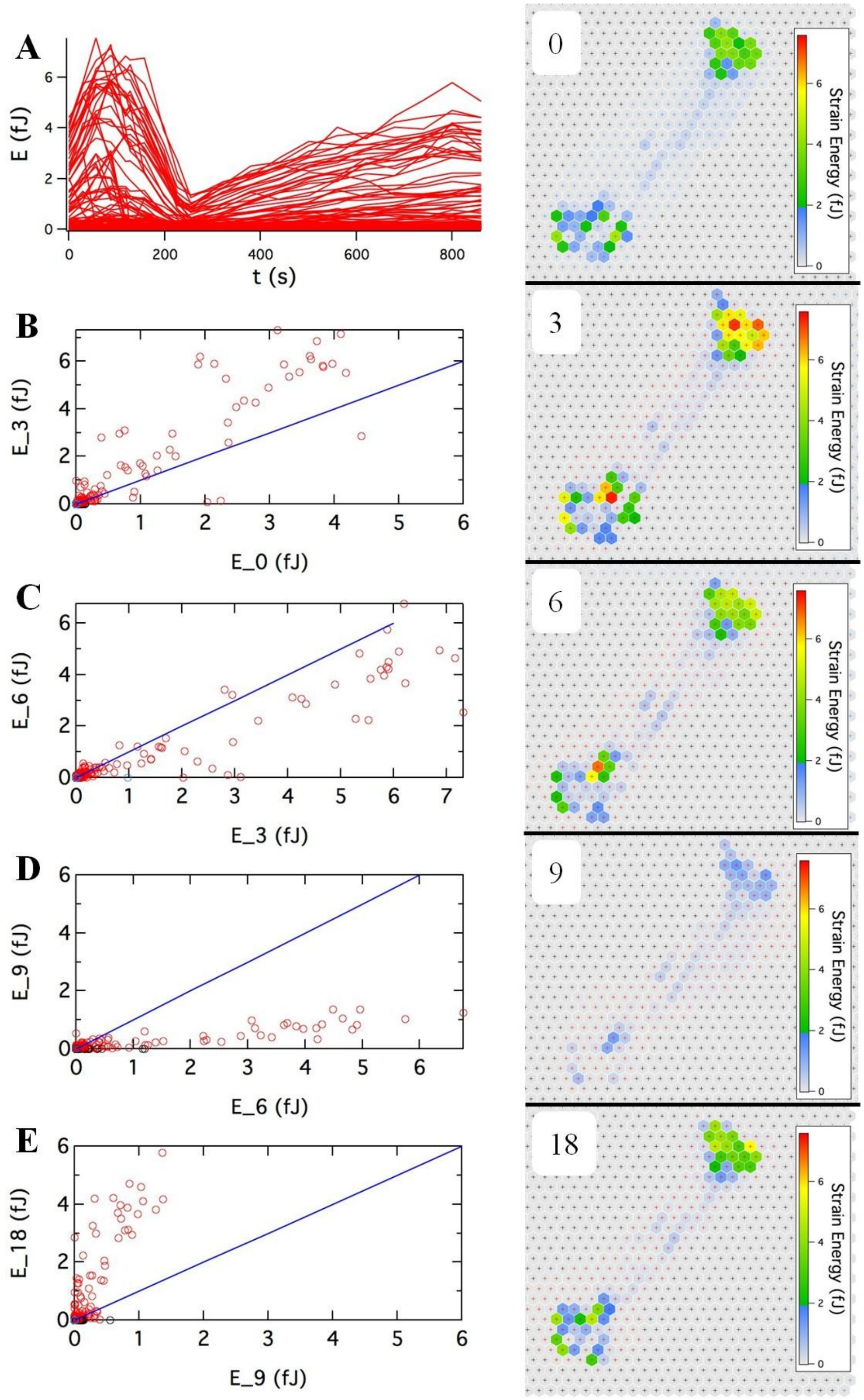

Figure 4.9: (A) Strain energy vs. time for each individual cell post. Right column: Energy distribution heat maps across the entire cell. Each map corresponds to a selected time point during stretch application (numeric labels, see Figure 4.8). (B-E) Energy evolution between time points indicated on axes (also see corresponding heat maps). y = x line (blue trace) represents no change in energy.

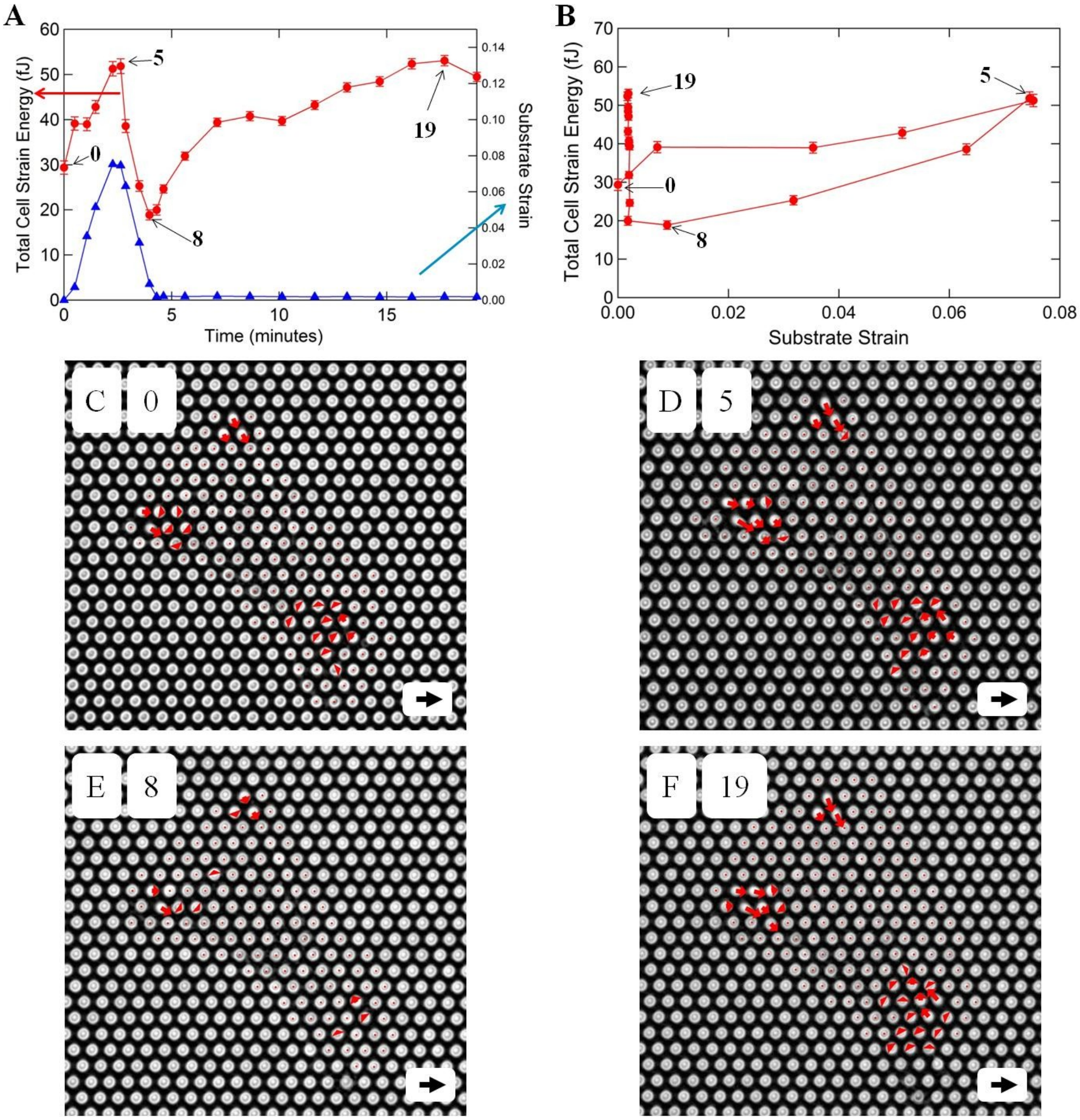

Figure 4.10: (A) Plots of cell strain energy (red, left axis) and substrate strain (blue, right axis) vs. time. (B) Cell strain energy vs. substrate strain. (C-F) Force vector maps for selected time points (numeric label) during stretch application. Points of interest indicated on plots by black arrows. Scale vector is 10 nN.

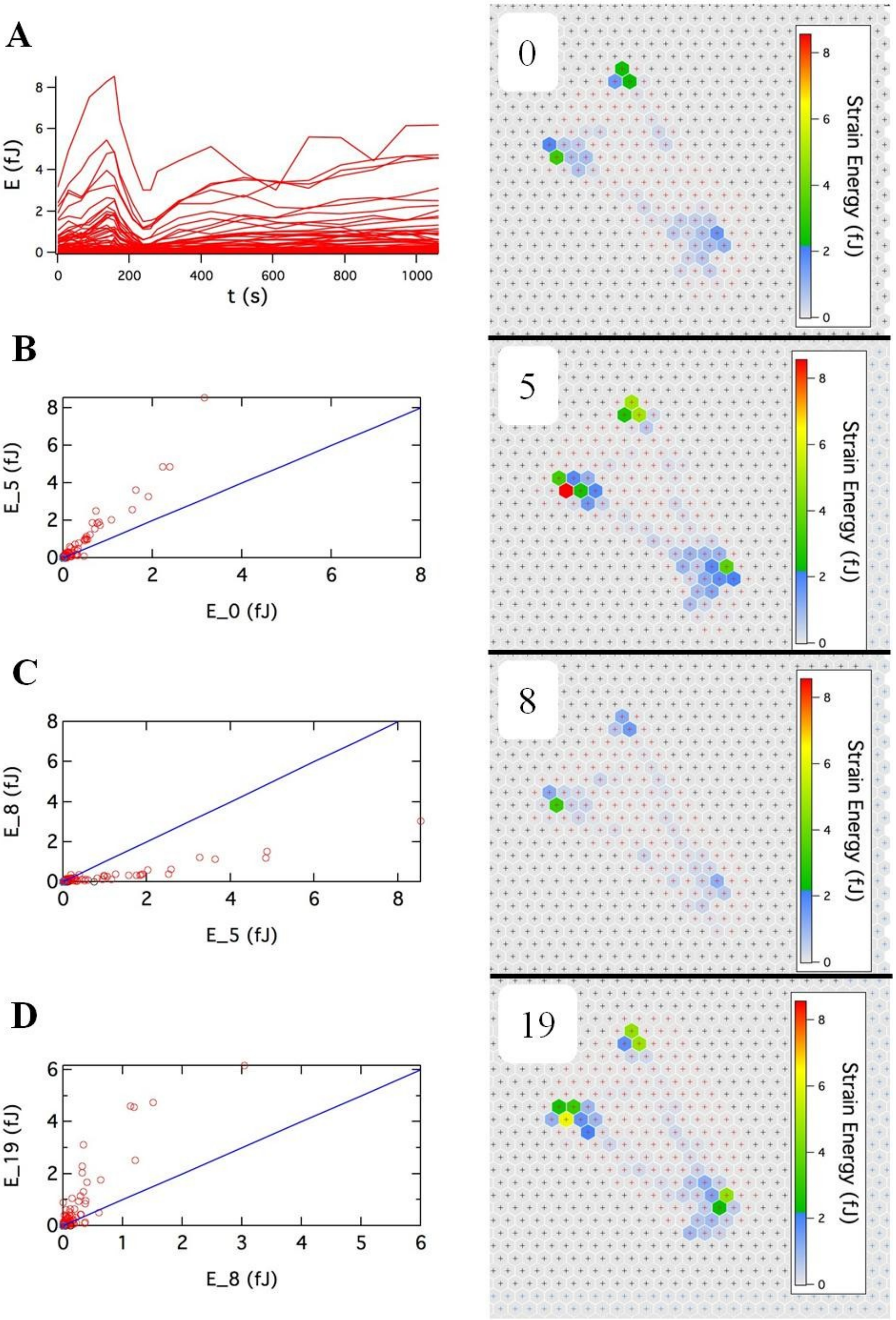

Figure 4.11: (A) Strain energy vs. time for each individual cell post. Right column: Energy distribution heat maps across the entire cell. Each map corresponds to a selected time point during stretch application (numeric labels, see Figure 4.10). (B-D) Energy evolution between time points indicated on axes (also see corresponding heat maps). y = x line (blue trace) represents no change in energy.

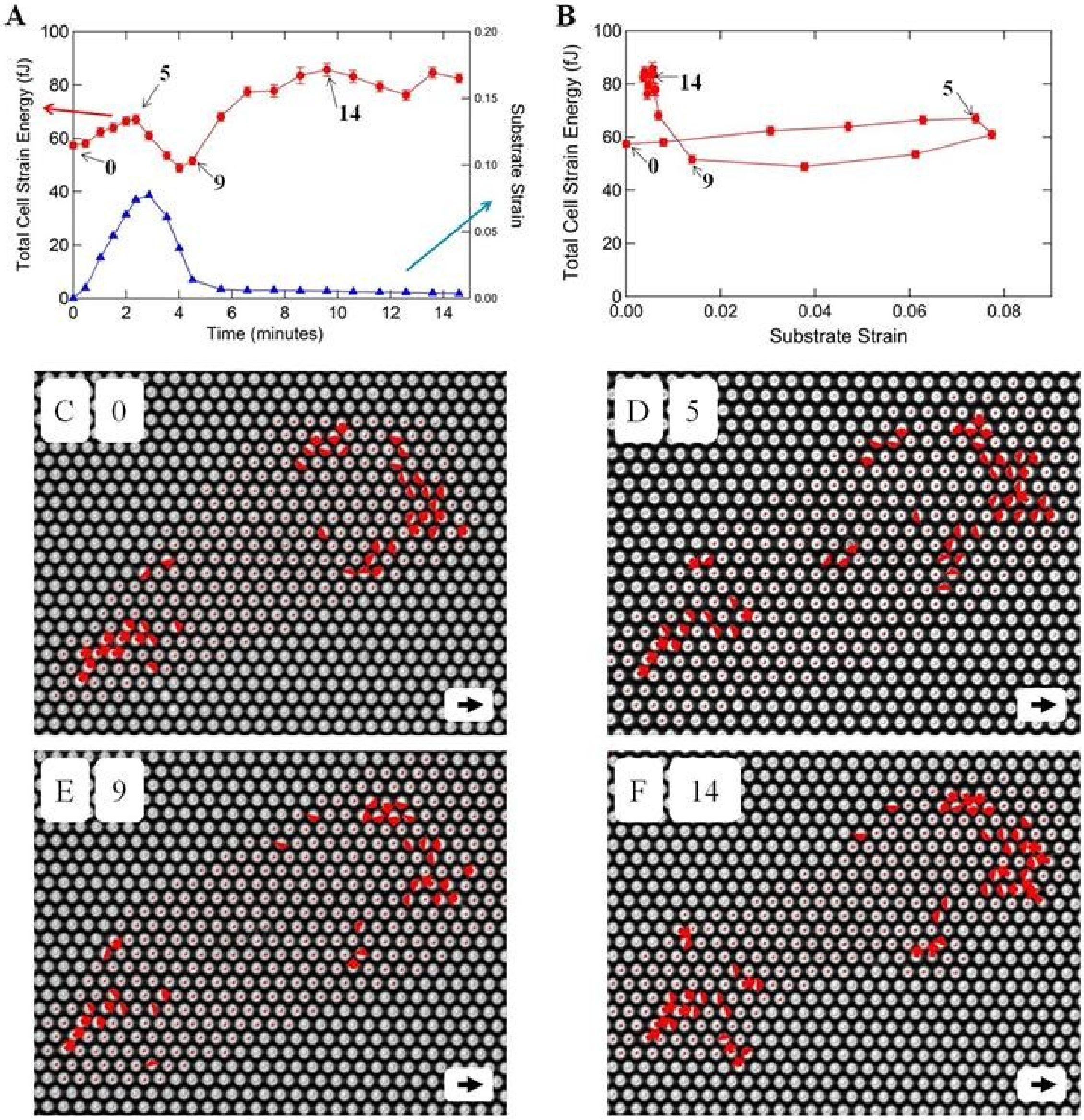

Figure 4.12: (A) Plots of cell strain energy (red, left axis) and substrate strain (blue, right axis) vs. time. (B) Cell strain energy vs. substrate strain. (C-F) Force vector maps for selected time points (numeric label) during stretch application. Points of interest indicated on plots by black arrows. Scale vector is 10 nN.

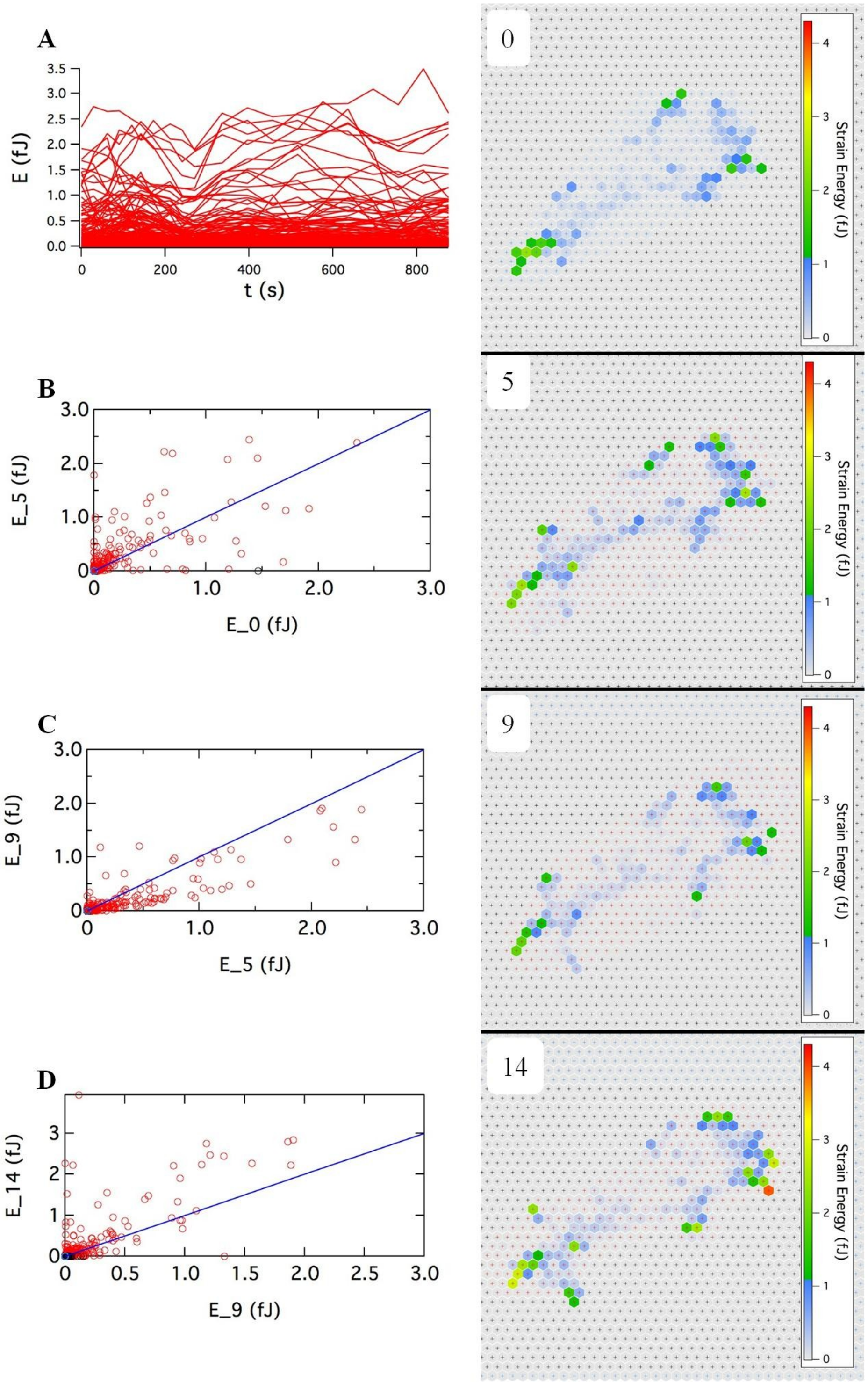

Figure 4.13: (A) Strain energy vs. time for each individual cell post. Right column: Energy distribution heat maps across the entire cell. Each map corresponds to a selected time point during stretch application (numeric labels, see Figure 4.12). (B-D) Energy evolution between time points indicated on axes (also see corresponding heat maps). y = x line (blue trace) represents no change in energy.

4.3.3 Virus

In order to enhance the cells' ability to actively generate force and observe the effect on the traction force response during applied stretch, cells were treated to express constitutively active RhoA via transfected with V14 adenovirus (Section 2.1.3). When exposed to long duration stretches and imaged *during* the stretch process, the overall response of Rho-V14 expressing cells (Figures 4.14 A-D, 4.15 A-E) was not significantly different from either control cells or cells virally treated to express GFP (not shown).

As mentioned previously, control cells imaged before and after exposure to a 7-10% stretch of 5s duration showed an average whole cell strain energy drop of 49.77% (n=13). The same stretching protocol performed on RhoV14 expressing cells showed an average drop of only 20.62% (n=12). The recovery response following stretch cessation was not significantly different from controls for either the short duration (Figure 4.16) or the long duration stretches (Figures 4.15, 4.16). While a difference in response was observed between RhoV14-expressing cells and controls cells exposed to short duration stretches, RhoV14 expression caused reduced spreading on mPADs, which may have altered cytoskeletal actin distribution in these cells.

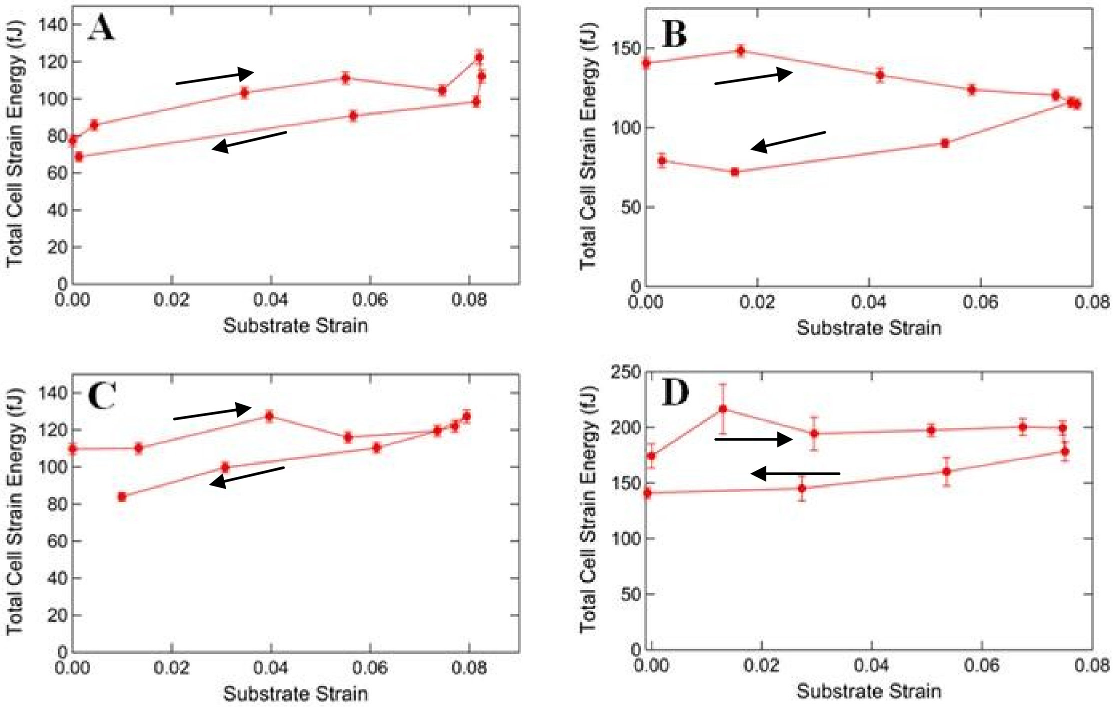

Figure 4.14: Total cell strain energy vs. substrate strain for four Rho-V14 expressing BPASMCs observed during stretch application. Overall responses are not significantly different from controls.

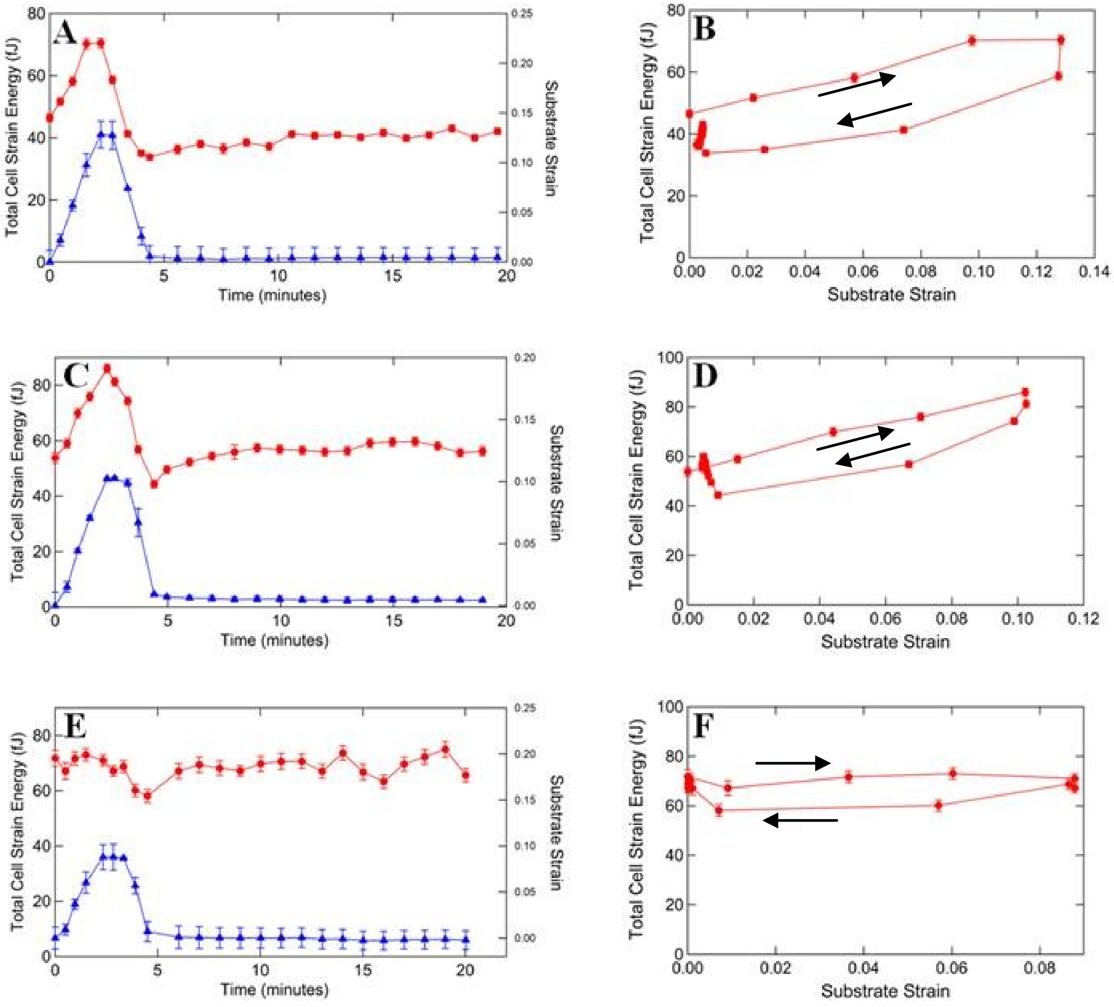

Figure 4.15: (A, C, E) Total cell strain energy (red, left axis), substrate strain (blue, right axis) vs. time, and strain energy vs. substrate strain (B, D, F) for three Rho-V14 expressing BPASMCs observed during stretch application.

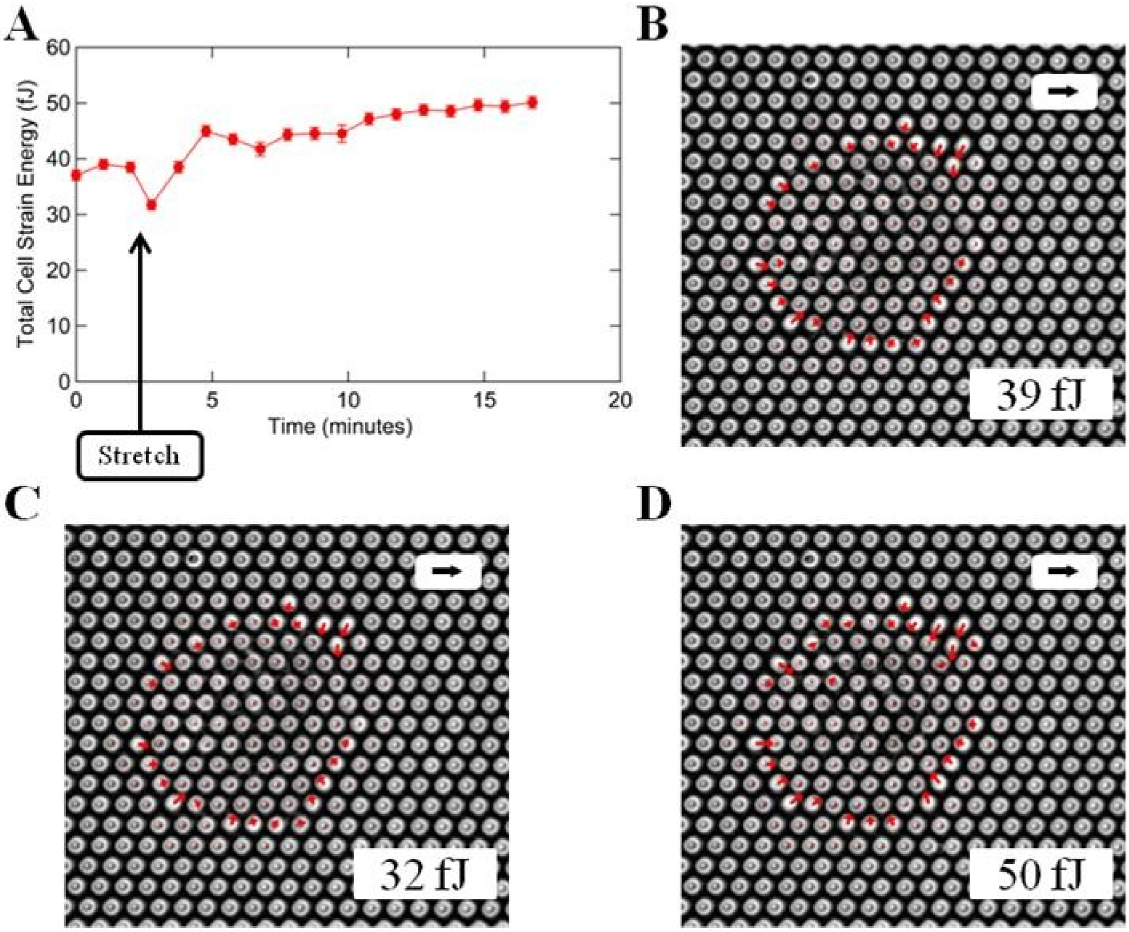

Figure 4.16: (A) Whole cell strain energy vs. time for a Rho-V14 expressing BPASMC exposed to a transient 8% stretch of 5s duration. Vector maps of cellular traction forces prior to stretch application. (B), immediately following stretch (C), and 14 minutes after stimulation. Scale vector is 10 nN.

4.3.4 Sustained Stretch

To further examine the response of BPASMCs to stretch stimulus, our experimental setup was used to expose cells to a sustained stretch. This was achieved by bringing the flexible mPAD substrate to the desired strain level and then holding the vacuum pressure constant over time (Figure 4.17). The few cells tested in this way exhibited elastic energy increases during the onset of stretch, followed by decreasing energy prior to reaching maximum substrate strain. While strain was held constant, each cell exhibited decaying strain energy imparted to the mPAD.

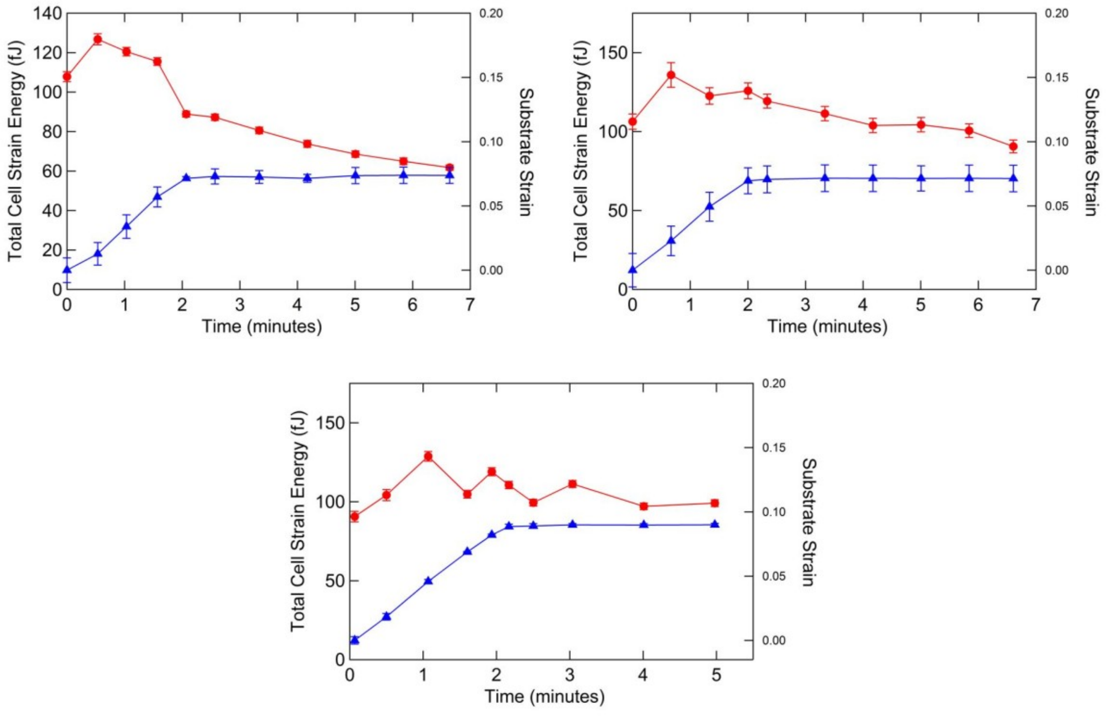

Figure 4.17: Total cell strain energy (red, left axis) and substrate strain (blue, right axis) vs. time for three BPASMCs exposed to a sustained stretch.

4.3.5 Cell Pairs

Patterning techniques described previously were used to culture cells in pair configurations on flexible mPADs for stretch application (Figures 4.18 A, 4.19 A). Measurement of whole cell strain energy during stretch for each cell individual cell a pair shows a global response similar to that observed for single cells. Worth noting is that the response of paired cells displays a degree of synchronization (Figures 4.18 B, 4.19 B). Determination of the force acting at cell-cell adhesions (cell-cell force, Section 2.3.3) shows that not only do cell-cell adhesions remain intact during stretch, but the response to stimulus of the force acting at these sites is modulated synchronously with cell-substrate forces (Figures 4.18 C, 4.19 C). Even though the cell-cell force for the pair in Figure 4.19 is relatively low magnitude, the response still captures the hysteresis characteristics of the cell-substrate force response.

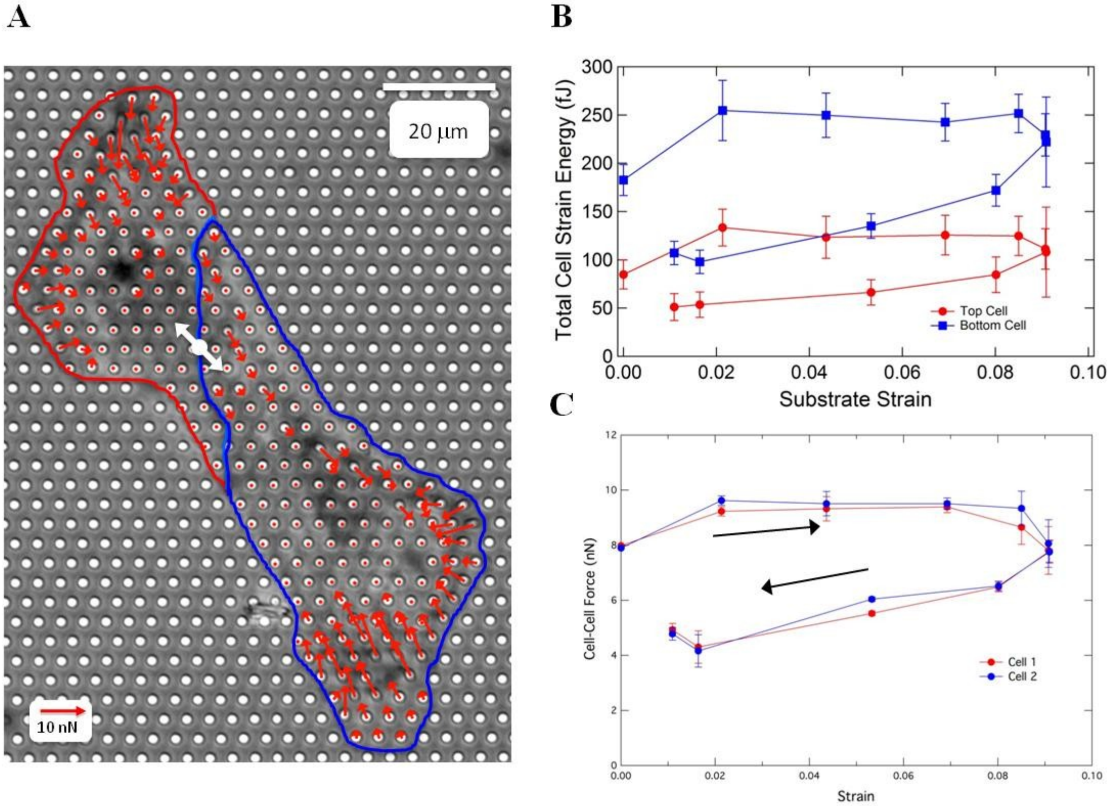

Figure 4.18: (A) Phase contrast image of a cell pair adhered to an mPAD. Cell one is outlined in red, cell two in blue. Cell-substrate force vectors are shown in red and cell-cell force vectors in white. (B) Total cell strain energy vs. substrate strain for both cells. (C) Cell-cell force vs. substrate strain as calculated from unbalanced cell-substrate forces for each cell.

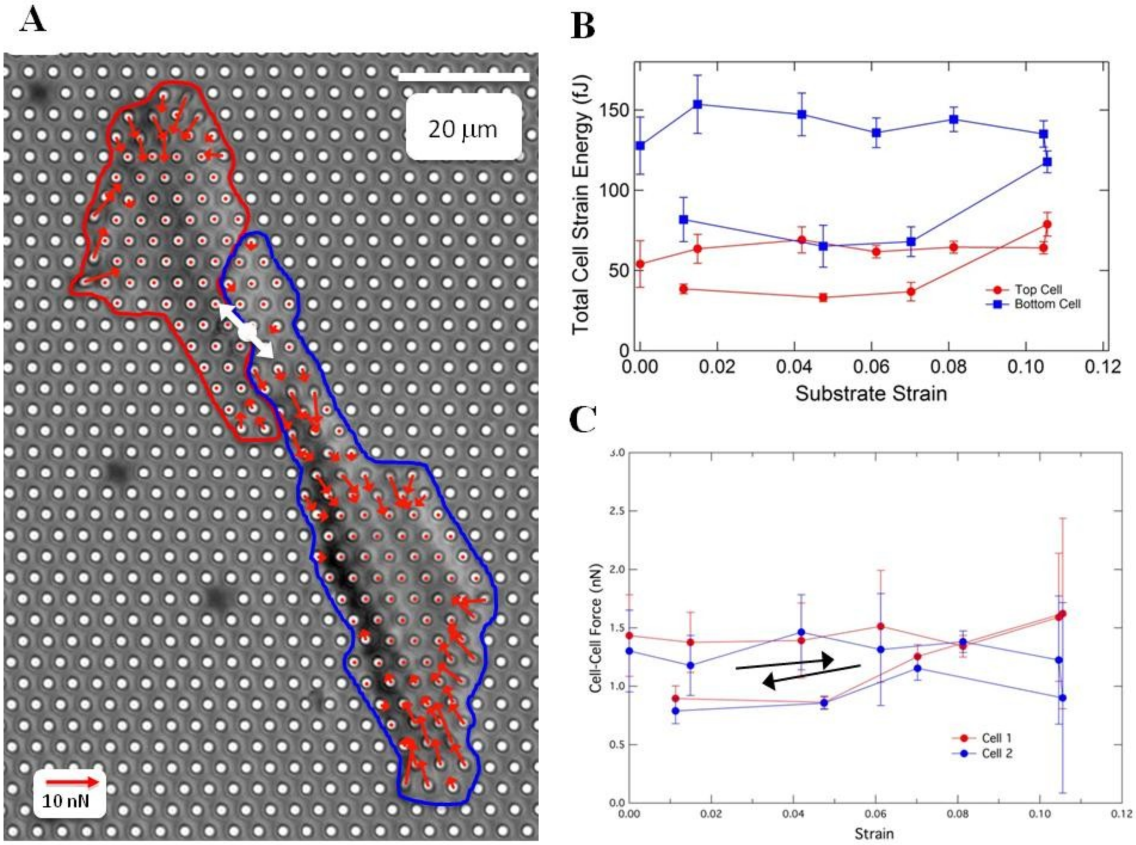

Figure 4.19: (A) Phase contrast image of a cell pair adhered to an mPAD. Cell one is outlined in red, cell two in blue. Cell-substrate force vectors are shown in red and cell-cell force vectors in white. (B) Total cell strain energy vs. substrate strain for both cells. (C) Cell-cell force vs. substrate strain as calculated from unbalanced cell-substrate forces for each cell.

4.4 Discussion

Fast Stretch. The traction force response of BPASMCs exposed to a short duration (5s) transient stretch of 10% magnitude is consistent with previous findings for human airway smooth muscle cells (HASMCs) [39] and human bladder smooth muscle cells (HBSMCs) [40]. Namely, a prompt decrease in traction forces immediately after stretch cessation, followed by slow recovery over the course of minutes. The resulting quasi-static equilibrium values following recovery for HASM and HBSM cells were generally reported to be equal to pre-stretch values, or slightly below. While our results showed that this was indeed the case for many of the BPASM cells tested, some cells reached new contractile energy values that were much greater than pre-stretch levels. Similar results for HASM and HBSM cells were found only after exposure to non-homogeneous stretches, where the strain field varied continuously across the cell.. Our results show that while there may be two mechanisms responsible for the response to either homogeneous or non-homogenous stretch, some overlap exists allowing for BPASMCs to sometimes reinforce following homogeneous stretch. The studies mentioned then explored the affect of transient stretch on the structural dynamics of cytoskeletal actin fibers. Immunostaining for both the filamentous (f-actin) and globular (g-actin) forms of actin revealed that actin in cells exposed to transient stretch underwent rapid depolymerization following stretch, observed as a significant increase in the ratio of g-actin to f-actin. However, these experiments were only able to observe cell traction forces and cytoskeletal dynamics prior to and following transient stretch, and therefore concluded that the rapid depolymerization of actin was coincident with the drop in traction forces. This effect was hypothesized to perhaps be the result of catch bonds acting to reinforce the cytoskeleton during loading, which promptly release upon de-loading during stretch reversal [40].

Observation during long duration stretches. The functionality of our experimental setup enabled us to observe cellular traction force dynamics *during* stretch application, while substrate strain was actively changing. These measurements showed that the sub-baseline traction forces observed following transient stretch are initiated at the onset of strain reversal. For all but one cell tested, strain energy decreased significantly in the vicinity of strain reversal, and continued to decrease below baseline values as the stretch completed. This shows cellular relaxation to be, in part, a result of relatively small changes in strain dynamics and not only due to the dramatic physical forcing of more rapid stretch application and release. The global nature of this response is made clear by noting that the strain energy dynamics for the vast majority of cell-attached posts were consistent across the entire cell. This change in strain energy imparted to the mPAD substrate displays a hysteresis that is characteristic of the response of a viscoelastic material to applied stretch, although the energy loss indicated by the area contained within the loop varied greatly from cell to cell.

Our experiments also revealed a significant degree of variability in the cellular response to increasing substrate strain. While a subset of the cells tested exhibited behavior that was consistent with the catch bond theory proposed by Fredberg et al.[40]: an elastic reinforcement of traction forces, presented as increasing whole cell strain energy; many cells displayed a more passive response to increasing substrate strain. These cells appeared to reach a “plastic limit” following an initial elastic response, after which traction forces remained relatively constant or even decreased while substratestrain was still increasing. Spatial analysis revealed that relative energy changes associated with both response modes were uniform across the entire cell. Given that contractile force is generated through relative motion of actin fibers, the ability of a cell to, following an initial increase, virtually maintain the magnitude and spatial orientation of its traction forces during application of global strain is a surprising result. This apparent transition in cytoskeletal tension may indicate that the depolymerization response observed following stretch can occur *during* stretch, even before the reversal of strain direction that ultimately facilitates a release in tension. While typical immunostaining protocols that require fixation would likely be disrupted on a flexible substrate, the use of cells genetically modified to express fluorescent actin fibers would allow for characterization of actin dynamics during applied stretch.

Previous studies by Hirata et al. found that exposure to large sustained uniaxial stretch of 50% magnitude for 30s induced actin polymerzation at focal adhesions in a zyxin and force dependent manner in human foreskin fibroblasts, and was reversible in response to decreased tension [41]. Consistent with these findings, zyxin, which regulates actin polymerization at focal adhesions in response to changes in tension, could play a role in actin depolymerization following strain reversal (tension release). However, the recruitment of actin found during applied stretch seems to contradict our findings that BPASMCs can begin to relax and decrease force generation in response to a biaxial stretch, indicating that the action of zyxin may be overridden by global changes in the cytoskeleton, or somehow specific to uniaxial forcing.

Sustained stretch. When exposed to a sustained stretch, cellular traction forces again showed the relaxation response that was previously observed for some cells during increasing strain, and this response continued while maximum substrate strain was maintained. Previous experiments that measured the concentration of intracellular calcium demonstrated an increase in intracellular calcium in response to both homogeneous [42] and inhomogeneous [43] stretches in fibroblasts and endothelial cells, respectively. Increased intracellular calcium is well known to facilitate increased contraction (Section 1.1.2). Our results demonstrating the relaxation response to a sustained stretch may indicate that the influx of calcium observed in response to stretch in other cell types is ineffective at increasing contractility during global stretch. This supports the hypothesis that global cytoskeletal disruption is the likely driving force behind stretch induced relaxation of traction forces.

Rho-V14 expression. While it has been shown that Rho, and also constitutively active Rho-V14, has significant affects on stress fiber organization and remodeling associated with cyclic stretching [44], our experiments using Rho-V14 expressing BPASMCs did not show a significant difference in traction force response during a single applied stretch as compared to controls. This is in contrast to changes in traction forces in response to more rapid ~5s stretches, where Rho-V14 expressing cells exhibited a significantly smaller decrease in whole cell strain energy as compared to controls. While constitutively active Rho would certainly lead to increased force generation, as seen in microtissues (Copeland, Liu, Zhao, Chen and Reich, in preparation), Rho-V14 expression did not cause an obvious increase in forces imparted to microposts. This is likely due the reduced ability of single BPASMCs to spread on mPADS that was observed. Given that the response of Rho-V14 expressing microtissues to applied stretch was not significantly different from controls, despite an overall increase in force generation, the difference in response to 5s stretches on mPADs may instead be a result of reduced spreading area. Reduced spreading area may cause an increase in stress fiber overlap across the cell that renders the cytoskeleton more resistant to short duration stretching forces, thereby increasing the strain a cell is able to endure prior to the onset of force-induced remodeling.

Cell pairs. Stretch experiments performed on patterned cell pairs demonstrated that while cell-cell interaction does not alter the viscoelastic behavior of cells in response to stretch, it does result in a degree of synchronization in the dynamic response between the two cells. As well, the ability to measure cell-cell forces present in these pair configurations during applied stretch showed that cell-cell adhesions remain intact and under tension during the cytoskeletal remodeling associated with exposure to stretch, and that forces generated at cell-cell adhesions are regulated synchronously with traction forces at cell-substrate adhesions. Common regulation of cell-cell and cell-substrate forces is consistent with global cellular relaxation caused by cytoskeletal disruption in response to stretch.

Taken together, these results have demonstrated that the responses of cell generated contractile forces to applied strain are globally regulated and likely due to cell-wide disruption of cytoskeletal integrity.

Chapter 5 Local Chemical Stimulation

The combined use of techniques for measuring cell generated forces and local application of chemical treatment at the cellular level can not only improve experimental efficiency, but may provide interesting paths forward in the study of cell-cell interactions. Described below is the development of experimental techniques combining micropipette facilitated fluid flow ("spritzing") for controlled delivery of biochemical treatments with the aforementioned mPAD system and with a system for measuring the mechanical properties of microtissues.

5.1 Introduction

Experimental methods developed to supply biochemical stimulation to controlled regions of two dimensional cell culture provide a useful means of probing biological systems. These methods often make use of micropipettes [45-47]. These devices allow for controlled delivery of biochemical solution to regions of culture down to the single cell level. Combining these techniques with optical microscopy enables experiments where single cell responses can be observed in real time without exposing cells in the surrounding culture, which are not under observation, to the desired treatment. This allows multiple cells to be sequentially exposed to treatment, while each is under high-magnification observation. The increased experimental efficiency made capable by these setups is particularly important when, for example, high value cell lines or samples that are difficult to prepare are being studied. In these cases, unobserved exposure to treatment renders the bulk of the substrate unusable for further data collection.

Microfabricated devices used in our lab allow for real time measurement of force generation by single cells, via mPADS, or single microtissues, via µTUGs [48]. In both cases, the cell or tissue under observation is located on a PDMS substrate that contains many cells or microtissues that are suitable for experimentation, all sharing a common bulk media bath. Hence, biochemical treatment through supplementation directly into the media bath will treat all available cells/tissues simultaneously. I have demonstrated the combined use of a local chemical stimulation technique termed "micropipette spritzing" with mPAD and µTUG devices in order to more efficiently treat and observe single cells and microtissues. In addition, I have shown how this technique can be used to selectively manipulate cells in culture on mPADs in order to create physical stimulus through cell-cell interactions.

5.2 Methods

5.2.1 Micropipettes

Micropipettes (TW-150F-4, World Precision Instruments) were pulled using a two stage Kopf 720 Needle Pipette Puller (Kopf Instruments). This puller operates by securing a single pipette held vertically at each end, with a heating element located around the center. As the element heats, a weight located where the bottom end of the pipette was secured draws the lower half of the pipette downward a fixed distance. The puller was then set to the next heat value, or "stage", and taken through the same process. Pipettes of the desired size required 4 heating stages. The first heat setting is used for the first stage of pulling, and the final 3 settings are used while repeating the 2nd stage process of pulling until the two pipette halves separate. Pipettes with tips approximately 50 µm in diameter, were obtained using heat value dial settings of 8.4, 6.8, 6.8, and 6.4. For tips 20 µm in diameter, heating values of 8.4, 6.8, 6.8, and 6.8 were used.

5.2.2 Experimental Setup

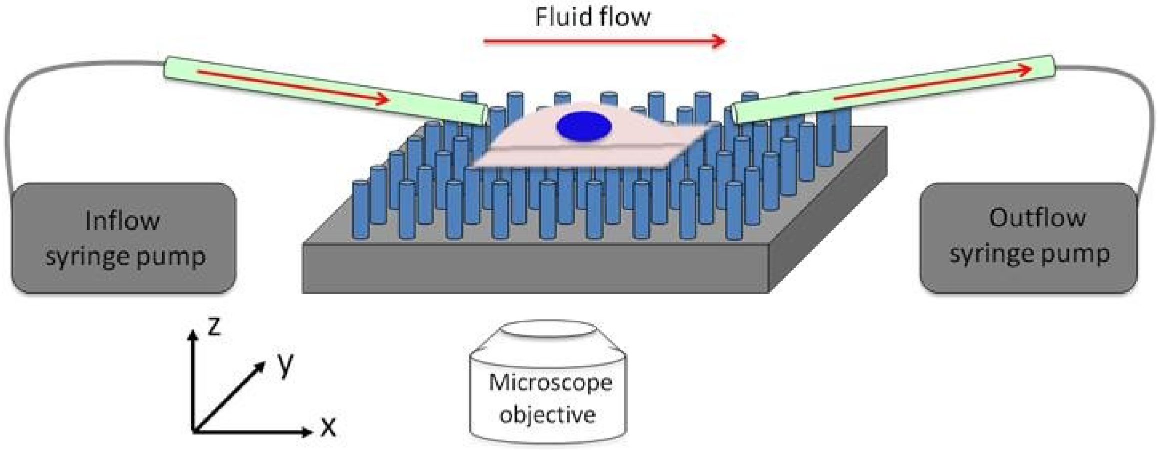

Figure 5.1: Schematic diagram of micropipette spritzing experimental setup being used for single cell treatment on mPADs.

A custom built platform mounted onto the microscope stage supports two micro-manipulators that in turn hold mounting devices for the micropipettes. The manipulator setup allowed for precise control of each micropipette, independent of each other and the microscope stage. Vacuum tubing connects each pipette to its own syringe pump for independent control of fluid flow (Figure 5.1). Precise control of the treatment region (the flow plume between the pipettes), required that the user be able to observe the flow edges. In order to visualize the flow plume, the incoming drug supplemented media did not contain serum. The absence of serum caused a sufficient index of refraction difference between the inflowing media and the bath for visualization using phase contrast microscopy. A 1 ml syringe was typically used for the inflow solution in order to conserve reagents. In order to remove as much air as possible from the system, the outflow syringe, tubing, and pipette were all loaded with un-supplemented media, containing no serum or antibiotics. It was important to make sure that all syringes, lines, and pipettes were free of air bubbles in order to reduce lag when controlling the flow. Once loaded, pipettes were raised as high as possible and positioned for maximum downward angle. An angle of ~45 degrees ensured that inflowing solution was directed downward and would contact the base of the substrate before traveling to the outflow pipette. Using a 4x objective, the pipette tips were located and positioned just above the media surface before changing to the 10x objective. Tips were then moved to a region above the substrate that was far from the cells to be treated. The outflow pipette was moved to just below the media surface with the flow rate set high (~9000 µl/hr). Next, the inflow pipette, with its syringe pump still off, was lowered directly in front of the outflow pipette. Once contact with media was made, the high rate of outflow ensured any solution leaking out of the inflow was immediately removed from the bath. Flow rates were then adjusted to the lowest possible rate that produced a controllable flow plume. Typical rates were 10-50µ/hr for the inflow and 100-500µl/hr for the outflow.

When not flowing for treatment, tips were left very close together with the outflow at an “idle” rate of 200µl/hr to account for any remnant leakage from the inflow pipette. With the pipette tips submerged and ready for use, a suitable construct for the device and experiments being used was selected and imaged in order to establish a baseline measurement. With the pipette tips still a few hundred microns from the construct of interest, flow was initiated and given time to stabilize. The microscope stage was then adjusted to bring the treatment area into view, and the pipette tips were slowly moved using the micro-manipulators until they were in place for the desired treatment. The cellular construct and flow plume were imaged using the 10x objective to document the flow position (Figure 5.2), after which the construct under treatment was imaged over time using either the 40x or 60x objective.

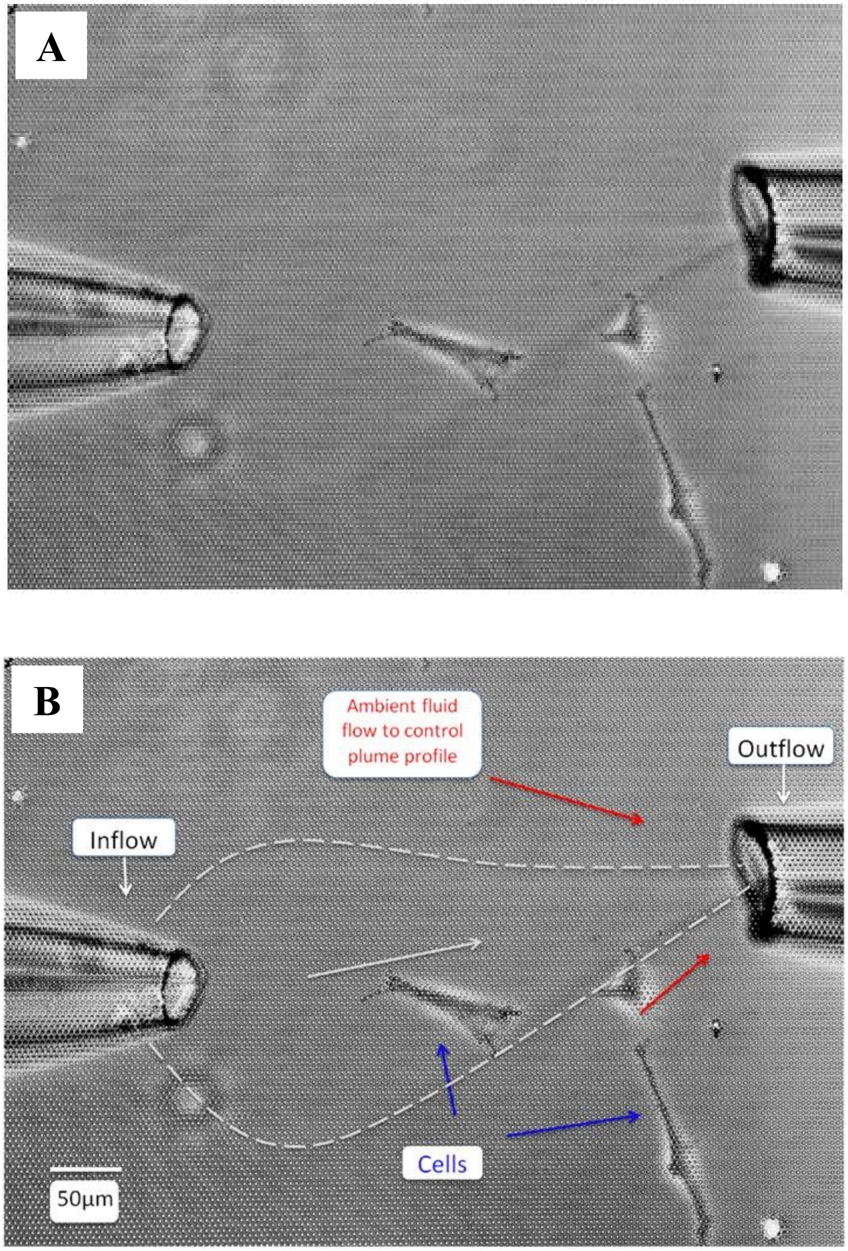

Figure 5.2: Phase contrast image of a spritzing experiment. (A) Phase contrast image showing flow plume between the inflow (left) and outflow (right) pipettes. (B) Detailed schematic indicating treatment fluid flow plume and direction indicated in grey, ambient bath fluid flow is indicated by red arrows. Cells cultured on mPAD surface are indicated by blue arrows.

In order to characterize the flow field generated by the micropipette system, experiments performed by David Hunter in the Tung lab measured the relative conductance between a probe located in the inflow pipette and one located in the bath using a flow solution of 0.1M NaCl and a bath of de-ionized (DI) water (Figure 5.3 A). The bath probe was moved relative to the edge of the visible flow (Figure 5.3 A, solid black line), and the relative conductance was measured. This was performed at five different distances away from the inflow pipette, designated by the colored dashed lines in Figure 5.3 A. The plot in Figure 5.3 B shows traces of conductance versus the distance from the flow edge, designated by x=0. Positive x values are when the probe was inside the flow, while for negative values the probe is in the bath, outside the flow. The distances from the inflow pipette are represented by the trace color, corresponding to the dashed lines in Figure 5.3A. The data are in agreement with the error function solution to the diffusion equation:

$$Conductance(x) = C_0 + C_1 * \mathrm{erf}\left(\frac{x}{\sigma}\right),$$

as can be seen by the fit to the 62 μm (red) trace (teal trace, Figure 5.3B).

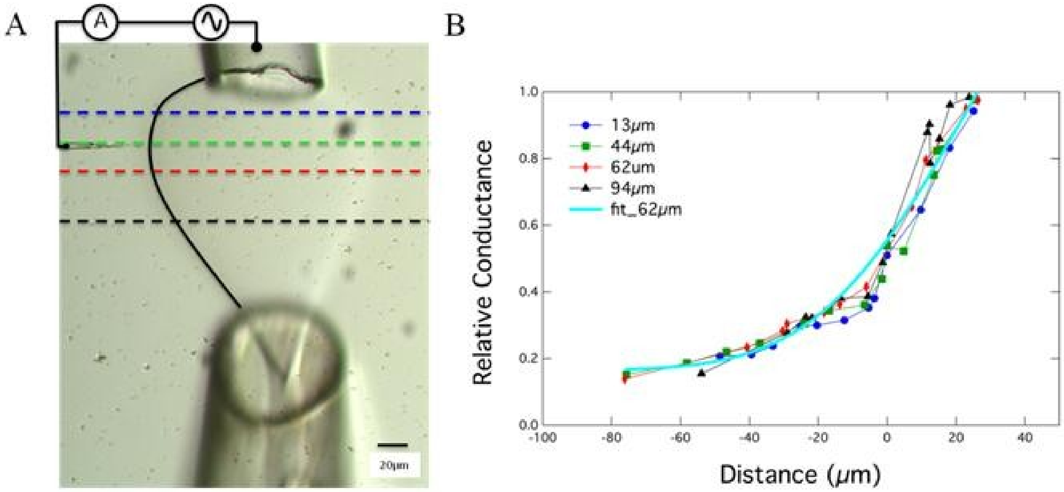

Figure 5.3: Spritzing flow characterization. (A) Phase contrast image showing flow of NaCl from the inflow pipette (bottom) to the outflow piipette (top). Probes for measuring relative conductance are denoted by the circuit schematic. Bath probe distances are denoted by dashed lines, solid black line represents flow edge. (B) Plot of relative conductance vs. probe distance from inflow pipette with associated error function it. Flow edge is $x = 0$.

5.3.1 Single Cell Treatment: Blebbistatin

The contraction inhibitor blebbistatin (described previously) was used to demonstrate biochemical treatment of single cells using the described experimental setup.

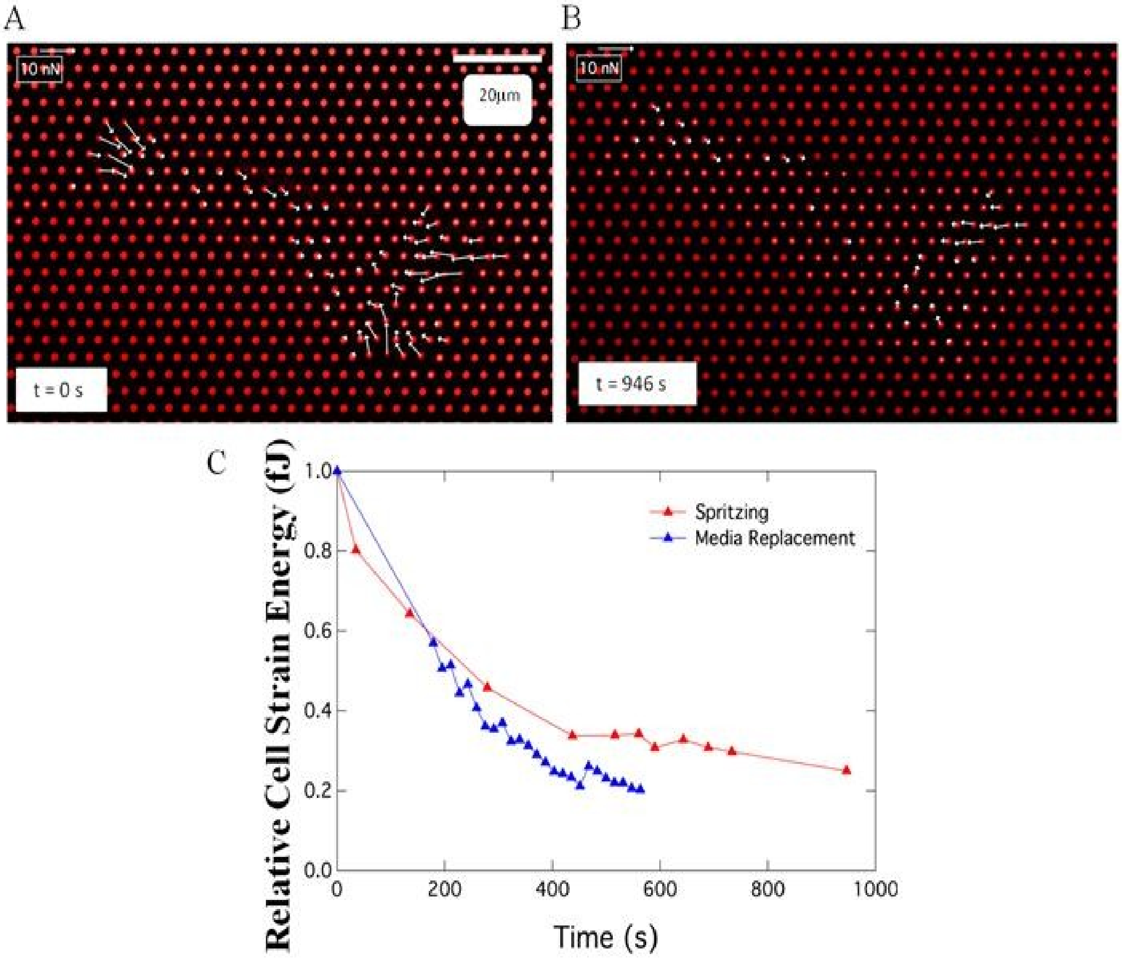

Figure 5.4: Force vector plot at t = 0s (A) and t = 980s (B). Relative change in whole cell strain energy vs. time for a single BPASMC treated with blebbistatin via media replacement (blue) and spritzing (red).

Figure 5.2 shows the controlled treatment region created by the micropipette system. Inside the flow region is a single BPASMC adhered to the underlying mPAD. Figure 5.4 A and B are force vector maps for the cell treated via spritzing before and after 980s of exposure to treatment, respectively. Figure 5.4 C shows a plot of the relative change in whole cell strain energy vs. time for two cells. The blue trace represents a cell that was exposed to blebbistatin treatment via supplementation to the entire media bath containing the mPAD (image not shown). The red trace represents the cell pictured in Figure 5.2, which was treated using the spritzing system without exposing the rest of the mPAD culture to blebbistatin treatment. This data shows that the spritzing system is capable of drug delivery at rates comparable to standard media replacement methods, and can be used to treat single cells under observation without treating unobserved cells that could potential be used for further data collection.

5.3.2 Trypsin Manipulation of Cell pairs

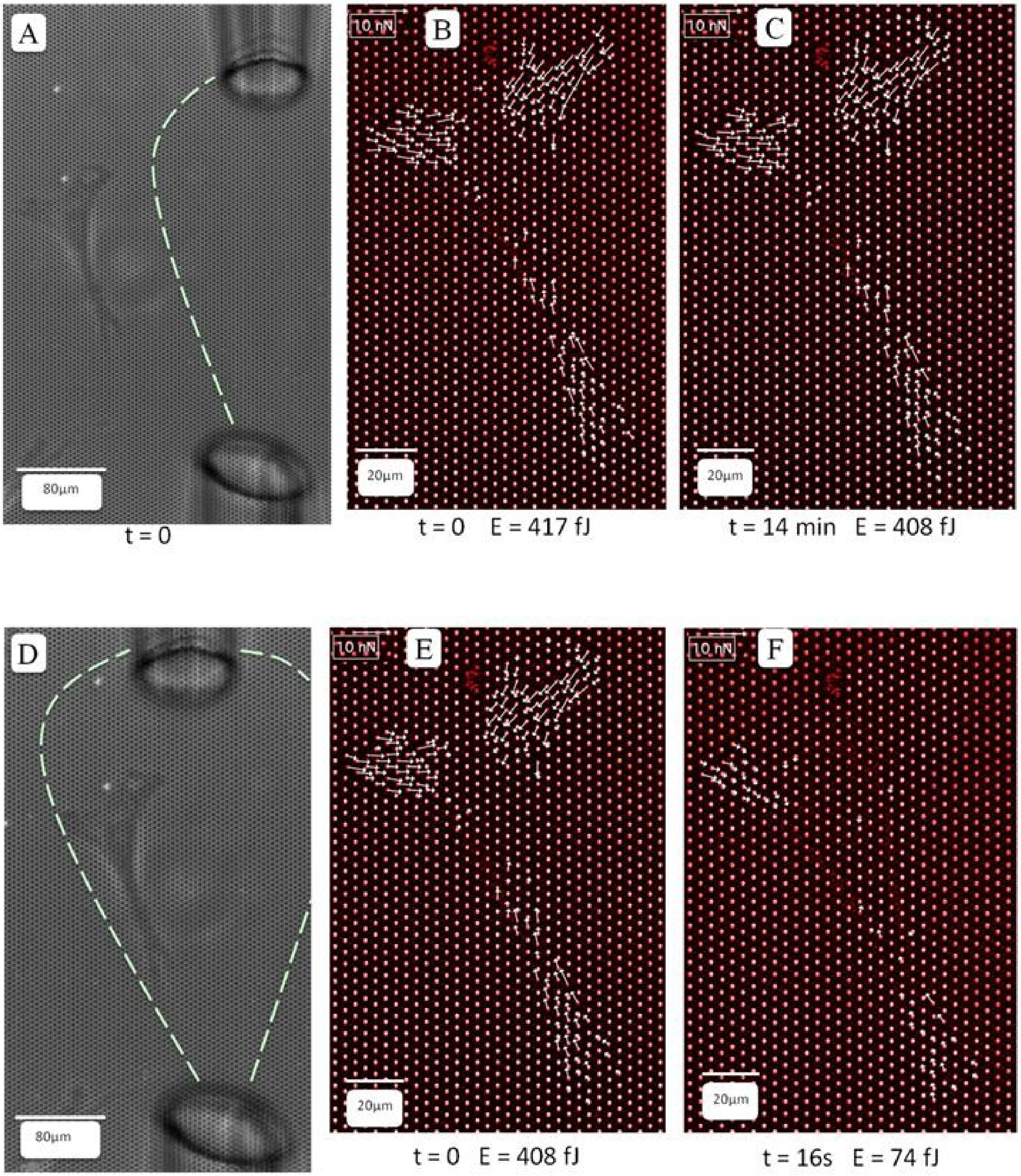

t = 0

t = 0 E = 417 fJ

t = 14 min E = 408 fJ

t = 0 E = 408 fJ

t = 16s E = 74 fJ

Figure 5.5: Testing the precision of trypsin flow using sprtizing system. (A) Phase contrast image showing flow edge and proximity to a nearby BPASMC. Vector maps and whole cell strain energy values at t = 0 (B), and after 14 minutes of trypsin flow (C). (D) Phase contrast image showing as cell was moved into the flow. Vector maps show cell detachment within 16s of exposure (E),(F).

Trypsin-EDTA is commonly used in cell culture in order to remove adherent cells from their substrate. Trypsin is a protease commonly found in the digestive systems of many vertebrates that breaks the integrin binding responsible for cell adhesion. Because Ca2+/Mg2+ ions present in culture medium inhibit the action of Trypsin, a combination of Trypsin and the chelating agent Ethylenediaminetetraacetic acid (EDTA) is used to disrupt cell-substrate adhesions. With the goal of using localized Trypsin treatment to selectively manipulate cell-substrate adhesions on mPADs, we performed a control experiment to test the locality of Trypsin flow using the spritzing system. Figure 5.6 shows that bringing the visible flow of trypsin within 40 μm of an adherent BPASMC (A) has no affect on the cell's attachment to the mPAD substrate following 14 minutes of active flow (B), (C). However, once the cell is moved into the visible flow (Figure 5.6 D), detachment from the mPAD rapidly occurs, visible here as a loss of traction forces imparted by the cell to the substrate after only 16 s of treatment (D), (E).

In combination with techniques previously described to culture pairs of BPASMCs on mPADs, the spritzing system was used to alter the cell-substrate adhesion of one cell in a cell pair cultured on an mPAD substrate. Following disruption, the traction force response of the untreated cell was measured. Determination of cell-cell force (Section 2.3.3) showed that cell-cell force decreased in response to disruption of cell-substrate adhesions of one cell in the pair. This decrease in cell-cell force was coincident with an increase in total cell strain energy by the untreated cell.

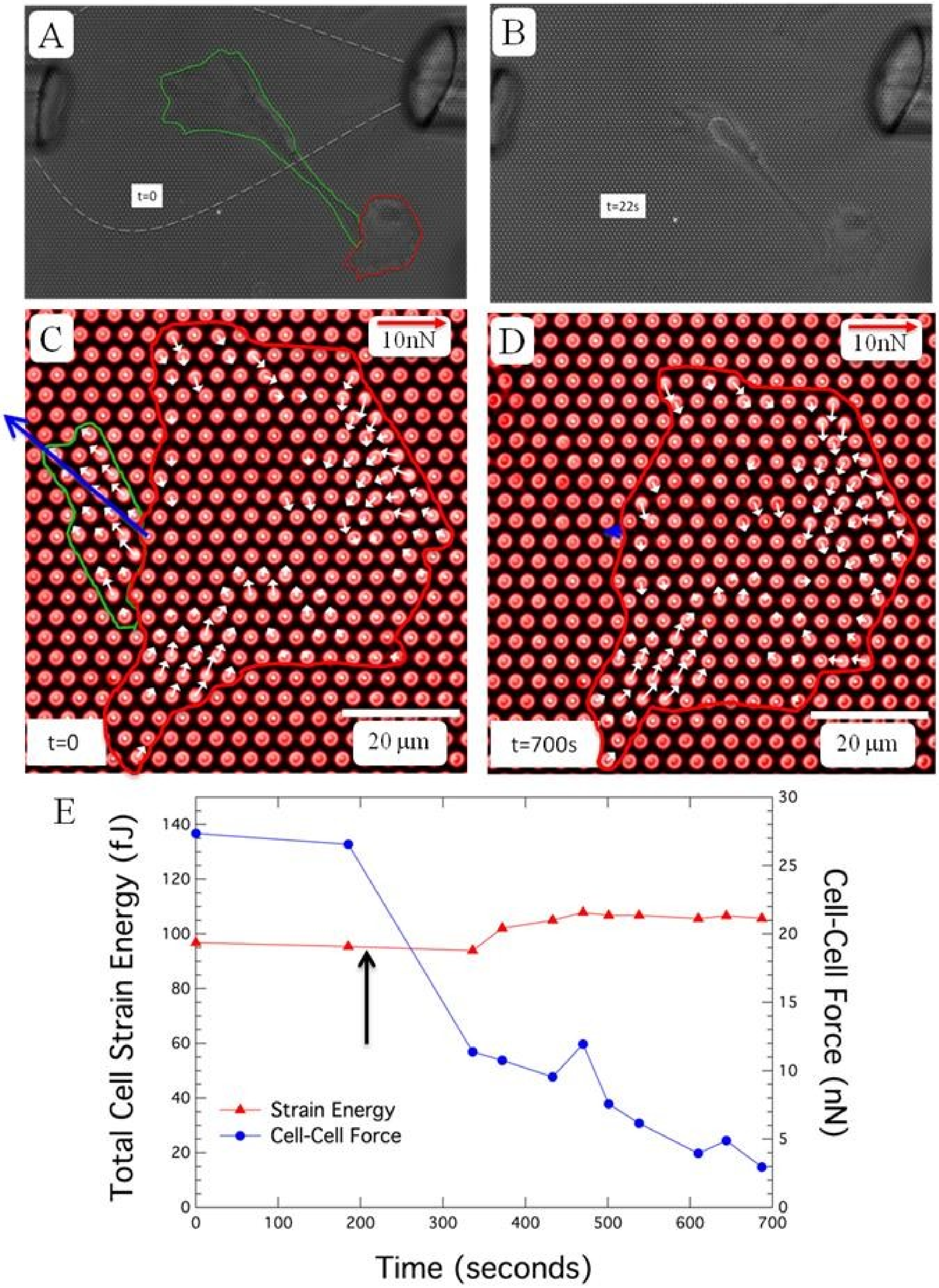

Figure 5.6: (A) phase contrast image showing two cells in a pair configuration and the Trypsin-EDTA treatment flow plume. Phase contrast image showing trypsinisation of one cell in the pair after 22s of treatment flow. Force vector maps, including the cell-cell force, for the untreated cell (red outline) and the treated cell (green outline) prior to treatment (C), and following treatment (D). (E) Total cell strain energy of the untreated

cell (red), and cell-cell force (blue) in response to trypsin treatment. Treatment onset indicated by vertical arrow.

5.3.3 Microtissues

The use of micropipette spritzing was also demonstrated in conjunction with microfabricated devices designed to study the mechanics of micron-scale tissue constructs, termed μTUGs [48]. These devices facilitate the formation of arrays of micron-scale tissues that of consist of hundreds of cells and extra cellular matrix (ECM). To demonstrate the spritzing technique for chemical treatment of a single tissue construct within the larger μTUG device, Hoechst dye was used to stain the nuclei of cells within a single microtissue (Figure 5.7 A, B) without exposure of neighboring tissues (Figure 5.7 C).

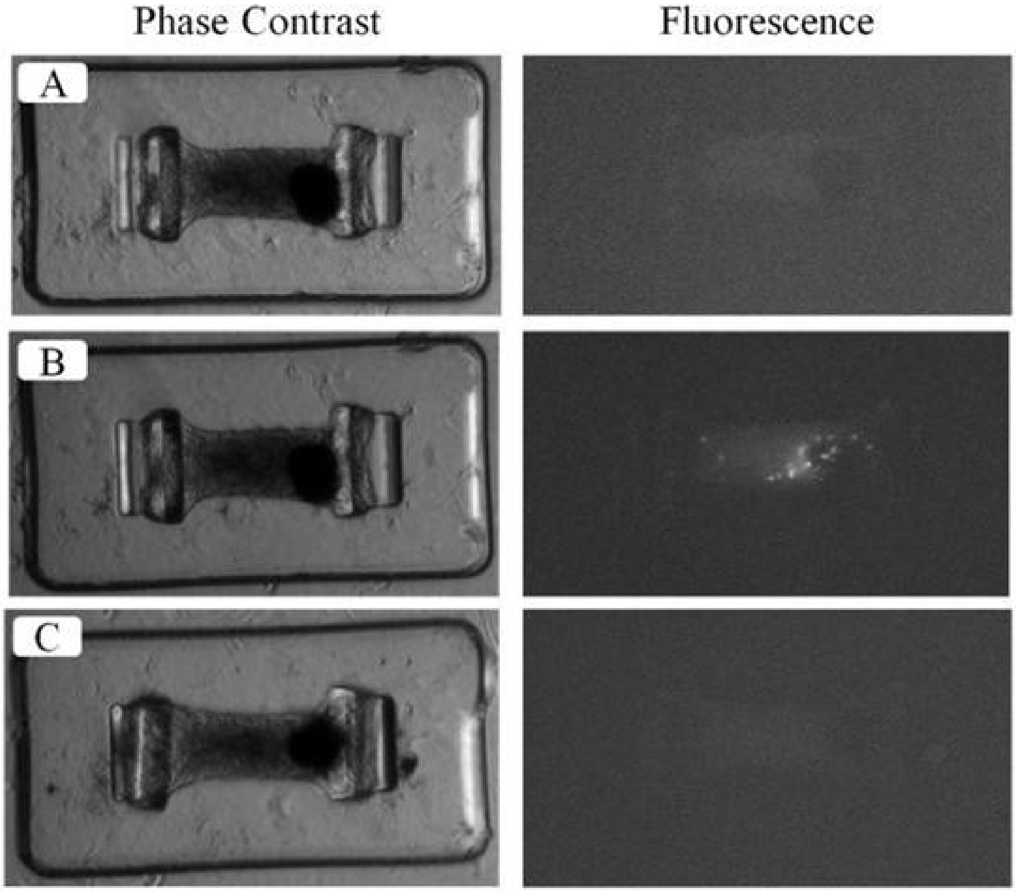

Figure 5.7: Hoechst dye labeling of cell nuclei in a single microtissue within a TUG device. A microtissue before (A) and after (B) 15 minutes of exposure to treatment. (C) Neighboring tissue is unexposed following treatment.

Further experiments demonstrating the use of the spritzing setup in conjunction with μTUG devices were performed using trypsin-EDTA to selectively disrupt cell-matrix adhesions within single tissues. In two examples shown (Figures 5.9, 5.10), cells within the microtissue become detached from the ECM and cluster in un-spread morphologies compared to the smooth appearance of intact tissue observed prior to treatment (t = 0).

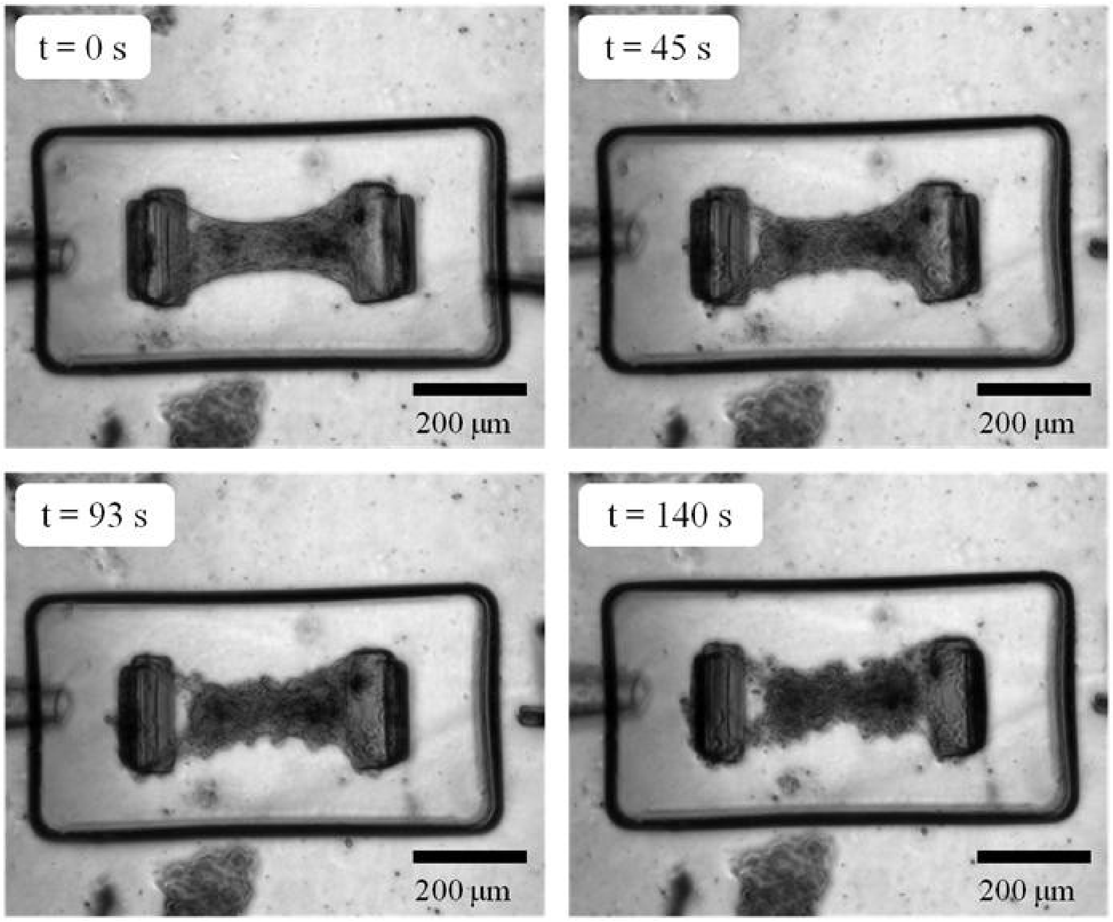

Figure 5.8: Phase contrast images over time of a single microtissue exposed to trypsin treatment via spritzing for disruption of cell-matrix adhesion.

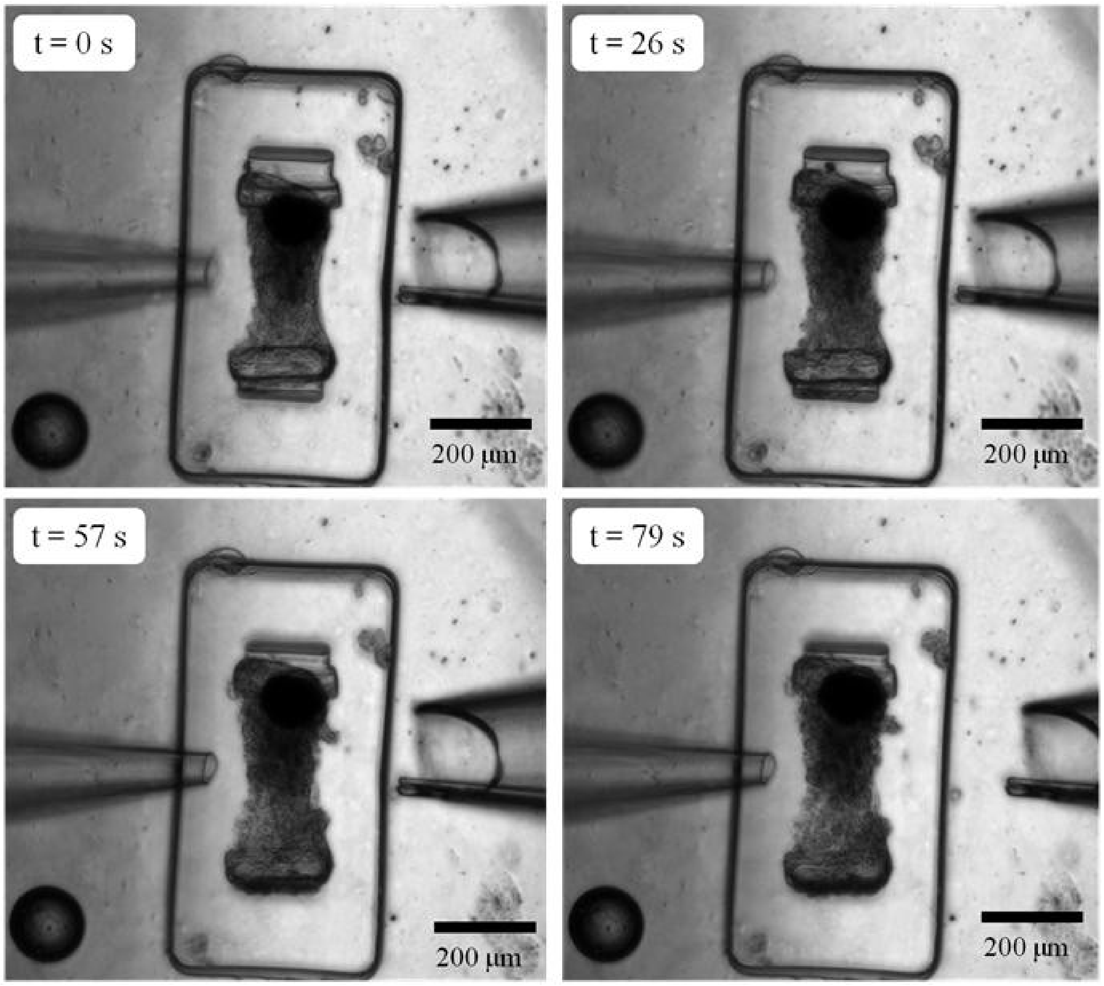

Figure 5.9: Phase contrast images over time of a single microtissue exposed to trypsin treatment via spritzing for disruption of cell-matrix adhesion.

5.4 Discussion

Experiments combining microfabricated devices with a micropipette “spritzing” technique used for application of local chemical stimulation were performed. These experiments demonstrated the functionality of the setup through exposure of single BASMCs cultured on mPADs to treatment with the contraction inhibitors blebbistatin and Y-27632, resulting in decreases in whole cell strain energy imparted to the microposts by the cells. Direct comparison between the time course of blebbistatin treatment using the spritzing set up and that of using bath media replacement showed that local treatment provided a rate of exposure that was comparable with media replacement. This was expected since the concentration of blebbistatin used during the media replacement experiments was the same as that used in the inflow solution in the spritzing experiments. As well, local delivery of Hoechst dye, which labels DNA in the cell nucleus, was demonstrated on µTUG devices through selective treatment of a single microtissue within the device without exposing neighboring tissues to treatment. This same technique was used to selectively treat single microtissues with trypsin-EDTA, which could enable paired measurements of tissue mechanics for intact and “de-cellularized” tissues [49]. The ability to expose single cells or constructs within a microfabricated device that contains a bulk media bath for cell culture will allow for increased experimental efficiency when observations of dynamic effects in real time are desired. By allowing for simultaneous treatment and observation, single cells and constructs that would otherwise be “lost” due to unobserved treatment via media bath replacement will now be available for observation.

Cell-cell contacts are critical to tissue formation, maintenance, and repair [50], and are also sites of active force generation and transmission [51]. It is therefore critical to further our understanding of how cells sense and respond to forces imposed through cell-cell interaction. Local chemical stimulation of one cell within a cell pair configuration, where two cells are in visible contact with each other, provided a means to investigate the traction force response of the untreated cell to changes imposed through cell-cell interactions. Experiments were performed using local treatment with Trypsin-EDTA to partially disrupt cell-substrate adhesions for one cell in a cell pair, and the resulting change in cell-cell force and contractility of the untreated cell was measured. These results showed that forced cell-substrate detachment for one cell in a pair subsequently caused a drop in force generation at cell-cell adhesions. The observed drop in cell-cell force in turn caused changes in traction force orientation and magnitude in the neighboring, untreated cell; demonstrating how force transduction at cell-cell contacts can affect cell-substrate force generation.

The combination of force sensing culture substrates and the ability to apply controlled local stimulation at the cellular level provides a useful tool for the study of cell-cell interactions.

Chapter 6 Conclusion

Our growing knowledge of the importance of physical phenomena in the regulation and proper functioning of biological systems is driving the development of specialized tools and methodologies that enable precise measurements of cellular activity and mechanical properties. The ability to selectively manipulate the in vitro environment and to apply specific stimuli to biological cells are powerful tools for the elucidation of how physical interactions can lead to pathological conditions.

By combining a microfabricated device that enabled measurement of cell generated forces with controlled interaction of cardiac fibroblasts and myocytes through the fabrication of model cardiac tissues, specific experiments designed to define the role of mechanical interactions in impaired cardiac tissue function were able to be performed. Slowing of electrical signal conduction velocity (CV) due to heterocellular coupling between cardiac fibroblasts (CFs) and cardiac myocytes was found to be the result of mechanical coupling between these two cells types. Chemical and genetic interventions that were shown to directly alter CF force generation also served to influence CV in ways consistent with the hypothesis that the contractile forces generated by CFs were causing the observed CV slowing. Further chemical and genetic intervention was applied to the model tissue system in order to disrupt the proposed coupling mechanism, which, along with confirmation that CF contractility was unaffected by these treatments, was found to be N-Cadherin mediated transfer of mechanical force generated by CFs to the myocyte membranes, opening stretch activated channels. The opening of these channels likely causes unregulated depolarization of myocyte membrane potential, which can lead to dangerous arrhythmias in vivo. These experiments demonstrate how mechanical forces can regulate cellular function, and how understanding of the exact mechanisms can be gained through the combined use of a controlled microenvironment and microfabricated tools.

An enhanced version of the mPAD device used for measuring cell generated contractile forces was developed in order to apply global stretch stimulation to arterial smooth muscle cells. Flexible membranes containing micropost arrays were fabricated from PDMS and stretched in a custom culture chamber, enabling real time observation of traction force dynamics *during* stretch. These experiments revealed that while the response of single cells to applied stretch was in general viscoelastic, cell response during increasing strain could vary greatly. Previous experiments using similar systems [39, 40] that observed cellular response prior to and following transient stretch had attributed the large drop in traction forces following stretch to be caused by the dramatic release in tension associated with the un-stretch portion of the protocol. Our data taken during stretch revealed that relaxation of forces could occur well before stretch release. While a subset of the cells tested exhibited increased force generation in response to stretch, others showed maintained or even decreasing forces while substrate strain was still increasing. The mechanisms behind these differing responses could play a critical role in the progression of mechanically mediated arterial diseases such as fibrosis and vascular hypertension. To this end, experiments using our system could be performed to determine if the response to stretch is altered in diseased smooth muscle cells, which would then allow for genetic and/or chemical intervention to determine the mechanism responsible for any observed differences.

Finally, the combined use of local chemical stimulation with the mPAD devices was shown to enable single cell manipulation and determination of cell-cell forces in cell pairs. Similar experiments could be used to investigate wound healing mechanisms through controlled formation, via trypsin treatment, of model wounds in cell monolayers on mPADs, where dynamics in force generation during model wound healing could be observed.

The results described in this work demonstrate the value of microfabricated devices for investigating physical cell-cell and cell-substrate interactions, and how insights gained from furthering our understanding of these interactions provide critical information necessary for moving towards treatments for pathologies that involve mechanical interactions in biological systems.

Bibliography

1. W. Becker, L.K., and J. Hardin, *The World of the Cell*. 2003, Redwood City, CA: Benjamin/Cummings.
2. Kimura, K., et al., *Regulation of myosin phosphatase by Rho and Rho-associated kinase (Rho-kinase).* Science, 1996. **273**(5272): p. 245-8.
3. Bers, D.M., *Calcium fluxes involved in control of cardiac myocyte contraction.* Circ Res, 2000. **87**(4): p. 275-81.
4. Qiagen. *Extracellular Matrix & Adhesion Molecules*. 2013; Available from: http://www.qiagen.com/products/genes%20and%20pathways/complete%20biology%20list/extracellular%20matrix%20and%20adhesion%20molecules.
5. Ruoslahti, E., *RGD and other recognition sequences for integrins.* Annu Rev Cell Dev Biol, 1996. **12**: p. 697-715.
6. Burridge, K., et al., *Focal adhesions: transmembrane junctions between the extracellular matrix and the cytoskeleton.* Annu Rev Cell Biol, 1988. **4**: p. 487-525.
7. Humphries, J.D., et al., *Vinculin controls focal adhesion formation by direct interactions with talin and actin.* J Cell Biol, 2007. **179**(5): p. 1043-57.
8. Balaban, N.Q., et al., *Force and focal adhesion assembly: a close relationship studied using elastic micropatterned substrates.* Nat Cell Biol, 2001. **3**(5): p. 466-72.
9. Liu, Z., et al., *Mechanical tugging force regulates the size of cell-cell junctions.* Proc Natl Acad Sci U S A, 2010. **107**(22): p. 9944-9.
10. Chen, C.S., et al., *Geometric control of cell life and death.* Science, 1997. **276**(5317): p. 1425-8.
11. Lo, C.M., et al., *Cell movement is guided by the rigidity of the substrate.* Biophys J, 2000. **79**(1): p. 144-52.
12. Parker, K.K., et al., *Directional control of lamellipodia extension by constraining cell shape and orienting cell tractional forces.* Faseb j, 2002. **16**(10): p. 1195-204.
13. Ingber, D.E., *Mechanobiology and diseases of mechanotransduction.* Ann Med, 2003. **35**(8): p. 564-77.
14. Cunningham, K.S. and A.I. Gotlieb, *The role of shear stress in the pathogenesis of atherosclerosis.* Lab Invest, 2005. **85**(1): p. 9-23.
15. Weiss, L., G. Elkin, and E. Barbera-Guillem, *The differential resistance of B16 wild-type and F10 cells to mechanical trauma in vitro.* Invasion Metastasis, 1993. **13**(2): p. 92-101.
16. Camelliti, P., T.K. Borg, and P. Kohl, *Structural and functional characterisation of cardiac fibroblasts.* Cardiovasc Res, 2005. **65**(1): p. 40-51.
17. Souders, C.A., S.L. Bowers, and T.A. Baudino, *Cardiac fibroblast: the renaissance cell.* Circ Res, 2009. **105**(12): p. 1164-76.
18. Brown, R.D., et al., *The cardiac fibroblast: therapeutic target in myocardial remodeling and failure.* Annu Rev Pharmacol Toxicol, 2005. **45**: p. 657-87.
19. Hinz, B., et al., *The myofibroblast: one function, multiple origins.* Am J Pathol, 2007. **170**(6): p. 1807-16.
20. Tomasek, J.J., et al., *Myofibroblasts and mechano-regulation of connective tissue remodelling.* Nat Rev Mol Cell Biol, 2002. **3**(5): p. 349-63.

21. Tan, J.L., et al., *Cells lying on a bed of microneedles: an approach to isolate mechanical force.* Proc Natl Acad Sci U S A, 2003. **100**(4): p. 1484-9.
22. *Atherosclerosis: comparison of arteries.* 2014; Available from: <http://www.britannica.com/EBchecked/media/100168/Cross-sectional-diagrams-of-human-blood-vessels-showing-a-normal>.
23. Gidaspow, D., *MultiPhase Flow and Fluidization: Continuum and Kinetic Theory Descriptions*. 1994: Academic Press.
24. Gopalakrishnan, S., et al., *Rho GTPase signaling regulates tight junction assembly and protects tight junctions during ATP depletion.* Am J Physiol, 1998. **275**(3 Pt 1): p. C798-809.
25. Sniadecki, N.J., et al., *Magnetic microposts for mechanical stimulation of biological cells: fabrication, characterization, and analysis.* Rev Sci Instrum, 2008. **79**(4): p. 044302.
26. Katagiri, Y., S.A. Brew, and K.C. Ingham, *All six modules of the gelatin-binding domain of fibronectin are required for full affinity.* J Biol Chem, 2003. **278**(14): p. 11897-902.
27. Thompson, S.A., et al., *Mechanical coupling between myofibroblasts and cardiomyocytes slows electric conduction in fibrotic cell monolayers.* Circulation, 2011. **123**(19): p. 2083-93.
28. Thompson, S.A., et al., *Acute slowing of cardiac conduction in response to myofibroblast coupling to cardiomyocytes through N-cadherin.* J Mol Cell Cardiol, 2014. **68c**: p. 29-37.
29. Kovacs, M., et al., *Mechanism of blebbistatin inhibition of myosin II.* J Biol Chem, 2004. **279**(34): p. 35557-63.
30. Yang, X.C. and F. Sachs, *Block of stretch-activated ion channels in Xenopus oocytes by gadolinium and calcium ions.* Science, 1989. **243**(4894 Pt 1): p. 1068-71.
31. Verheule, S., et al., *Characterization of gap junction channels in adult rabbit atrial and ventricular myocardium.* Circ Res, 1997. **80**(5): p. 673-81.
32. Kohl, P., et al., *Electrical coupling of fibroblasts and myocytes: relevance for cardiac propagation.* J Electrocardiol, 2005. **38**(4 Suppl): p. 45-50.
33. Pedrotty, D.M., et al., *Structural coupling of cardiomyocytes and noncardiomyocytes: quantitative comparisons using a novel micropatterned cell pair assay.* Am J Physiol Heart Circ Physiol, 2008. **295**(1): p. H390-400.
34. Wipff, P.J. and B. Hinz, *Myofibroblasts work best under stress.* J Bodyw Mov Ther, 2009. **13**(2): p. 121-7.
35. Follonier, L., et al., *Myofibroblast communication is controlled by intercellular mechanical coupling.* J Cell Sci, 2008. **121**(Pt 20): p. 3305-16.
36. Liu, Z., et al., *Blebbistatin inhibits contraction and accelerates migration in mouse hepatic stellate cells.* Br J Pharmacol, 2010. **159**(2): p. 304-15.
37. Lijnen, P., V. Petrov, and R. Fagard, *Transforming growth factor-beta 1-mediated collagen gel contraction by cardiac fibroblasts.* J Renin Angiotensin Aldosterone Syst, 2003. **4**(2): p. 113-8.
38. Dubin-Thaler, B.J., et al., *Quantification of cell edge velocities and traction forces reveals distinct motility modules during cell spreading.* PLoS One, 2008. **3**(11): p. e3735.
39. Krishnan, R., et al., *Reinforcement versus fluidization in cytoskeletal mechanoresponsiveness.* PLoS One, 2009. **4**(5): p. e5486.
40. Chen, C., et al., *Fluidization and resolidification of the human bladder smooth muscle cell in response to transient stretch.* PLoS One, 2010. **5**(8): p. e12035.
41. Hirata, H., H. Tatsumi, and M. Sokabe, *Mechanical forces facilitate actin polymerization at focal adhesions in a zyxin-dependent manner.* J Cell Sci, 2008. **121**(Pt 17): p. 2795-804.

42. Tang, Q.Y., et al., *Characterization of a functionally expressed stretch-activated BKca channel cloned from chick ventricular myocytes.* J Membr Biol, 2003. **196**(3): p. 185-200.
43. Munevar, S., Y.L. Wang, and M. Dembo, *Regulation of mechanical interactions between fibroblasts and the substratum by stretch-activated Ca2+ entry.* J Cell Sci, 2004. **117**(Pt 1): p. 85-92.
44. Kaunas, R., et al., *Cooperative effects of Rho and mechanical stretch on stress fiber organization.* Proc Natl Acad Sci U S A, 2005. **102**(44): p. 15895-900.
45. Streit, J. and H.D. Lux, *Distribution of calcium currents in sprouting PC12 cells.* J Neurosci, 1989. **9**(12): p. 4190-9.
46. Ainla, A., et al., *A multifunctional pipette.* Lab Chip, 2012. **12**(7): p. 1255-61.
47. Frank, T. and S. Tay, *Flow-switching allows independently programmable, extremely stable, high-throughput diffusion-based gradients.* Lab Chip, 2013. **13**(7): p. 1273-81.
48. Legant, W.R., et al., *Microfabricated tissue gauges to measure and manipulate forces from 3D microtissues.* Proc Natl Acad Sci U S A, 2009. **106**(25): p. 10097-102.
49. Zhao, R., et al., *Decoupling cell and matrix mechanics in engineered microtissues using magnetically actuated microcantilevers.* Adv Mater, 2013. **25**(12): p. 1699-705.
50. Gumbiner, B.M., *Regulation of cadherin-mediated adhesion in morphogenesis.* Nat Rev Mol Cell Biol, 2005. **6**(8): p. 622-34.
51. Chen, C.S., J. Tan, and J. Tien, *Mechanotransduction at cell-matrix and cell-cell contacts.* Annu Rev Biomed Eng, 2004. **6**: p. 275-302.

List of Publications

1. **C. R. Copeland**, A. S. Liu, R. Zhao, C. S. Chen, and D. H. Reich, "Comparative Study of Force Generation and Response to Stretch by Isolated Smooth Muscle Cells and Smooth Muscle Cell Microtissues ", in preparation.

2. S. A. Thompson, A. Blazeski, **C. R. Copeland**, D.M. Cohen, C.S. Chen, D. H. Reich, and L. Tung, "Acute slowing of cardiac conduction in response to myofibroblast coupling to cardiomyocytes through N-Cadherin," J Mol Cell Cardiol, 2014. **68c**: p. 29-37.

3. E. J. Felton, **C. R. Copeland**, C. S. Chen, and D. H. Reich, "Heterotypic cell pair co-culturing on patterned microarrays," Lab Chip **12**, 3117-3126 (2012).

4. S. A. Thompson, **C. R. Copeland**, D. H. Reich, and L. Tung, "Mechanical coupling between myofibroblasts and cardiomyocytes slows electric conduction in fibrotic cell monolayers," Circulation **123**, 2083-2093 (2011)

Vita

Craig Robert Copeland was born on August 21, 1985 in Baltimore, Maryland to Wayne and Phyllis Copeland. He attended the University of Maryland Baltimore County, where he graduated magna cum laude with a B.S. in Physics in May 2007. He received his Ph.D. from Johns Hopkins University in February, 2014